Microfabrication of Plasmonic Devices: PPBG Biosensor in Cytop, Intensity Modulator, and Atomically Flat Nanohole Array

by

Sa'ad Hassan

A Thesis submitted to the Faculty of Graduate Studies and Postdoctoral Studies in partial fulfillment of the requirements for the degree of
Master of Applied Science, Chemical Engineering

April 2015

Department of Chemical and Biological Engineering
University of Ottawa
Ottawa, Ontario, Canada

Acknowledgements

Foremost, I would like to thank my parents; my mother, Maryan Abdirahman, for her unwavering support and wisdom and my father, Mohamed Hassan, for his constant encouragement and for instilling in me a life-long love of learning. Without their support and love I would have never made it this far.

I would also like to express my deep gratitude to my supervisors, Niall Tait and Pierre Berini for guiding me through my research and sharing their extensive knowledge and expertise. Further, I would also like thank the technical staff at Carleton, and Ottawa U: Rob Vandusen, Rick Adams, Angela McCormick, Ewa Lisicka-Skrzek, and Anthony Olivieri. Without their work, experience and patience much of this thesis would have been impossible.

This thesis is dedicated to my sister, Hodan Hassan, the best person I know.

Abstract

This thesis details the fabrication of three different plasmon-polariton based devices: a plasmon-polariton Bragg grating (PPBG) biosensor, an intensity modulator incorporating grating couplers, and optically separated electrical contact, and finally an array of nanoholes in an ultrasmooth Au film. The biosensor involves a 35 nm Au stripe, lithographically stepped in width to produce a Bragg reflector. The waveguide is embedded in symmetric, Cytop claddings 8 μm thick. Channels are etched into the top cladding, exposing the waveguides and allowing for the integration of fluidics. The modulator involves a 20 nm Au pad, overlaid with 80 nm Au diffraction gratings, supported by an ultrathin (~3 nm) SiO_2 insulator, on a p-doped Silicon wafer backed by an Al Ohmic contact. Electrical contact pads are separated from the waveguide by a thick dielectric (700 nm PMMA), and 2.5 μm vias in-filled with Au allow for electrical connection between the contact pads and waveguides. The nanohole array is machined by focused ion beam into an ultrasmooth Au film revealed by template stripping. The Au film is stacked on a thick film of Cytop between ~5 μm thick.

Résumé

Cette thèse explique la fabrication de trois appareils différents, composés du plasmon polarition: un biosenseur de plasmon polarition Brag grating (PPBG), un modulateur d'intensité qui intègre des grilles de coupleur, et du contact électrique visuellement séparé, et finalement, une série de nanotrous dans un Au film lisse. Le biosenseur s'implique d'un 35 nm Au stripe, étagé en largeur lithographiquement pour produire un réflecteur Bragg. Le guide d'ondes est intégré en placage de Cytop symmétriques, avec un épais de 8 µm. Des sillons sont intègrés dans le placage en haut, en exposant le guide d'ondes et en permettant l'intégration des fluidiques. Le modulateur s'implique d'un 20nm Au pad, recouvert avec des réseau de diffraction de 80nm Au, supporté par un insulateur SiO_2 ultrafin (~3 nm), sur une gaufrette de silicium supporté par un contact d'Al Ohmic. Les rembourrages de contacts électriques sont séparés du guide d'ondes diélectrique (700 nm PMMA), et 2.5 µm vias remplit avec Au qui permet un connection électique entre les rembourrages de contacts et les guides d'ondes. La série de nanotrous est fabriquée des rayons d'ion centralisés dans un Au film lisse révelée par l'enlêve des gabarits. Le film d'Au est mis sur un film de Cytop épais, entre ~5 µm.

Table of Contents

List of Figures

1 Introduction

2 Chapter 2

3 Chapter 3

4 Chapter 4

1. Introduction

1.1 Motivation

This thesis is concerned with the fabrication of three different plasmonic devices: Plasmon polariton bragg grating (PPBG) biosensor in Cytop, a reflection intensity modulator and a nanohole array. The fabrication of each device entails unique challenges and device overviews are provided in section 1.5. Each of these devices relies on inexpensive silicon chip fabrication techniques.

The PPBG biosensor represents a modification of a biosensor fabricated previously that had straight wave-guides and mach-zehnder interferometers embedded in Cytop bottom and top claddings (see section 1.6). Unlike straight waveguides, PPBGs are not loss sensitive but are instead phase sensitive i.e., binding events are transduced into a phase shift in the bragg reflectance wavelength. The Cytop cladding allows for both symmetrisation of the refractive indexes of the substrate and superstrate along with index matching of fluidics to the top cladding. A phase-shift based biosensor with incorporated microfluidics, composed of biocompatible materials is of great interest, and was successfully fabricated.

Opto-electronic devices are miniaturizing and SPPs, with their strong confinement and surface sensitivity, are of interest in assisting in further shrinking of these devices. The intensity modulator, fabricated as part of this thesis, possesses a unique, particularly compact design. This compact design allows for over 2000 modulators in an area of 100 mm^2. The modulator relies on SPPs whose index can be modified by the carrier refraction effect, and which can be excited by perpendicular p-polarised light incident on grating couplers.

The nanohole array, fabricated as part of this thesis, represents a beachhead in the sensitivity of nanohole based surface plasmon resonance sensors. Traditional SPR sensors were dominated by Kretschmann prism based sensors which could achieve vastly superior sensitivity and resolution. The nanohole array achieves a resolution of 9.38×10^{-8} refractive index units (RIU), which is, for the first time, comparable with commercially available kretschmann SPR sensors. This is extremely promising because nanoholes have a number of properties which are advantageous. These properties are high multiplexing, the ability to integrate microfluidics into the sensor, and parallel processing. The high resolution of the nanohole array is achieved by three main factors: FDTD based optimization of nanohole dimenions, Cytop substrate which allows for index symmetrisation with the bulk fluid and an extremely smooth metal film surface achieved by template stripping.

1.2 Surface Plasmons

Plasmons are quantized excitations of the free electrons of a metal, either within the bulk or at the surface [1]. At the interface of two materials with opposite signs to the real part of their permittivities, i.e. a dielectric and a conductor, it is possible to induce a propagating surface plasmon (SP) [2]. This excitation is induced by an incident El1ectroMagnetic (EM) wave at the metal surface. Further, the surface guides the coupled EM wave and SP, henceforth referred to as Surface Plasmon Polariton (SPP), which acts as a transverse-magnetic (TM) polarized optical wave [3].

The surfaces can be arranged as a metal slab, metal clad, or metal stripe. The slab arrangement consists of a thin metal film of thickness *t*, bounded by optically semi-infinite dielectrics, all of which are of infinite width. Conversely, a thin dielectric film cladded by optically semi-infinite metals, which are, again, of infinite width constitutes the metal clad arrangement. Figure 1 depicts the bound SPP modes for the metal clad, metal slab and a single-interface arrangement.

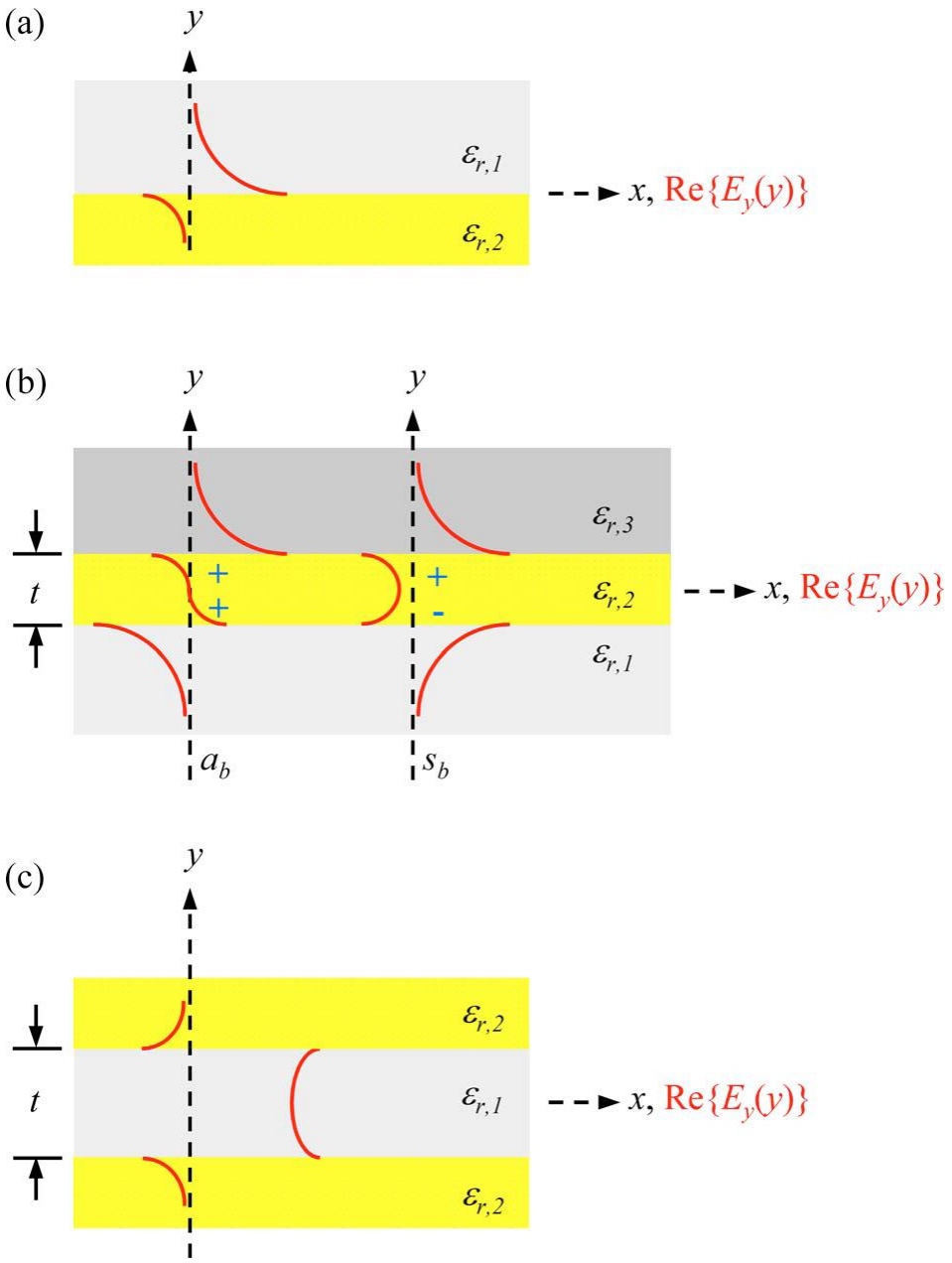

Figure 1. Bound SPP modes propagating in the z direction with the dominant component of the TM represented by red curves. Three different arrangements are displayed: a) Single-interface, b) metal-slab and c) metal-clad. Reprinted figure with permission from Pierre Berini, Physical Review B, 61, 2000 (2000) by the American Physical Society

The single-interface SPP possesses many advantageous qualities. These include sub-wavelength confinement, a high degree of sensitivity, and an energy asymptote in its dispersion curve. Notably, these SPPs are subject to large

attenuation. For a metal that is perfectly smooth and cladded by an ideal dielectric, the majority of the attenuation is due to free electron scattering in the metal with a lesser portion resulting from interband transitions [4]. More realistically, roughness in the metal surface caused by fabrication limitations also contributes to attenuation.

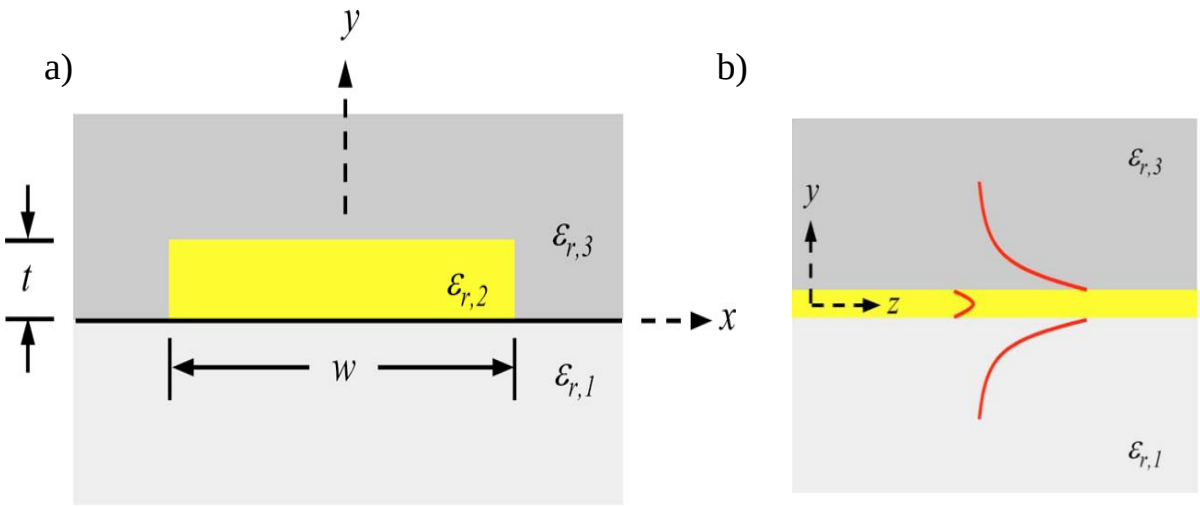

Figure 2. Metal stripe waveguide with bound SPP modes propagating in the z direction. The dominant component of the TM is represented by red curves. a) a cross sectional sketch of the metal stripe in the y-x plane. b) a cross-sectional sketch of the metal stripe in the y-z plane. Reprinted figure with permission from Pierre Berini, Physical Review B, 61, 2000 (2000) by the American Physical Society

The stripe design involves a thin metal stripe of thickness *t,* and finite width *w*, embedded in a dielectric superstrate and substrate [4]. For propagation in the z-direction, the SPP modes are designated by their symmetry or asymmetry in the x-y plane. If only modes of the lowest order are considered, that still allows for 4 possible bound modes: aa_b^0, as_b^0, sa_b^0, and ss_b^0 [5]. Figure 3 plots the computed attenuation of these modes along with the attenuation of several higher-order modes. It is clear, upon looking at Figure 3, that the ss_b^0 mode is characterized by a low attenuation in a thin film, which is why it is also known as the long-range surface

plasmon polariton (LRSPP). This makes the mode of particular interest for many applications.

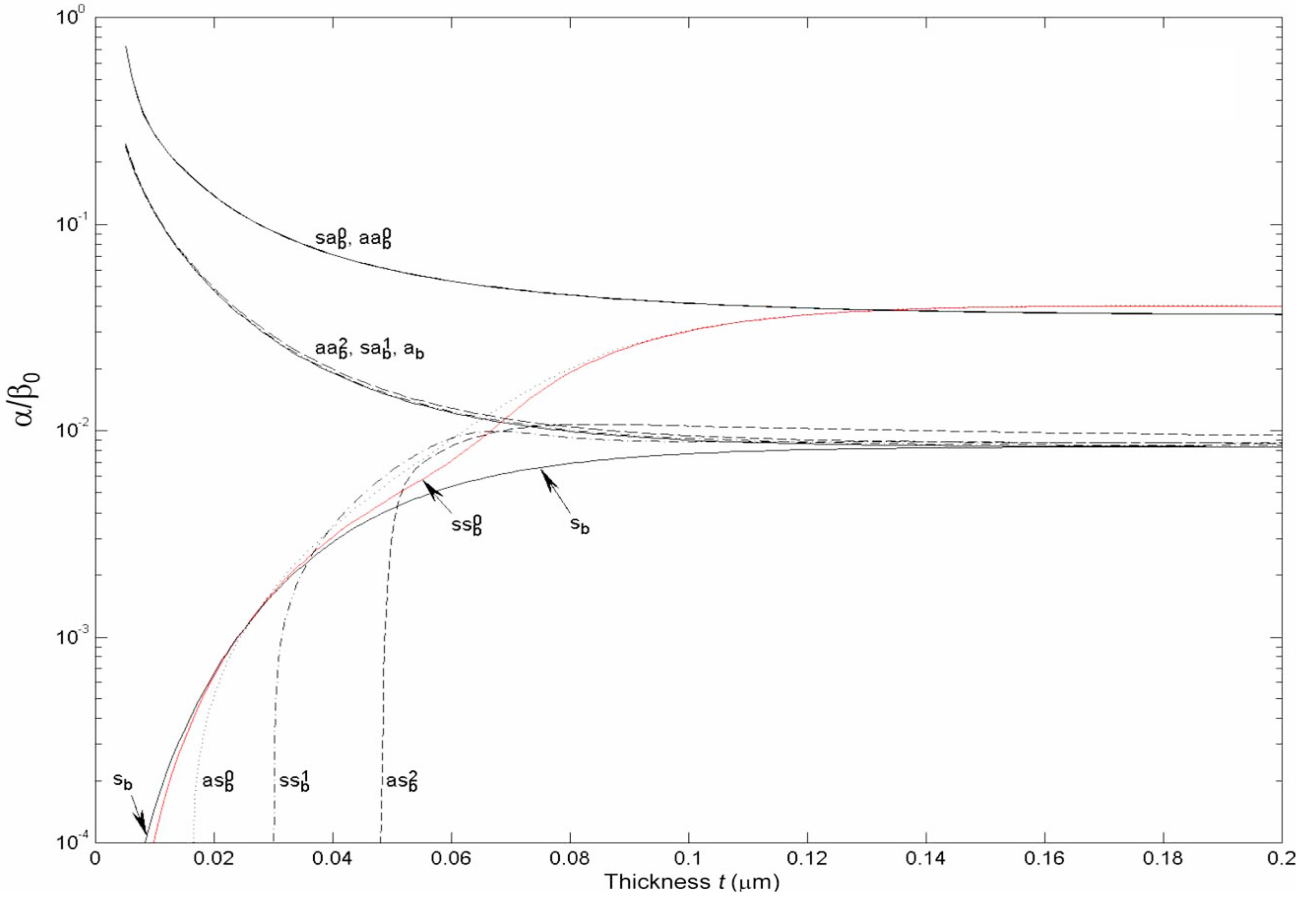

Figure 3. Response of normalized attenuation constant for each SPP mode to waveguide thickness. Reprinted figure with permission from Pierre Berini, Physical Review B, 61, 2000 (2000) by the American Physical Society

1.3 SPP Excitation Strategies

Optical strategies for the excitation of SPPs include prisms, diffraction gratings, nanoholes and end-fibre alignment [1, 6-8]. A common and illustrative example of the prism scheme is the Kretschmann configuration which is displayed in Figure 4. The Kretschmann configuration relies on a dielectric sample of lower refractive index

than the prism. The sample is brought into intimate contact with the prism whose interface surface has been coated with a thin metal film. P-polarized light is shone through the prism at an angle greater than a critical angle producing an evanescent wave at the metal-dielectric interface. Moreover, at a precise angle the propagation constant of the evanescent wave equals that of the SP, producing SPPs and diminishing the intensity of the reflected ray [7].

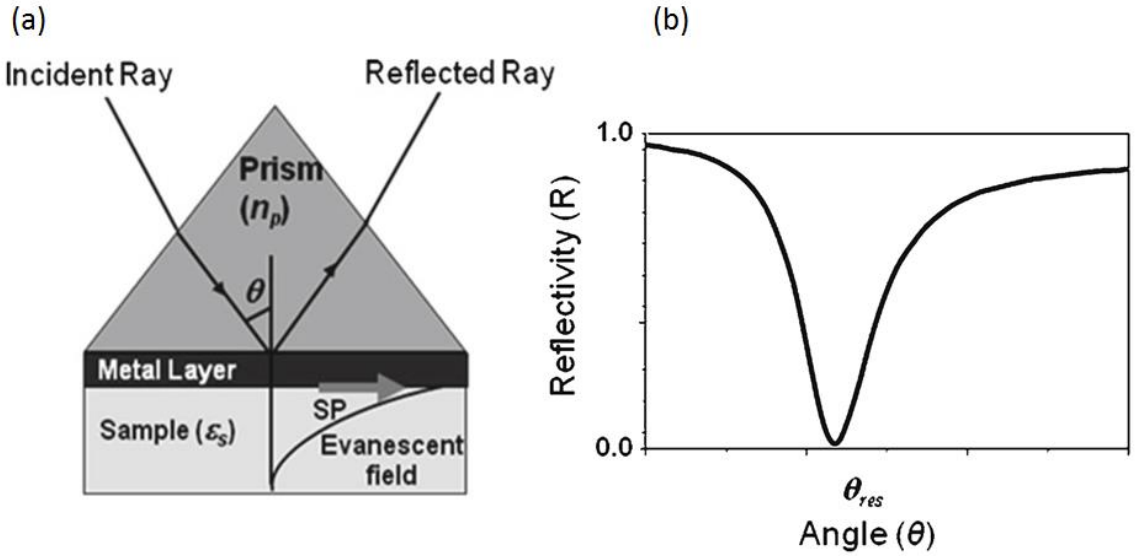

Figure 4. a) Kretschmann configuration b) Normalized reflectivity as a function of angle of incidence. The dip in reflectivity corresponds to θ_{res}, the SP resonant angle. Republished with permission of Springer from Reviews in plasonics, Geddes,C.D, 2010; permission conveyed through the copyright clearance center, Inc.

Diffraction gratings are geometric features in the metal surface which serve to diffract incident light waves into evanescent and propagating waves. A portion of these resultant waves is well-suited to the excitation of SPPs [9]. Efficient excitation of SPPs by grating couplers has been reported in the literature [11]. Grating bump height, duty cycle, and pitch must be optimized to ensure maximum efficiency in SPP excitation [12]. Figure 5 depicts a schematic of diffraction gratings.

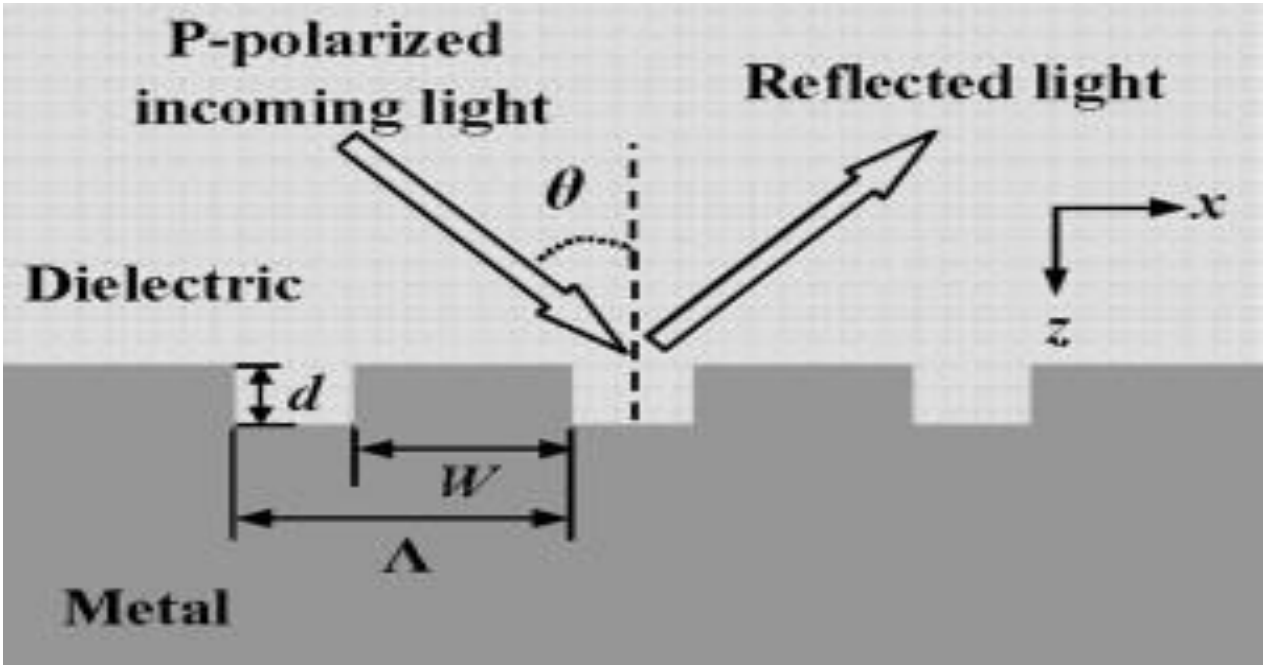

Figure 5. Schematic of metallic grating for SP excitation. *d* is the grating bump height, *w* is the grating width, and *Λ* is the duty cycle.

It has been shown that individual nanoholes through thin metal films can act as “point sources” of SPPs [8]. When the radius of the nanohole is below a critical threshold, the centre of the nanohole acts as the source of the SPP [13]. This excitation of SPPs in nanoholes is also responsible for Extraordinary Optical Transmission (EOT). EOT is a phenomenon which causes orders of magnitude greater transmission of light through a sub-wavelength aperture than would be thought possible by classical aperture theory [14]. A nanohole array and a demonstration of EOT is shown in Figure 6.

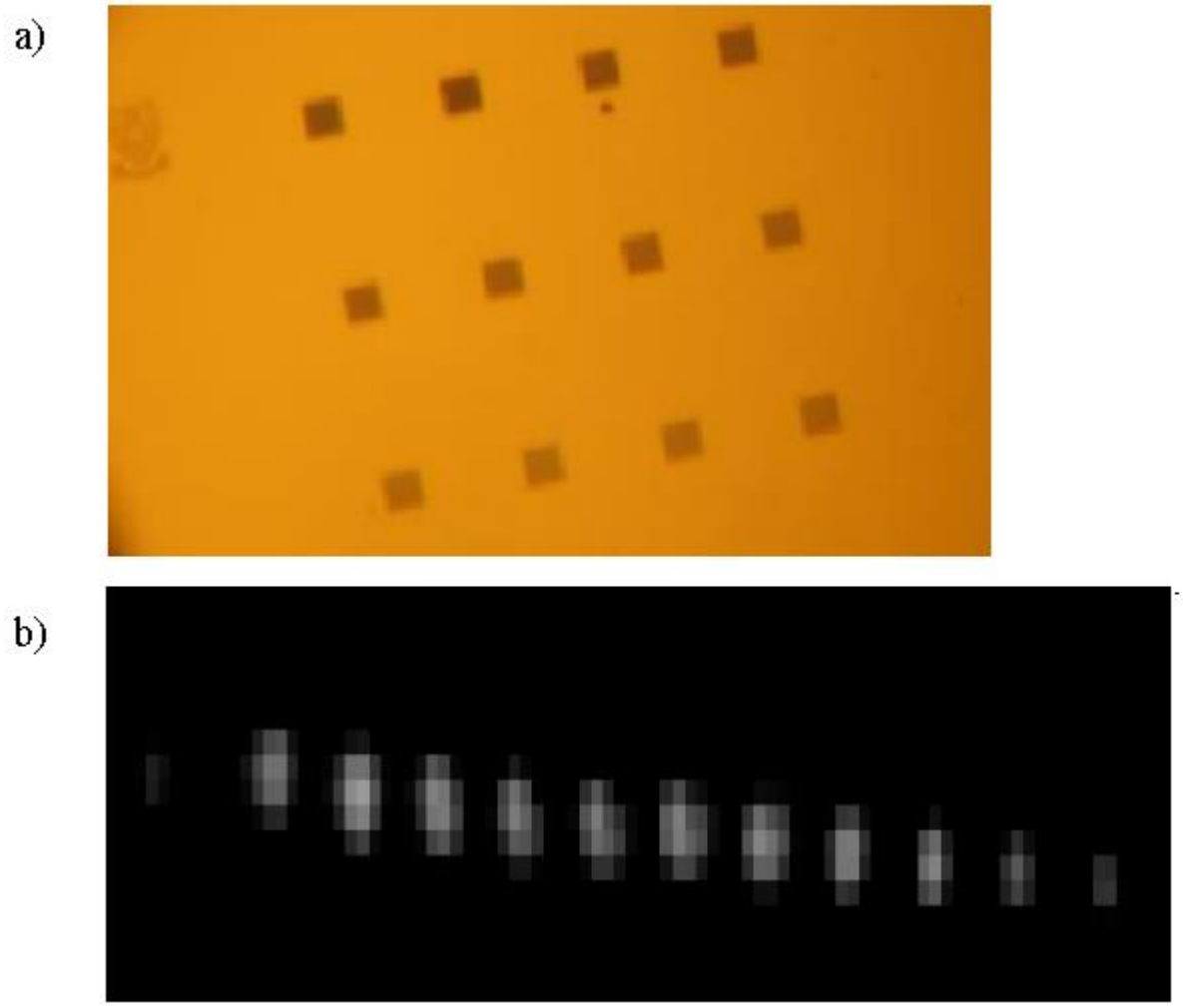

Figure 6. a) Nanohole array. b) light transmitted through the array by EOT captured by a charged coupled device camera. Figure adapted from [15]

End-fibre alignment or butt coupling is a common means of exciting SPP in the metal stripe arrangement. In this scheme, an optical fibre is placed against the end facet of the stripe with a high degree of overlap. When proper alignment is achieved, an EM wave is transmitted with minimal loss of power to the metal stripe, exciting an SPP which propagates along the stripe. Figure 7 shows the butt coupling excitation scheme [16].

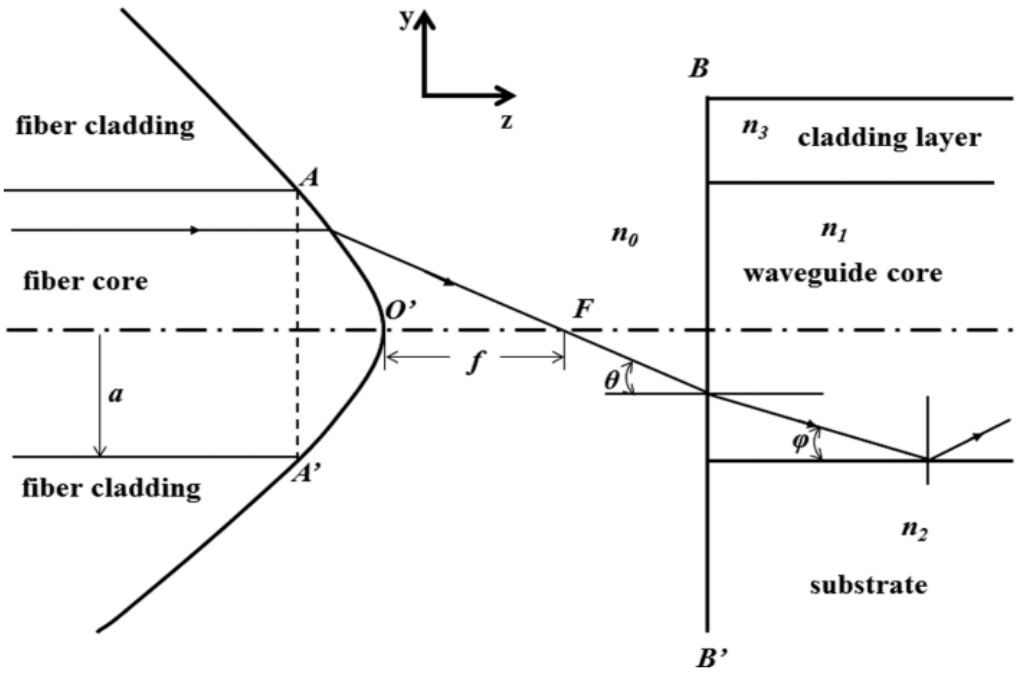

Figure 7. Schematic of butt-coupled system and propagated EM wave. Figure shown as published in [16]

In this thesis, SPP excitation by grating coupling, by nanohole arrays, and by butt-coupling to an optical fibre is of relevance. Device structure and function, along with excitation strategy are explained in section 1.4.

1.4 Microfabrication Methodologies

This thesis is primarily concerned with the successful and improved fabrication of plasmonic devices. The dimensions of these integrated devices necessitate the use of microfabrication and nanofabrication methodologies. An overview of these devices is provided in Section 1.4. A comprehensive review of microfabrication and nanofabrication technologies would be prohibitively long; rather, solely those

techniques exploited in the fabrication of the aforementioned devices are detailed in the following paragraphs.

All techniques used can be divided generically into two types: 1] film deposition and 2] film patterning. The former is concerned with the deposition of thin films composed of polymer, metal, oxide, etc. The latter is concerned with the reproduction of images on surfaces.

Within the scope of this thesis, all polymer layers were deposited by spin-coating. This involves sealing the wafer to a rotatable chuck whose rotation speed and duration can be controlled. The polymer, dissolved in a solvent, is applied to the surface of the wafer which is then spun at a speed prescribed to produce a desired thickness. Afterwards, the wafer is heated to expel the solvent solidifying the polymer on the wafer surface [17, 18]. Spin-coating is an effective and rapid technique for applying uniform polymer films to the surface of a wafer.

Thin-film metal deposition was achieved through physical vapour deposition (PVD), specifically, either electron beam evaporation or thermal evaporation. Both techniques require the sublimation of a metal, whose vapour then expands to fill an evacuated chamber. Upon contacting the sample, the metal vapour condenses, producing a thin film. Resistive thermal evaporation uses heating due to electrical resistance in a carrier, and the resultant conduction of that heat from the carrier to the metal it carries. Electron beam evaporation uses a filament that acts as a cathode releasing high energy electrons. The metal, which acts as the anode, converts the energy of the incident electrons into various forms of energy: thermal energy which heats the metal and high energy EM radiation such as x-rays and

gamma rays [19]. Figure 8 shows the electron beam set-up that would be housed in a low-pressure chamber.

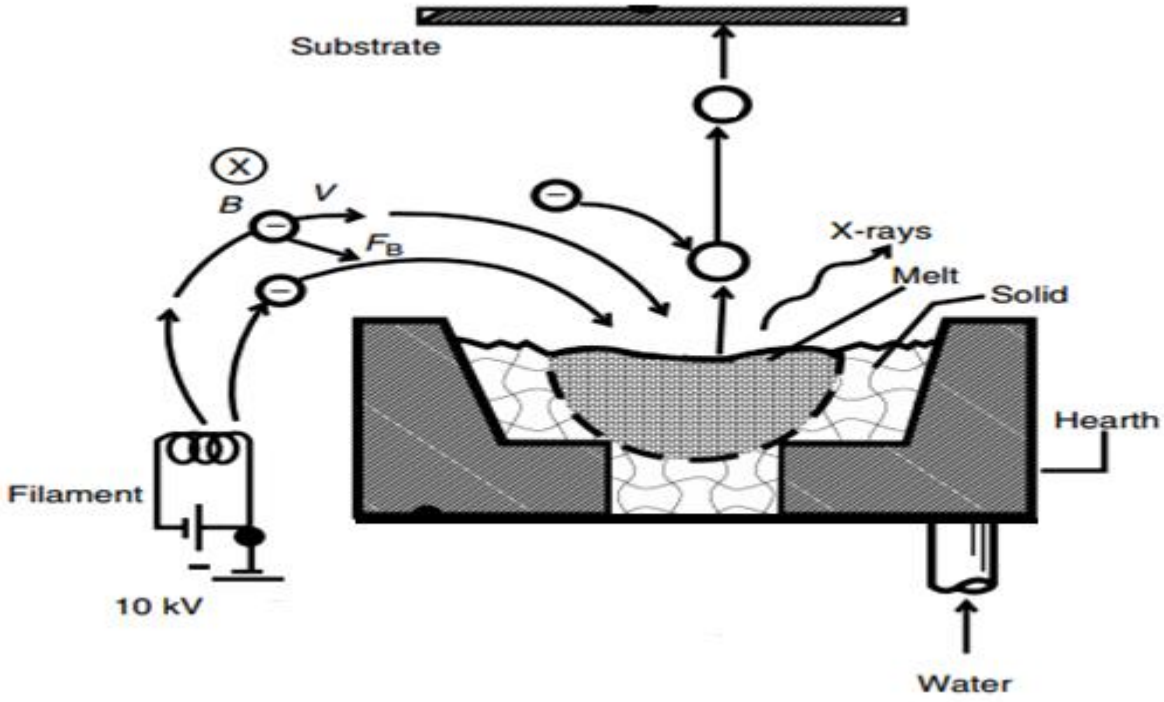

Figure 8. Electron Beam Evaporation set-up. The low-pressure housing for the set-up has not been included. Included as published in [19]

For the production of controlled, conformal, thin films, it is possible to deposit the film by producing a chemical reaction at the substrate surface. This technique is known as chemical vapour deposition (CVD). Reduced to its essence, CVD involves heating a substrate surface and the introduction of a precursor gas. The gas reacts at the surface, producing a conformal film and the remaining unreacted precursor, along with by-products are exhausted as effluent [20]. In order to produce a thin film of silica, a CVD technique known as thermal oxidation was used. This is extensively detailed in Section 3.1 of this thesis.

Proximity optical lithography involves the replication of an image from a mask to a photocatalytic polymer film, known as a photoresist, using a mask aligner. Positive photoresists experience photolysis when exposed to light in the ultraviolet to visible range allowing the exposed portion to be selectively removed by immersion in a developer. The relief image produced in the photoresist can then act as selective sites for deposition, allowing for the new film to be deposited in the likeness of the desired image. Conversely, the relief image can designate sites to be etched in the underlying film while the remaining photoresist acts as an etch-stop [19]. Bilayer lithography, including exposure and development are depicted in Figure 9.

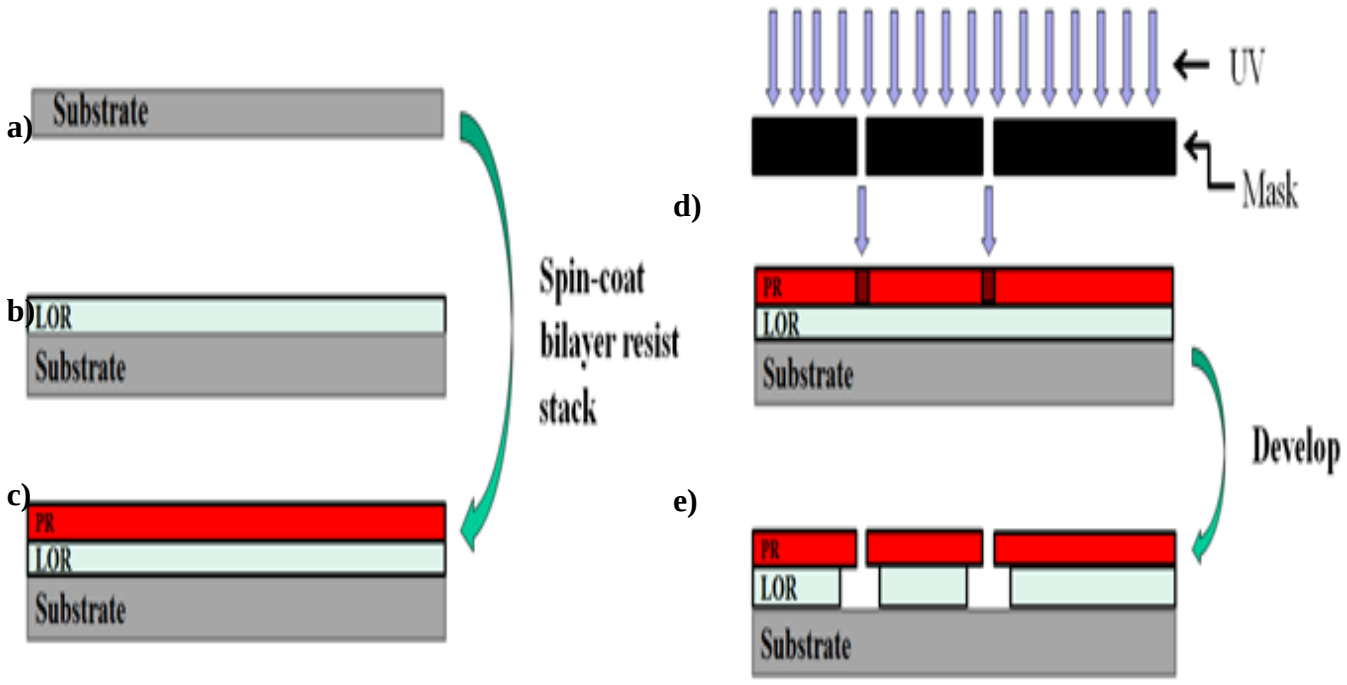

Figure 9. Schematic of bilayer lithography with positive photoresist. a) bare substrate, b) deposition of lift-off resist (LOR), c) deposition of photoresist (PR), d) exposure, e) development.

The use of the mask allows for the parallel production of many cells; optical lithography is advantaged by high throughput. However, the use of a mask imposes

optical resolution limits. For example, the minimum coherent resolution that can be realized by optical lithography is given by equation 1 [21].

$$\hat{h}_{min} = \frac{1}{2}\frac{\Lambda}{NA} \quad (1)$$

where $\hat{h}_{min}$ is the minimum coherent resolution, Λ is the wavelength of the exposure light, and *NA* is the numerical aperture of the lens through which the light passes [21].

To produce images beyond the optical resolution threshold, nanolithographic techniques like electron beam writing are required. E-beam writing involves the targeted damaging of a polymer film which results in either making it susceptible or impervious to a developer. One of the most common e-beam resists is poly (methyl methacrylate) (PMMA). Unlike optical lithography, e-beam writing cannot be done in parallel and so it is a much more time consuming process [22].

1.5 Device Overview

Three device types were fabricated in this thesis: 1] A LRSPP Bragg biosensor embedded in CYTOP, a commercially-available fluoropolymer (dielectric); 2] A silicon opto-electronic SPP modulator; and 3] SPP nanohole arrays. The fabrication techniques mentioned in Section 1.3 were applied to these three device families. Each device family relies on the excitation of SPPs using a different technique: butt-coupling, diffraction grating, and nanohole arrays, respectively. Targeted device characteristics are detailed in the following paragraphs.

The LRSPP based biosensor is comprised of gold waveguides embedded in CYTOP^{TM}, a dielectric fluoropolymer, with microfluidic channels etched into the dielectric. The waveguides are 5 μm wide and 35 nm thick. The waveguides are cladded by two approximately 8 μm thick layers of CYTOP, and it is into the upper cladding of CYTOP that the 80 μm wide microfluidic channels are etched. Fabrication of the PPBG biosensor had relatively high yield, i.e. approximately 70% of all waveguides being successfully fabricated. The structure of the biosensor is illustrated in Figure 10. Note that waveguides are either fully cladded or exposed by passing through the microfluidic channel which allows for selective functionalization of waveguides. The top and bottom cladding are symmetrical causing the device to function in the LRSPP mode. Critically, the refractive index of CYTOP closely approximates that of water [23], allowing the aqueous fluid passing through the microfluidic channels to not disrupt the optical symmetry and to render the etched channel walls “invisible”. The structures are excited by butt-coupling an aligned optical fibre to the input of the structure. The coupling efficiency depends critically on the quality of the end facets which is ensured via an externally-sourced and qualified wafer dicing service.

a)

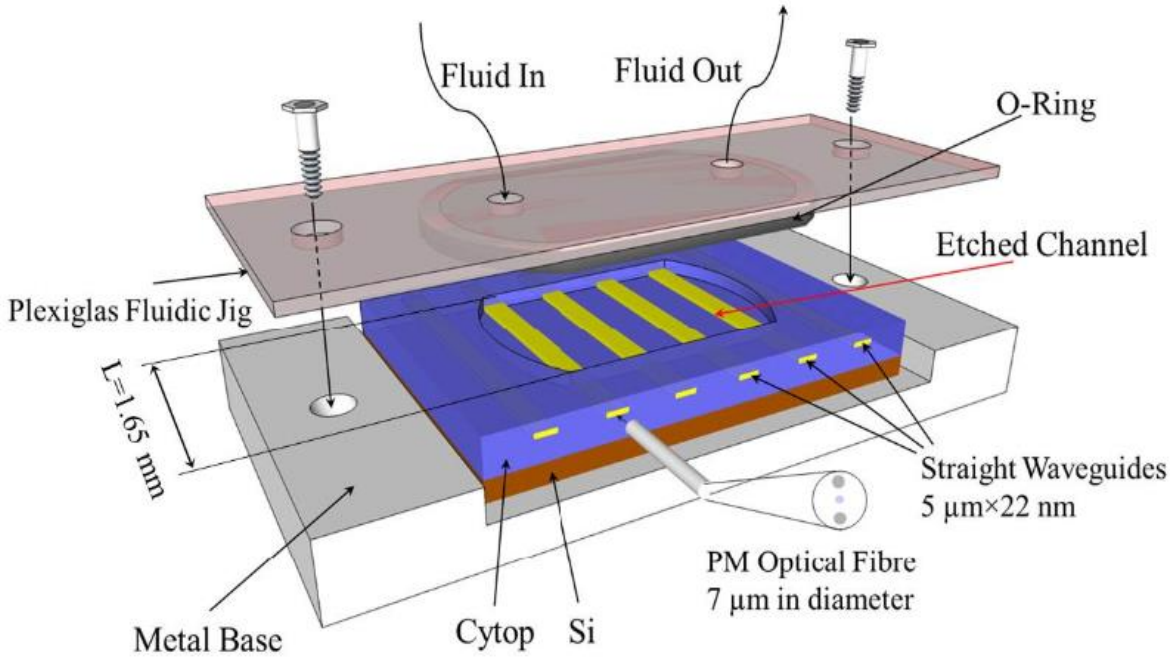

b)

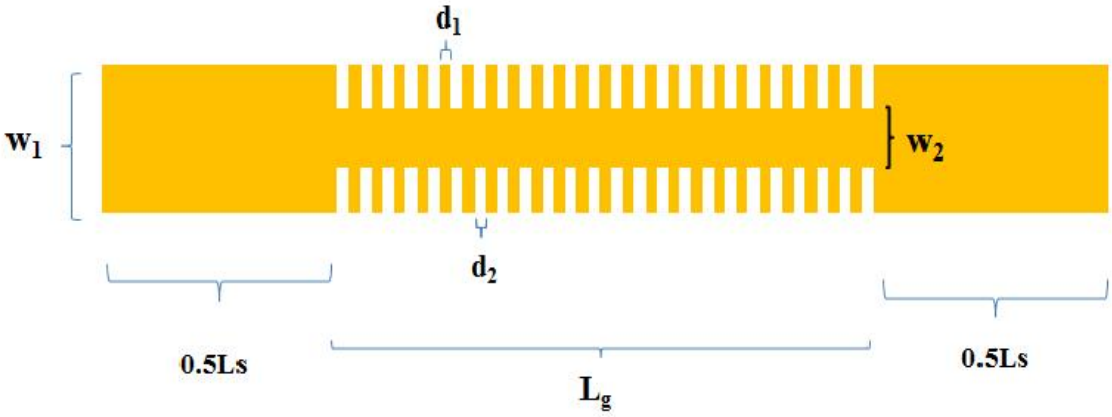

Figure 10. LRSPP biosensor with Bragg gratings. A) single biosensor with integrated fluidics (adapted from [24]). b) Top-view of waveguide with Bragg grating. $\Lambda = d_1+d_2$ is the period.

The exposed waveguides are functionalized with 16-mercaptohexadecanoic acid, a self-assembled monoloyaer (SAM). The SAM allows the waveguide to bind target analytes. The waveguides each possess a Bragg grating, the spectral characteristics of the grating is a function of the extent of binding. Successful binding

of a target analyte will cause the Bragg wavelength to shift resulting in a change in transmittance and reflectance which can be detected by the interrogation set-up. The expected sensitivity of the design was found to be high with a shift of 0.102 nm expected in the bragg wavelength when a 3 nm adlayer adheres to the surface [25].

The plasmonic modulator consists of a metal oxide semiconductor (MOS) device formed by a patterned gold SPP surface, on top of an ultra-thin (2 - 4 nm) blanket film of SiO_2, on top of a silicon wafer. Without the insulating oxide layer, an interface between a metal and a semiconductor would form a Schottky barrier [26]; with the oxide layer, a capacitor is formed. The plasmonic surface is a circle, 20 nm thick, of diameter 56, 28, 22, 17, 11, 5 or 3 μm. The plasmonic surfaces support 80 nm thick gold gratings, which are used to excite SPPs. A thick dielectric cladding of poly(methylmethacralate) (PMMA) acts as a superstrate for the waveguides and also supports a 250 nm thick, gold contact layer which allows for electrical probing of the device. The contact layer is brought into contact with the waveguide layer through metallised vias, which are perforations in the PMMA stack. See Figure 11 for an illustration of the modulator.

As previously mentioned, the MOS portion of the device constitutes a capacitor. The SPP propagates along the metal-oxide-semiconductor interfaces and the effective refractive index of the SPP is affected by the concentration of mobile carriers near the oxide-semiconductor interface via the carrier-refraction effect. By the application of a voltage to the contact layer, the capacitor can be charged into accumulation. This changes the concentration of mobile charge carriers in the semiconductor near the oxide which in turn modulates the intensity of reflected light.

If the thin-oxide layer was excluded, a similar design could be used as a photodetector. This would rely on exploitation of the Schottky barrier that is now present between the metal and the semicondcuctor, following Akbari, *et. al.* who successfully fabricated a photodetector operating with this effect [27]. Schottky detectors similar to the structure shown in Fig. 11 but without the oxide layer were fabricated during this thesis, but were omitted because their experimental characterisation is ongoing.

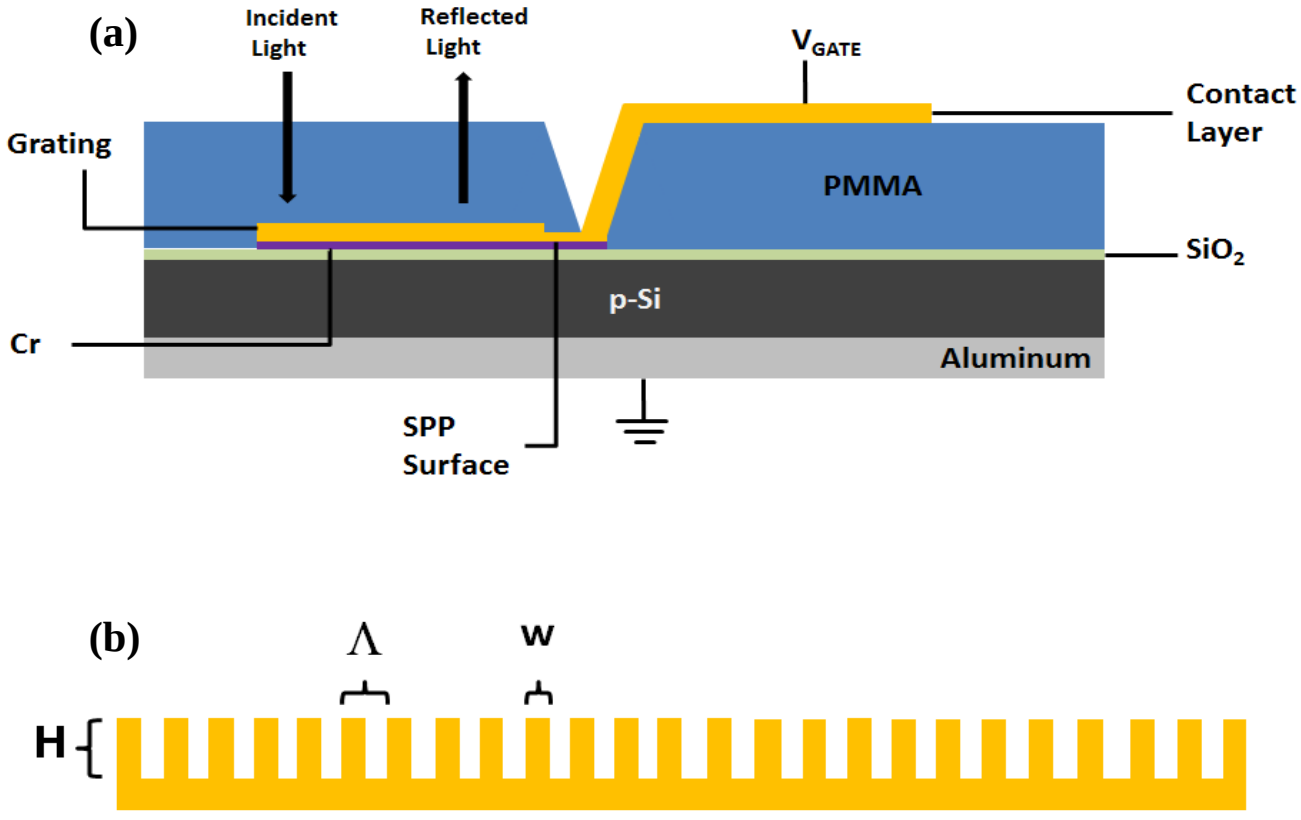

Figure 11. Plasmonic modulator. a) Overview of modulator with grating running lengthwise; b) anterior view of grating where H is the thickness of the grating, Λ is the period and w is the width. (See also Fig.1 in Section 3.1).

The nanohole array depicted in Figure 12. consists of a thin film of gold, on top of a thick CYTOP substrate. The gold was evaporated onto an oxide grown via thermal oxidation. CYTOP was then spun on the gold. The poor adhesion of gold to SiO_2 was exploited to facilitate delamination of the CYTOP/Au stack from the oxide; the gold to CYTOP bond is strong enough for the gold to remain adhered thereon. This technique allows the production of gold surfaces that have the same superior smoothness as thermally grown oxides (see Fig. 5, Section 4.1). Nanoholes are then machined through the thin metal film by a focused ion beam (FIB). Light transmitted through the nanohole array is then collected by a spectrometer. Successful transmittance through a film that should otherwise be opaque is caused by EOT and signals the presence of SPPs, excited and coupled through the nanoholes.

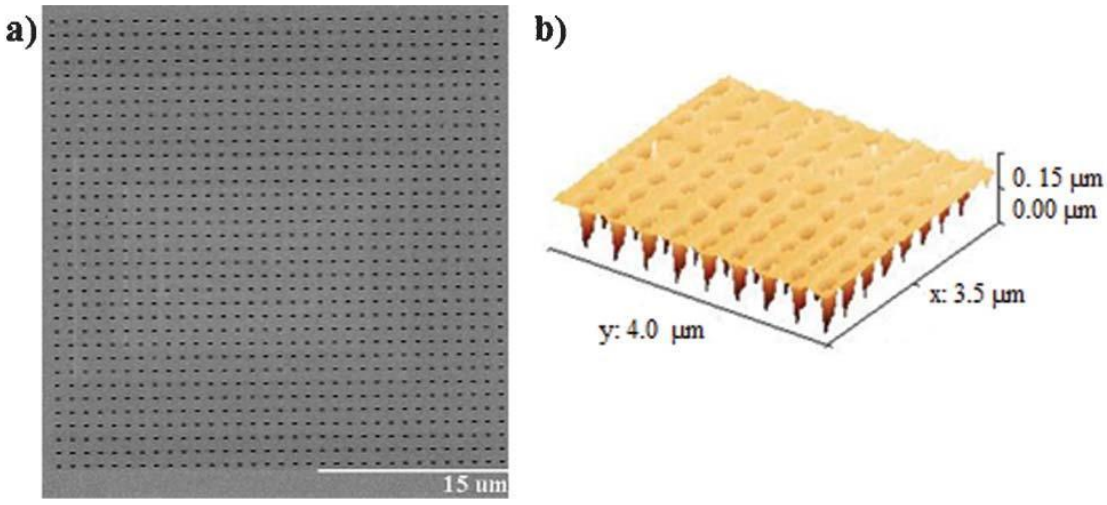

Figure 12. Elliptical nanohole arrays. a) A scanning electron microscope image of the nanohole arrays. b) An atomic force microscopy image of the nanohole arrays. Also included as Fig. 6 in section 4.1.

1.6 Thesis Structure

The thesis is comprised of a collection of articles which are all published.

Chapter 2 details the fabrication of the LRSPP based biosensor initially described in Section 1.4. Specifically, it includes fabrication improvements to the biosensor produced by Chiu [28] and Asiri [29]. The improvements are in 4 key areas: 1] Addition of Bragg gratings to waveguides, 2] increased lithographic resolution and feature definition, 3] Diminished cracking of CYTOP and photoresist during channel etch, and 4] Increased top cladding hardness.

Chapter 3 details the successful fabrication of the plasmonic modulator. Device characterization and optical measurements are also included.

Chapter 4 details the fabrication of nanohole arrays. Of note is the production of atomically smooth gold films. Collaborations between groups at the University of Victoria, the University of Ottawa and Carleton University were critical to the completion of this project.

All contributions, particularly those of the candidate, are delineated in a preamble to each of these chapters.

Chapter 5 summarises the main conclusions and contributions from this work, and suggests future work.

1.7 References Cited

[1] Maier, S.A. “Plasmonics: Fundamentals and Applications”, *Springer*, pp. 16, 21, (2007)

[2] Barnes, W.L., Dereux, A. and Ebbesen, T.W., “Surface Plasmon Subwavelength Optics,” *Nature*, vol. 424, no. 6950, pp. 824-830, (2003)

[3] Berini, P. “Plasmon-Polariton Waves Guided by Thin Lossy Metal Films of Finite Width: Bound Modes of Symmetric Structures” *Physical Review B*, Vol. 61 (15), pp. 10484, 10488. (2000)

[4] Berini, P. ‘’*Long-Range Surface Plasmon Polaritons*’’ *Advances in Optics and Photonics,* vol. 1, 484-588. (2009)

[5] Berini, P. “Plasmon-Polariton Modes Guided by a Metal Film of Finite Width Bounded by Different Dialectrics”, *Optics Express*, vol. 7 No.10, 329-335. (2000)

[6] Daviau, R., Lisicka-Skrzek, E.,Tait, R.N., Berini, P, “Broadside excitation of surface plasmon waveguides on Cytop”, *Applied Physics Letters*, vol. 94, pp. 1- 3, (2009)

[7] Geddes, C.D. “Review in Plasmonics” *Springer*, pp. 108-109 (2010)

[8] Yin, L. Vlasko-Vlasov, V.K., Rydh, A. Pearson, J. Welp, U. Chang, S-H, Gray S.K. Schatz, G.C., Brown, D.E., Kimball, C.W. “Surface Plasmons at Single Nanoholes in Au Films” Applied Physics Letters”, vol. 85 pp. 467-469 (2004)

[9] Homola, J., Koudela, I., Yee, S.S., “Surface plasmon resonance sensors based on diffracton gratings and prism couplers: sensitivity comparison,” *Sensors and Actuators B*, vol. 54, pp. 16 -24 (1999)

[10] Hu, C., Liu, D., “High-performance grating coupled surface plasmon resonance sensor based on Al-Au bimetallic layer,” *Modern Applied Science*, vol. 4 (6), pp. 9 (2010)

[11] Ditbacher, H., Krenn, J.R., Hohenau, A., Leitner, A., Aussenegg, F.R., “Efficiency of local light-plasmon coupling,” *Applied Physics Letter*, vol. 83, pp. 3665 (3), 2003

[12] Lévêque, G., Martin, O.J.F., “Numerical Study and Optimization of a Diffraction Grating for Surface Plasmon Excitation” *Proceedings of SPIE*, vol.5927, pp. 592713 (1-9) (2005)

[13] Chang, S-H., Gray, S.K, and Schatz, G.C., “Surface Plasmon Generation and Light Transmission by Isolated Nanoholes and Arrays of Nanoholes in Thin Metal Films,” *Optics Express*, vol. 13(8), pp. 3150-3165 (2005)

[14] Ebbesen, T.W., Lezec, H.J., Ghaemi, H.F., Thio, T., Wolff, P.A., “Extraordinary Optical Transmission Through Sub-wavelength Hole Arrays,” *Letters to Nature*, vol. 391, pp. 667-669, (1998)

[15] Campbell, J. Escobedo, C. Choudhury, A.I.K., Blakely, J.T., Brolo, A.G., Sinton, D., Gordon, R., “Handheld Nanohole Array Surface Plasmon Resonance Sensing Platform,” *Proc. of SPIE*, vol. 7750, pp. 1-9, (2010)

[16] Ma, H. Liu, X., He, Q., Chen, Y., Qin, W., “Theoretical treatments for the butt-coupling characteristics of fibers,” *International Journal of Optomechatronics*, vol. 6, pp. 120 – 129 (2012)

[17] Van Zant, P., “Microchip Fabrication: A Practical Guide to Semiconductor Processing,” *McGraw-Hill* (1984)

[18] Mack, C.A., “Field Guide to Optical Lithography”, *SPIE*, pp. 5 (2006)

[19] Sree Harsha, K.S., “Principles of Vapor Depositon of Thin Films,” *Elsevier Ltd*. (2006)

[20] Park, J., Sudarshan, T.S. “Chemical Vapour Deposition”, *ASM International*, (2001)

[21] Kwok-Kit Wong, A. “Resolution Enhancement Techniques in Optical Lithography” *SPIE*, (2001)

[22] Ferry, D.K., Khoury, M., Pivin Jr., D.P., Connolly, K.M., Whidden, T.K., Kozicski, M.N., Allee, D.R., “Nanolithography,” *Semiconductor Science Technology*, vol. 11, 1552-1557 (1996)

[23] “Amorphous Fluropolymer CYTOP: Technical Data”, *Asahi Glass Company*, http://www.agc.cp.jp

[24] Krupin, O., Asiri, H., Wang, C., Tait, N., Berini, P. “Biosensing Using Straight Long-Range Surface Plasmon Waveguides”, *Optics Expess*, vol. 21, No. 1, 698-709. (2012)

[25] Gazzaz, K. “Biosensing Performance of Surface Plasmon Polariton Bragg Gratings”, M.A.Sc. Thesis, *University of Ottawa*, (2014)

[26] Sze, S.M. “Physics of Semiconductor Devices” *Wiley*, (1981)

[28] Akbari, A., Tait, R.N., Berini, P., “Surface Plasmon Waveguide Schottky Detector,” *Optics Express*, vol. 18 (8), pp. 8505 – 8514 (2010)

[29] Chiu, C. “Fabrication of Surface Plasmon Waveguide Devices in CYTOP with Microfluidic Channels,” M.A.Sc. Thesis, *University of Ottawa*, (2009)

[30] Asiri, H. “Fabrication of Surface Plasmon Biosensors in Cytop”, M.A.Sc. Thesis, *University of Ottawa,* (2012)

Chapter 2

Fabrication of Long-Range Surface Plasmon-Polariton Bragg Gratings with Microfluidic Channels in Cytop Claddings

2.1 Paper published in the journal Microelectronic Engineering

Author Contributions: The paper included in this chapter was published in the journal Microelectronic Engineering and presents the fabrication of a plasmon-polariton Bragg grating biosensors embedded in Cytop. The targeted structure is a gold waveguide 35 nm thick with a Bragg grating, the waveguide width being 8 µm with grating widths of either 3, 2.5, 2, or 1.5 µm. Alternately, the waveguide width may be 5 µm with grating widths of 1.5, 1 or 0.5 µm. The waveguides are embedded in a bottom and top cladding of Cytop, both of which are 8 µm thick. Fluidic channels approximately 8 µm deep are etched into the top cladding exposing the waveguides. Device design and simulation was carried out by Kholoud Gazzaz. All optical measurements were taken by Maryam Khodami. The procedure for fabricating the Cytop bottom cladding was developed by Charles Chiu. All other fabrication steps were developed by myself under the guidance of Profs. Niall Tait and Pierre Berini. The fabrication steps that I developed are as follows: lithography, development and metallization of the waveguides, modified top cladding bakes to harden the cladding and reduce cracks, and modified fluidic channel-etch resist bake to reduce cracks.

Preamble: The fabrication of a completed plasmonic Bragg reflection grating biosensor with microfluidic channels is presented. The Bragg gratings are step-in-width designs on Au waveguides and drive stringent lithography requirements. Preliminary optical results have been successfully observed.

Fabrication of Long-Range Surface Plasmon-Polariton Bragg Gratings with Microfluidic Channels in Cytop Claddings

Sa'ad Hassan, Maryam Khodami, R. Niall Tait, Pierre Berini

Abstract

The fabrication of a novel plasmonic Bragg grating, consisting of a gold stripe lithographically stepped in width to form a waveguide Bragg grating, embedded in Cytop claddings, with an etched fluidic channel is described. The structure is designed and fabricated to be used as a compact biosensor excited via butt-coupling to an optical fibre carrying TM-polarised light. Fabrication includes Cytop bottom and top claddings, a stepped-in-width gold stripe defined by optical contact lithography, metal evaporation and lift-off, and fluidic channels etched into the top cladding via an anisotropic radical ion beam. Completed devices are presented along with preliminary optical measurements.

I. Introduction

A biosensor is a device which contains a receptor that binds a biological element, such as an antigen, antibody, whole cell or virus. The biosensor transduces the binding event into a measurable electrical or optical signal [1]. Biosensors have been produced which detect, *e.g.*, glucose in blood, drugs in serum, and neurodegenerative causative proteins [2]. The need for sensitive, compact and low-cost biosensors motivates research on high-sensitivity planar optical biosensors that can be fabricated using wafer-scale processes and standard tools. Surface

plasmon-polaritons (SPPs) are transverse electromagnetic (EM) waves coupled to charge density oscillations which propagate at the interface between a metal and a dielectric at optical wavelengths [3]. SPPs are commonly excited and used as transducer waves in optical biosensors because of their high surface sensitivity. Once appropriately functionalised, the metal surface supporting SPPs becomes selective to a target analyte, and as analyte binds, the properties of the SPPs are altered, producing a change in the measured output in an appropriately designed structure [3].

If a thin metal film is used and cladded by dielectrics that are symmetric, *i.e.* that have a similar refractive index on both surfaces of the metal film, then SPPs that propagate as far as several centimeters can be excited. Such SPPs are known as long-range surface plasmon-polaritons (LRSPPs) [4]. LRSPPs on thin gold planes [5-10] and stripes [11-14] have been used for biosensing, as they hold the promise of better sensing performance compared to single-interface SPPs due to their longer optical interaction length with the sensing surface [15]. Stripes are advantageous compared to planes because they enable compact integrated geometries [4].

An integrated optic geometry operating with LRSPPs, of strong interest for biosensing, consists of a waveguide grating implemented as a gold stripe periodically stepped-in-width over a length - a plasmon-polariton Bragg grating (PPBG). Such structures have been demonstrated previously as narrowband passive filtering elements [16] (as have step-in-thickness structures [17]). A PPBG reflects a portion of the input wave at the Bragg wavelength due to additive reflections at each unit cell along the structure. As the reflection is phase-sensitive, a biosensor can be implemented by exposing the PPBG in a microfluidic channel and

allowing biomaterial to bind to its surface thereby modifying the phase of the LRSPPs, which results in shifting the Bragg wavelength of the structure. Such a biosensor is therefore phase sensitive, as opposed to biosensors based on a uniform metal stripe which is loss sensitive [12-14]. Recent modelling validates the concept of a PPBG biosensor operating with LRSPPs and provides good designs for the structure [18]; high surface sensitivity is expected combined with a narrowband spectral response enabling accurate tracking of the reflection peak (or transmission dip). In this paper, the fabrication of PPBG structures in Cytop claddings with an etched microfluidic channel is presented and initial optical measurements demonstrating Bragg operation with LRSPPs are reported.

II. Device Structure and Fabrication Process Flow

The biosensor consists of a structured thin Au film cladded in Cytop, a fluoropolymer [19]. Cytop is of interest as a cladding material because it has a refractive index close to that of water which constitutes many of the sensing media of interest - this property is advantageous because it enables the propagation of LRSPPs which require that the refractive index of the media bounding the Au film be similar (*i.e.*, the structure must be optically symmetric), and it enables optically non-invasive microfluidic channels once filled. Cytop has low optical absorption and it has been used to create dielectric optical waveguides [20-22] and LRSPP waveguides [12-14].

The structure of interest is depicted in Figure 1, and consists of a 35 nm thick Au stripe bounded by bottom and top Cytop claddings of equal thickness of approximately 8 μm each. A PPBG of length L_g is concatenated to uniform input and

output waveguides, each of length $0.5L_s$, to excite the structure and extract light emerging from its output. Target dimensions for the PPBGs were determined through modelling [18] such that the Bragg wavelength would fall near λ_0 = 1550 nm. A range of periods and steps-in-width are thus of interest: Λ = 1690 to 1800 nm ($d_1 = d_2$), and W_1 = 8 μm with W_2 ranging from 2 to 5 μm. Operating at shorter wavelengths (say near λ_0 = 850 nm) would enable a more sensitive and compact device [18], but the grating period would decrease, challenging photolithography. A fluidic channel is etched into the top cladding exposing the PPBG, readying the device for biosensing. The structure propagates LRSPPs which are excited by butt-coupling to an optical fibre. Sensing could then be achieved by measuring changes in, *e.g.*, the transmittance spectrum of the structure near the Bragg wavelength as analyte binds to the surface of the PPBG [18].

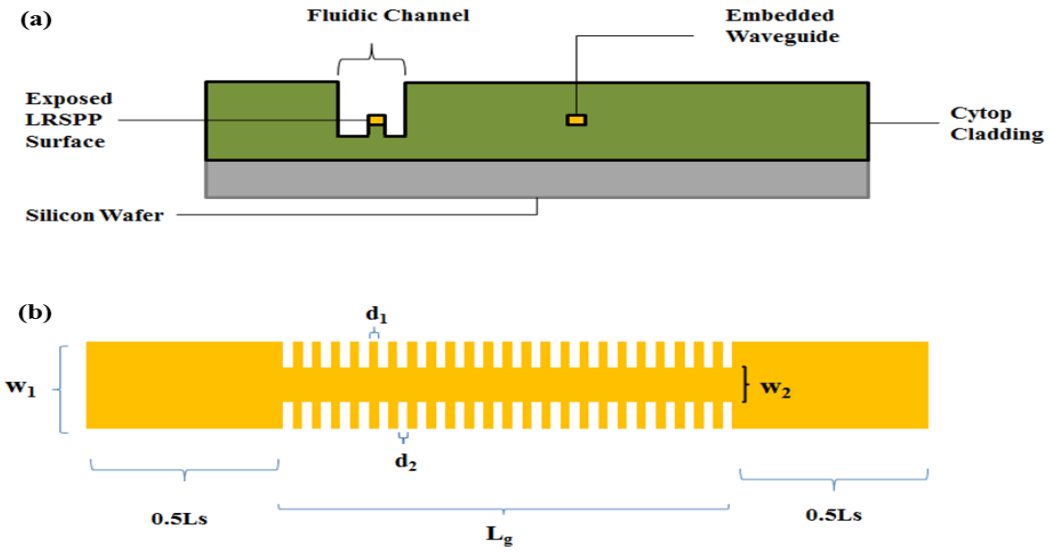

Figure 1. (a) Front cross-section of the Cytop-cladded LRSPP biosensor. (b) Top view of a Au waveguide PPBG consisting of steps in width (W_1, W_2) of period Λ defined as $\Lambda = d_1+d_2$. The PPBG of length L_g, is flanked by two access waveguides, each of length 0.5Ls.

An overview of the fabrication flow is depicted in Figure 2. Fabrication of the device proceeds in several steps: Wafer selection and cleaning, bottom cladding deposition, lithography and metallization of the PPBG and waveguides, top cladding deposition, fluidic channel etching, and top cladding long-bake. The PPBG biosensor poses several fabrication challenges, primarily, stringent lithographic resolution and the need to form the top Cytop cladding without destroying the embedded metallisation while ensuring that the cladding does not crack or remain tacky. The fabrication flow and process steps build on previous work with these materials [23,24].

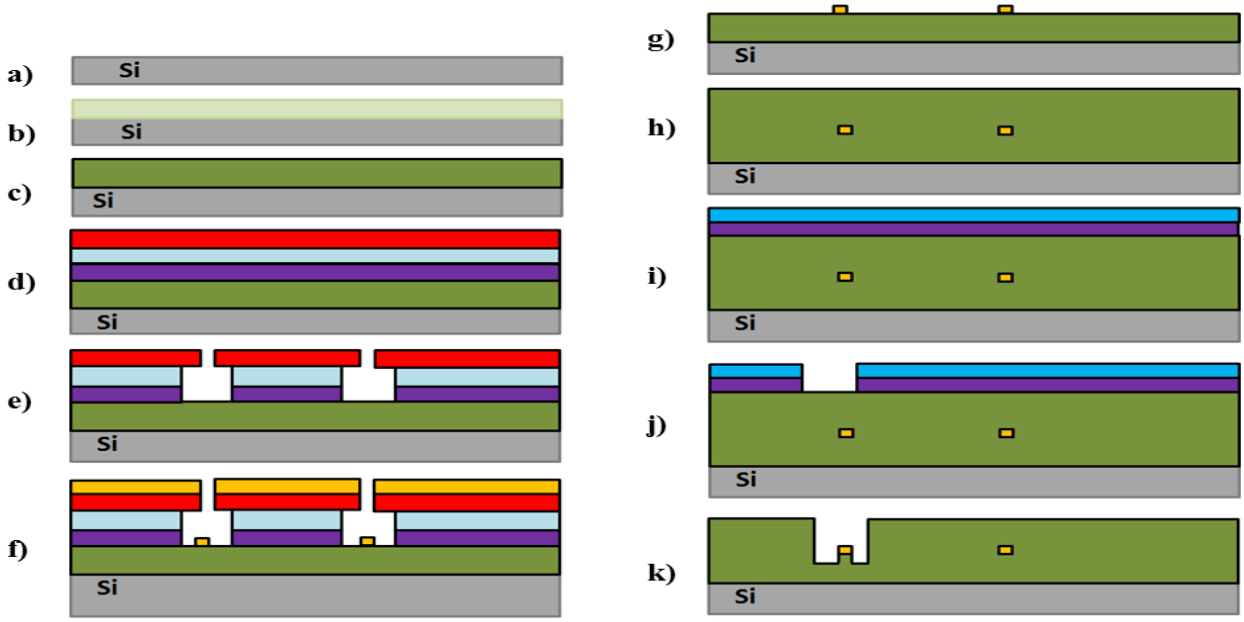

Figure 2. Fabrication process flow. (a) Selection of the supportive silicon wafer, (b) deposition and soft-bake of Cytop bottom cladding, (c) hard-bake of Cytop bottom cladding, (d) priming of Cytop surface (purple) for spinning of bi-layer LOR/resist stack (light blue, red), (e) exposure and development, (f) metallization of gold film, (g) lift-off and dehydration, (h) deposition of Cytop top cladding, (i) priming (purple) and spinning of fluidic-channel etch resist (blue), (j) alignment, exposure through fluidic channel mask, and development, and (k) fluidic-channel etch.

III. Fabrication Details

3.1 Wafer Selection and Bottom Cladding

Fabrication begins with a 4 inch p-type (100) silicon wafer, which is dipped in a 10% HF solution to etch away any native oxide. The wafer is then placed in an Oxygen reactive ion etch (RIE) in a Plasmatic plasma-preen II 862 to clear any remaining organic molecules on the surface of the wafer and dehydrate it. The power, pressure, and oxygen flowrate of the RIE are 100 W, 350 Torr and 44 sccm, respectively.

Once the wafer preparation steps have been completed, the Cytop bottom cladding can be deposited. To ensure adequate smoothness, it is necessary to produce the Cytop bottom cladding via multiple coats that are spun at high spin speeds. The bottom cladding fabrication procedure is detailed in Table 1. The first layer of the bottom cladding is CTL-809M “M-grade” Cytop which has superior adhesion to silicon and metals due to its amino-silane functional groups [19]. This layer contributes 0.4 μm to the bottom cladding thickness. The following three layers constitute the optically infinite Cytop stack and are comprised of CTX-809SP2, i.e. optical quality “S-grade” Cytop. Each of these layers is 2.35 μm thick. Finally, the bottom cladding is topped with a diluted s-grade smoothing layer. A final 5% s-grade layer is sun on top of the stack to improve the smoothness of the surface. This final layer contributes 1.4 μm to the bottom cladding thickness. The bottom cladding therefore has a total thickness of 8.8 μm.

Table 1. Deposition of the bottom cladding

Step	Description	Details
1	Adhesive Layer	Spin 5 wt% solids CTL-809M, 500 rpm for 10 s followed by 1000 rpm for 20 s. Soft-bake layer on hotplate for 30 minutes at 50 C
2	Bulk Layers	Spin 9 wt% solids CTX-809SP2, 1000 rpm for 10 s followed by 1500 rpm for 20 s. Soft-bake layer on hotplate for 30 minutes at 50 C. Repeat twice
3	Smoothing layer	Spin 5 wt% solids CTX-809SP2, 1000 rpm for 20 s. Soft-bake layer on hotplate for 30 minutes at 50 C
4	Hard-Bake	Ramp at 150 C/hr to 200 C and then hold for 2.5 hours.

3.2 Plasmon-Polariton Bragg Gratings

Once the bottom cladding is fully deposited, fabrication of the waveguide layer can begin. Cytop presents a highly hydrophobic surface which is inimical to many lift-off resists (LOR) and so requires two priming steps to ensure proper adhesion of the LOR. First, the wafer is subjected to an oxygen-radical ashing step, which briefly renders the Cytop surface hydrophilic. The ashing step involves exposing the bottom cladding surface to an anisotropic RIE (March Systems Jupiter II bench-top etcher). The wafer must then be primed with a hexamethyldisilazane (HMDS) adhesion layer. These two steps must immediately precede LOR deposition due to the transience of the electrostatic charge and HMDS monolayer. The procedure for the fabrication of the PPBG metallisation is detailed in Table 2.

Table 2. Photolithography, Metallization and lift-off of PPBGs

Step	Description	Details
1	Ash	30 s in reactive-ion etcher (RIE) at 100 W with O_2 flow of 100 sccm

2	Deposition of HMDS	Place in HMDS oven at 97 °C
3	Deposition of LOR	Spin coat of Michrochem PMGi SFG 2S
4	Deposition of PR	Spin coat of Microposit S1805
5	Exposure	12 s exposure with Karl Suss MA 6 contact mask aligner
6	Development	Develop for 1 min 40 s in Microposit MF-321 with aggressive agitation
7	Rinse	Flush rinse with de-ionized (DI) water
8	Metallization	Thermal deposition of 35 nm Au
9	Lift-off	5 minute static dip in Microposit 1165 followed by 10 s ultrasonic. Repeat once. Static IPA and DI water baths for 10 min each. Finally, dry in N_2
10	Dehydration	Leave on hotplate at 95 °C for 15 min

The PPBG steps-in-width are extremely fine and tax the limits of optical lithographic resolution. E-beam writing is available but was avoided because of the high cost associated with this process and the difficulties of writing on thick Cytop (which is insulating). A technique that could produce many waveguides in parallel was desired therefore we selected optical contact lithography and attempted to refine the resolution of features as much as possible.

PPBGs of varying dimensions were attempted in order to have a broad design space. This would allow for analysis of the relationship between design and performance. A typical fabricated PPBG is shown in Figure 3. The design duty cycle of the gratings is 50%, the inner stripe width (w_2) should be 3 μm, the outer stripe width (w_1) should be 8 μm and the period (Λ) should be 1.8 μm. From optical microscope inspections, the design targets seem to have been achieved in this structure except for w_2 which was fabricated as 4.5 μm. Slight rounding of the features is also noted due to the limited resolution of the lithography process.

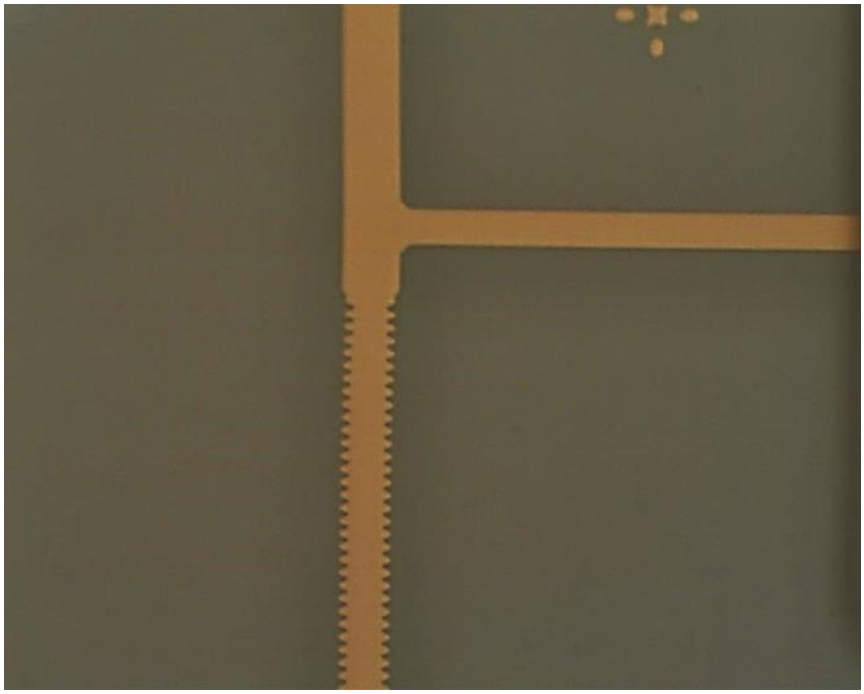

Figure 3. Microscope image of a PPBG. The dimensions of the grating are Λ = 1.8 µm, w_1 = 8 µm, w_2 = 4.5 µm.

3.3 Top Cladding

Previous fabrication of the top-cladding produced a smooth cladding which minimally deformed the waveguides. However, the top-cladding remained tacky because it retained too much solvent [23, 24]. On the other hand, if the solvent content is too low, the dielectric becomes stiff and prone to cracking during the channel etch. To address these concerns a new top cladding procedure was developed which minimizes the degree of waveguide deformation, Cytop tackiness, and crack formation. The procedure for baking the Cytop top cladding is presented in Table 3. The top cladding consists of 6 layers, each spun at 1000 rpm for 10 seconds followed by 4000 rpm for 20 seconds to produce layers 1.35 µm thick.

Table 3. Baking Procedure for Cytop Top Cladding

Step	Description	Details
1	First Layer	Soft bake at 50 °C for 30 minutes then ramp at 5 °C/hour to 100 °C and hold for 24 hours[a]
2	Second Layer	Soft bake at 50 °C for 30 minutes then ramp at 10 °C/hour to 100 °C and hold for 24 hours[a]
3	Third to Sixth Layers	Soft bake at 50 °C for 30 minutes. Then ramp at 25 °C/hour to 100 °C and hold for 2 hours

[a] – The long, slow bake produces an effective barrier against solvent ingress

Once the sixth layer is deposited, the biosensor is ready for fluidic channel lithography and etching. The bake procedure detailed in Table 3 provides a top cladding that has minimally deformed the PPBGs and waveguides and moreover that is soft enough to inhibit cracking during the channel etch. After the channel etch, the wafer is subjected to a week-long bake at 100 °C to harden the Cytop cladding.

3.4 Reduction of Cracks in the Cytop Cladding and Fluidic Channel Etch

Cracking in the Cytop cladding has been observed and documented in earlier publications [23,24]. Cracking in the Cytop cladding has four possible sources: 1) Expulsion of solvent from the top cladding during baking, 2) nucleation from errant particles or gold flakes embedded in the cladding, 3) imprinting of cracks from the fluidic-channel etch resist, and 4) drying out the top cladding excessively before exposing it to shearing pressure during the fluidic-channel etch. The first cause has already been addressed by Chiu [23] and cause (4) was addressed in the previous subsection. Modifications to the fluidic-channel etch resist are presented which

address the other three causes. These modifications result in a further decrease in the propagation of cracks.

As mentioned in the previous paragraph, any particle that embeds in the Cytop can act as a nucleation site for cracks. Gold flakes or particles that are removed during lift-off and that re-deposit on the bottom-cladding become difficult to remove once extracted from the stripper bath (Microposit Remover 1165). It is therefore important to ensure that no gold particles re-deposit on the wafer surface during extraction from the stripper. Agitating the wafer as it is removed from the bath and gently swabbing any gold flakes that linger are critical to producing a clean, particle-free surface.

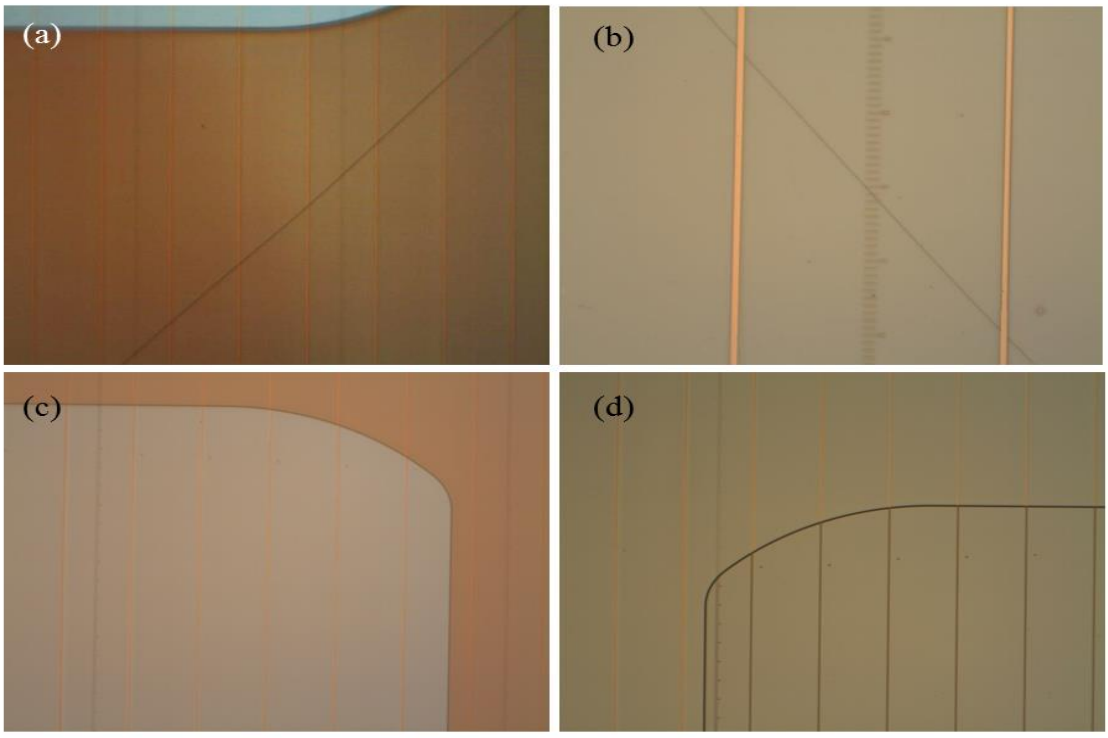

Figure 4. (a) Crack in the fluidic-channel etch resist. (b) A crack in the Cytop cladding induced by the etch resist. (c) Etch resist deposited using the new procedure - the absence of cracks is noted. (d) Fully etched fluidic channel lacking any cracks.

When the fluidic-channel etch resist is being deposited, it is susceptible to cracks. Notably, these cracks will be transferred into the Cytop cladding during etching and so it is critical that the etch resist be crack-free. Figures 4(a) and (b) show a crack in the fluidic-channel etch resist (Megaposit SPR 220-7.0) and a crack induced by the resist into the underlying Cytop cladding. A procedure for producing an etch resist free of cracks was required and is detailed in Table 4. An outgassing step was included to avoid rapid expulsion of solvent during baking. Further, slow temperature ramps up and down were included to prevent thermal shock.

Table 4. Photolithography of Fluidic Channels

Step	Description	Details
1	Ash	30 s in reactive-ion etcher (RIE) at 100 W with O_2 flow of 100 sccm
2	Deposition of HMDS	Place in HMDS (Hexamethyldisilizane) oven at 97 °C
3	Deposition of PR	Spin coat of Megaposit SPR 220-7.0
4	Outgas PR	Maintain wafer and PR at room temperature for 30 minutes.
5	Soft-Bake	Ramp wafer to 100 °C on a hotplate and then hold for 1 hour. Finally, turn off the hot-plate and allow wafer to gradually cool on the hot-plate back to room temperature.
6	Exposure	99 s exposure with Karl Suss MA 6 contact mask aligner
7	Moisturization	Leave resist at room temperature for 24 hours
8	Post-Exposure Bake	Place on 115 °C hotplate for 90 s
9	Development	Develop for 1 min 40 s in Microposit MF-24A with aggressive agitation
10	Rinse	Flush rinse with de-ionized (DI) water
11	Dehydration	Leave on hotplate at 95 °C for 15 min

Proper etching of the fluidic channels is vital to the device's operation as a biosensor. Care must be taken to align the channels to the appropriate waveguides and greater care must be taken to ensure that the waveguides in the fluidic channels are fully exposed, *i.e.* cleared of all covering Cytop. We have therefore developed a process that slightly over-etches the fluidic channels using the Au features as an etch stop. The Au features will therefore be raised slightly from the bottom of fluidic channel, resting on a Cytop pedestal. It is important for the pedestals to be short in order to ensure the mechanical rigidity of the structures.

After the fluidic channel resist is deposited and developed as per Table 4, the device is ready for channel etching. The channel etch procedure is detailed in Table 5. During the channel etch, the sample is profiled (Tencor P-1 Long scan profiler) to check for waveguide exposure. The profilometer stylus is programmed to scan across a waveguide, and if a smooth, bump-free surface is observed then the waveguide is assumed to be still embedded in the top cladding. On the other hand, if a thin, 5 micron wide bump that is 150 to 500 nm high, is observed, then it is evident that the waveguide has been exposed. Profilometry scans from at least 5 different regions of the wafer, *i.e.* north, east, south, west, and centre, are performed to verify that all waveguides across the wafer have been exposed to an appropriate depth.

Table 5. Fludic-Channel etch procedure

Step	Description	Details
1	Etch Parameters	Etch device in RIE at 200 W, 300 mTorr and 44 sccm O_2
2	First etch	2 minutes in one orientation. Open RIE chamber, rotate wafer 90. Repeat until wafer has been rotated 360 and been etched for 8 minutes.
3	Profile	Check for waveguide exposure in profilometer. If waveguides are exposed then etch is complete, otherwise continue to step 4.
4	Second Etch	1 minute etch in original orientation.
5	Profile	Check for waveguide exposure in profilometer. If waveguides are exposed then etch is complete, otherwise continue to step6.
6	Third Etch	30 second etch rotated at 90

Figure 5 depicts a completed device. The specified design dimensions are Λ = 1.8 µm, w_1 = 8 µm, w_2 = 2 µm. All dimensions were achieved apart from w_2 which was fabricated as 2.8 µm. A duty cycle of about 50% was achieved, in line with the design specifications. The lateral contact arm and large pad apparent in Fig. 5(b) are optically non-invasive and have been added in order to eventually carry out thermo-optic measurements on the gratings.

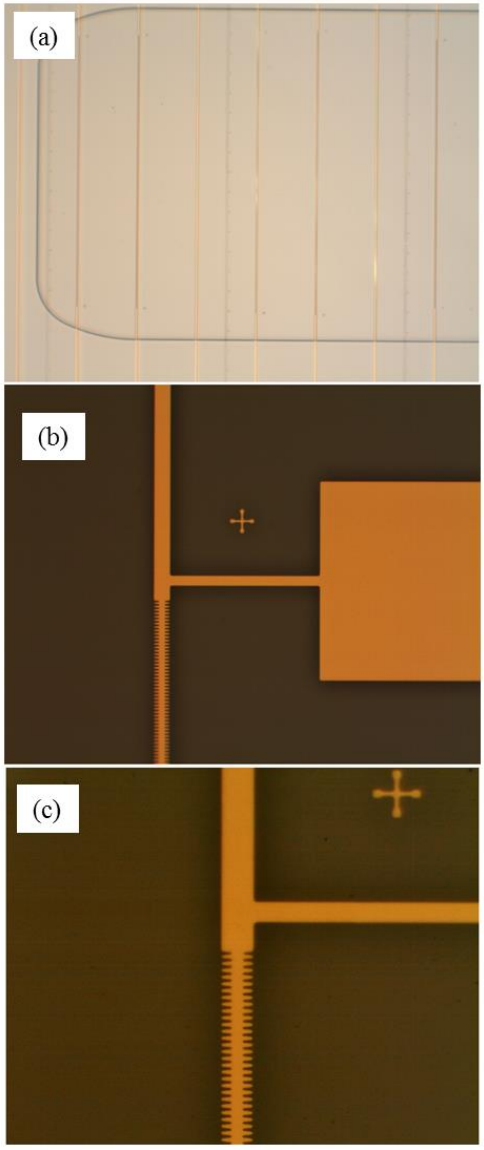

Figure 5**.** Completed Devices. (a) A channel with PPBGs and access waveguides. (b) A 500X magnification image of a waveguide within the same channel. Note the presence of a concatenated access waveguide and an electrical contact pad. (c) Increased magnification of waveguide shown in (b). The dimensions of the grating are Λ = 1.8 µm, w_1 = 8 µm, w_2 = 2.8 µm.

IV. Optical Measurements

The experimental setup used for the preliminary characterization of PPBGs is presented in Fig. 6. The setup is used to capture the infrared mode output of the device under test (DUT) and to measure its insertion loss and transmittance over wavelength. The setup consists of a tuneable laser operating in the 1500 nm range.

The DUT is excited through a polarization maintaining single mode input fibre carrying TM-polarised light butt-coupled to the input. The transmitted power from the output of the device is first collimated using a 25× objective and after passing through the aperture, impinges on a 50:50 beam splitter. Half of the beam is then captured by an optical power meter, while the other half is captured by an IR camera to produce a mode output image.

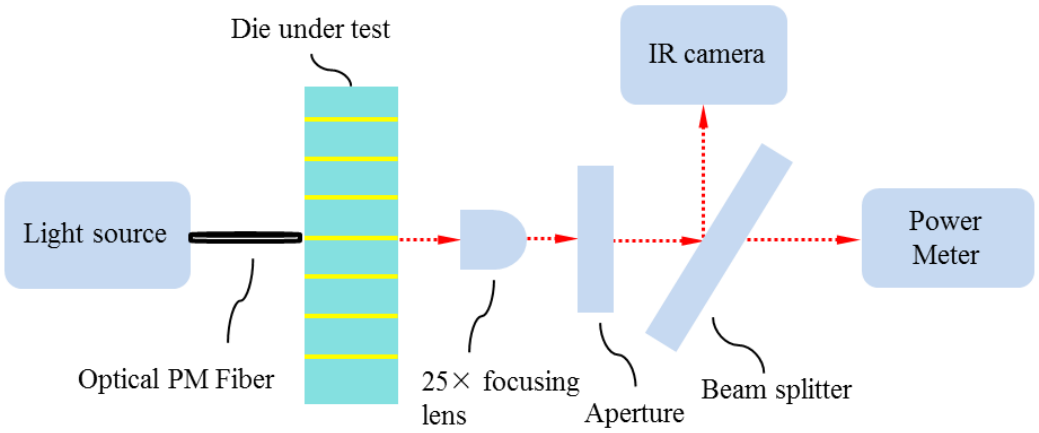

Figure 6. Optical setup used to measure the insertion loss and transmittance of a PPBG.

The attenuation and coupling loss of uniform waveguides (no PPBG) were measured first using the cutback technique [16], where the measured insertion loss of a series of uniform waveguides is plotted as a function of waveguide length. A linear regression model can then be used to determine waveguide parameters. Fig. 7 plots the measured insertion loss of four cladded uniform waveguides of various lengths (2, 2.8, 3.8 and 4.8 mm) along with the best-fitting linear model (R^2 = 0.9997). An input coupling loss of C_c = 1.78 dB (intercept) and a mode power attenuation of MPA_c = 5.83 dB/mm (slope) are obtained from the linear model. The

measured MPA is slightly larger than the theoretical value of 4.4 dB/mm expected for an 8 μm wide 35 nm thick stripe [18]. However, the measured input coupling efficiency is about 6× higher than the expected value of 0.3 dB; this is probably due to facet imperfections caused by dicing and by stubborn particulate matter that remained thereon post cleaning.The inset to Fig. 7 gives the mode output for a straight waveguide, revealing a well-confined mode with little background radiation. MPA measurements for etched waveguides filled with index-matched fluid have been obtained in similar structures [25], where it was observed that the MPA can be almost 2× larger than in fully cladded waveguides.

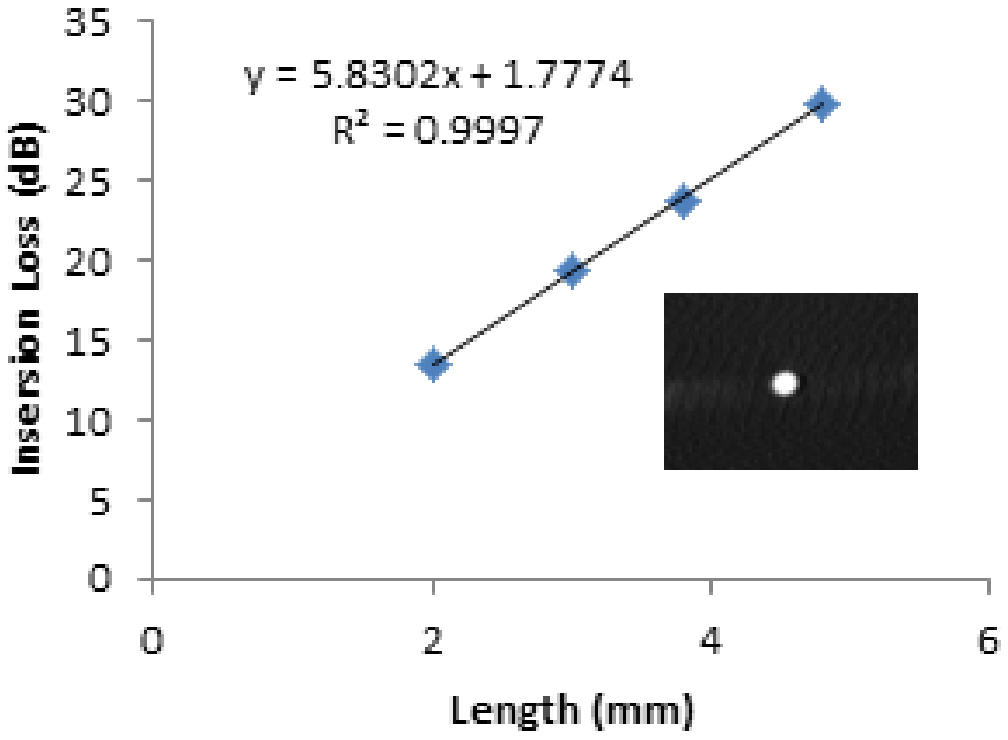

Figure 7. Cutback measurements at λ_0 = 1550 nm for a series of uniform 8 μm wide waveguides of different length.

Fig. 8 shows the measured transmittance response of a cladded PPBG (no fluidic channel) having a target Au thickness of 35 nm (unverified) and target dimensions of w_1 = 8 μm, w_2 = 2 μm, Λ = 1740 nm and L_g = 1.4 mm. The effects of the access lines and input fiber-chip coupling were removed from these measurements by applying the de-embedding process described in [16]. In this process the measurement reference planes are shifted from the input and output of the chip to the input and output of a PPBG, yielding the transmittance of the PPBG only (in dB) as follows:

$$T = P_{Meas} - P_{Cal} - MPA_c\left(L_s - L_g\right) - C_c \quad (1)$$

In Eq. (1), P_{Meas} is the measured transmitted power (in dBm), P_{Cal} is the power measured during the calibration process (in dBm), MPA_c is the mode power attenuation of the access waveguides (in dB/mm), and C_c is the coupling loss between the fibre and access waveguide at the input of the chip (in dB). The lengths L_s and L_g (in mm) are defined in Fig. 1(b) and are L_s = 0.6 mm and L_g = 1.4 mm (the die length was 2 mm). On the assumption that all PPBGs have identical access waveguides, the values for MPA_c and C_c were taken as the results of the cutback measurements given in Fig. 7.

This PPBG was designed to produce a Bragg response at 1548.4 nm over a FWHM bandwidth of 0.9 nm and a corresponding transmittance dip of 5.4 dB relative to the out-of-band transmittance. The measured response reveals a Bragg wavelength of 1559.5 nm, a bandwidth of ~ 1 nm, and a transmittance dip of ~ 1.5

dB. The inner width in the realised structure was w_2 ~ 3.2 μm rather than the target width of w_2 = 2 μm, and the steps-in-width were rounded due to the limited resolution of optical lithography (*e.g.*, Figs. 3 and 5(c)) rather than rectangular as designed (Fig. 1(b)). Both of these effects would cause the grating to be weaker than modeled explaining in part the smaller measured transmittance dip. The measured Bragg wavelength is red-shifted relative to the theoretical value by ~ 11 nm. This could be caused by discrepancies in the metal thickness and in the optical parameters used to model the materials, and as discussed in [16], in a discrepancy in the realised period. Nonetheless, the results are in sufficient agreement to validate the process developed, although improvements are required to obtain better quantitative agreement with theory.

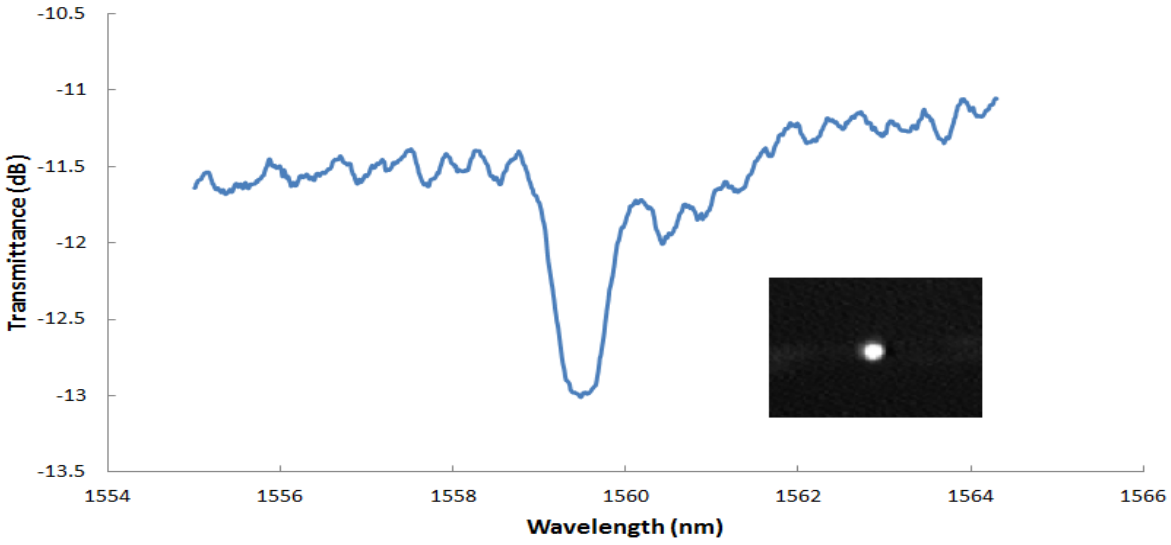

Figure 8. Measured transmittance response of a PPBG (die C82T, wafer 4D1A). The output mode (on resonance) captured by the IR camera is shown as the inset.

V. Conclusions

A fabrication process for realising Au waveguide PPBGs in Cytop operating with LRSPPs has been described and successfully implemented. The process includes bottom cladding deposition, optical lithography and metallization by lift-off of Au PPBGs and waveguides, top cladding deposition, and fluidic channel etching. Structures designed for operation at free-space optical wavelengths near 1550 nm have been fabricated and tested. Preliminary optical measurements corroborate qualitatively design expectations and fabrication quality. Additionally, fabrication improvements to previous processes developed for LRSPP biosensors in Cytop have been proposed and implemented. These improvements eliminate cracks in the Cytop top cladding and tackiness in the biosensor.

References

[1] A. Sadana, Fractal Binding and Dissociation Kinetics, Elsevier, 2005.

[2] A. Sadana, N. Sadana, Handbook of Biosensors and Biosensor Kinetics, Elsevier 2011.

[3] E. Wijaya, C. Lenaerts, S. Maricot, J. Hastanin, S. Habraken, J.-P. Vilcot, R. Boukherroub, S. Szunerits, Surface plasmon resonance-based biosensors: From the development of different SPR structures to novel surface functionalizion strategies, Current Opinion Solid State and Materials Science 15, (2011) 208-224.

[4] P. Berini, Long-range surface plasmon polaritons, Adv. Opt. Phot 1 (2009) 484-588.

[5] A. R. Wark, H. J. Lee, R. M. Corn, Long-range surface plasmon resonance imaging for bioaffinity sensors, Anal. Chem. 77 (2005) 3904-3907.

[6] R. Slavík, J. Homola, Ultrahigh resolution long range surface plasmon-based sensor, Sens. Actuators B 123 (2007) 10-12.

[7] J. Dostálek, A. Kasry, W. Knoll, Long range surface plasmons for observation of biomolecular binding events at metallic surfaces, Plasmonics 2 (2007) 97–106.

[8] J. Guo, P. D. Keathley, T. J. Hastings, Dual-mode surface-plasmon resonance sensors using angular interrogation, Opt. Lett. 33 (2008) 512–514.

[9] M. Vala, S. Etheridge, J. A. Roach, J. Homola, Long-range surface plasmons for sensitive detection of bacterial analytes, Sens. Actuators B 139 (2009) pp. 59–63.

[10] V. Chabot, Y. Miron, M. Grandbois, P. G. Charette, Long range surface plasmon resonance for increased sensitivity in living cell biosensing through greater probing depth, Sens. Actuators B 174 (2012) pp. 94-101.

[11] Y. H. Joo, S. Song, R. Magnusson, Demonstration of long-range surface plasmon-polariton waveguide sensors with asymmetric double-electrode structures, Appl. Phys. Lett. 97 (2010) 201105.

[12] O. Krupin, H. Asiri, C. Wang, R. N. Tait, P. Berini, Biosensing using straight long-range surface plasmon waveguides, Optics Express 21 (2013) 698-709.

[13] O. Krupin, C. Wang, P. Berini, Selective capture of human red blood cells based on blood grouping using long-range surface plasmon waveguides, Biosens. Bioelectr. 53 (2014) 117-122.

[14] W. R. Wong, O. Krupin, S. D. Sekaran, F. R. M. Adikan, P. Berini, Serological detection of Dengue infection in blood plasma using long-range surface plasmon waveguides, Anal. Chem. 86 (2014) 1735–1743.

[15] P. Berini, Bulk and surface sensitivities of surface plasmon waveguides, New J. Phys. 10 (2008) 105010.

[16] S. Jetté-Charbonneau, R. Charbonneau, N. Lahoud, G. Mattiussi, P. Berini, Bragg gratings based on long-range surface plasmon-polariton waveguides: comparison of theory and experiment, IEEE J. Quant. Electr. 41 (2005) 1480-1491.

[17] A. Boltasseva, S. I. Bozhevolnyi, T. Nikolajsen, K. Leosson, Compact Bragg Gratings for Long-Range Surface Plasmon Polaritons, J. Lightwave Technol. 24 (2006) 912-918.

[18] K. Gazzaz, P. Berini, Theoretical biosensing performance of surface plasmon polariton Bragg gratings, Applied Optics (in press).

[19] Amorphous Fluoropolymer CYTOP, Asahi Glass Co., Ltd, http://www.agc-cytop.com/, January 2009.

[20] Y. G. Zhao, W.-K. Lu, Y. Ma, S.-S. Kim, S. T. Ho, T. J. Marks, Polymer waveguides useful over a very wide wavelength range from the ultraviolet to infrared, Appl. Phys. Lett. 77 (2000) 2961-2963.

[21] Y. Kuwana, S. Takenobu, K. Takayama, Y. Morizawa, High-performance and low-cost optical waveguide module made of perfluoropolymer, Rep. Res. Lab. Asahi Glass Co. Ltd. 56 (2006) 35-38.

[22] B. Agnarsson, J. Halldorsson, N. Arnfinnsdottir, S. Ingthorsson, T. Gudjonsson, K. Leosson, Fabrication of planar polymer waveguides for evanescent-wave sensing in aqueous environments, Microelectr. Eng. 87 (2010) 56-61.

[23] C. Chiu, E. Lisicka-Skrzek, R. N. Tait, P. Berini, Fabrication of Surface Plasmon Waveguides and Devices in Cytop with Integrated Microfluidic Channels, J. Vac. Sci. Technol. B 28 (2010) 729-735.

[24] H. Asiri, “Fabrication of Surface Plasmon Biosensors in Cytop”, M.A.Sc. Thesis University of Ottawa (2012)

[25] A Khan, O. Krupin, E. Lisicka-Skrzek and P. Berini, “Mach-Zehnder refractometric sensor using long-range surface plasmon waveguides,” Appl. Phys. Lett. 103, 111108 (2013)

Chapter 3

Fabrication of a Plasmonic Modulator Incorporating an Overlaid Grating Coupler

3.1 Paper published in the journal Nanotechnology

My Contribution: The paper included in this chapter is published in the journal Nanotechnology and presents the complete fabrication of a plasmonic modulator with diffraction gratings. The design targets are 20 nm thick Au plasmonic surfaces, with 80 nm thick Au gratings, covered by a 700 nm thick PMMA layer. Electrical contact is established by placing 250 nm Au pads above the PMMA which contact the plasmonic surfaces layer through metalized VIAs opened through the PMMA. Device modeling and simulation was carried out by Chengkun Chen and Dr. Pierre Berini. The grating layer e-beam lithography procedure was developed and executed by Ewa Lisicka-Skzrek and Tony Olivieri. PMMA deposition and VIA perforation via e-beam were completed by Ewa Lisicka-Skrzek. All other fabrication steps were developed and performed by myself under the guidance of Dr. Tait and Dr. Berini. All tables were prepared by me, as were all figures with the exception the AFM, modulation, and SEM results. The latter two were prepared by Tony Olivieri.

Preamble: Fabrication for a completed novel plasmonic modulator concept is presented. The inclusion of diffraction gratings allows for plasmon excitation. Preliminary modulation results have been successfully observed and are included.

Fabrication of a Plasmonic Modulator Incorporating an Overlaid Grating Coupler

Sa'ad Hassan, Ewa Lisicka-Skrzek, Anthony Olivieri, R. Niall Tait, Pierre Berini

Abstract

The fabrication of a novel plasmonic reflection modulator is presented and described. The modulator includes plasmon excitation using a diffraction grating coupler and is based on a metal-insulator-semiconductor structure on silicon. Fabrication includes a thin thermal oxide, a plasmonic metal surface defined by optical lithography, a metal grating coupler defined by overlaid e-beam lithography, a passivation layer with metalized vias, and electrical contacts. Physical characterisation of intermediate structures is provided along with modulation measurements at λ_0 ~ 1550 nm which verify the concept.

I. Introduction

Plasmons are electron density oscillations which can occur in either the bulk or at the surface of a metal. Surface plasmon polaritons (SPPs) are coupled excitations comprised of electron density oscillations and a transverse-magnetic (TM) electromagnetic wave. SPPs propagate at the interface of a metal and dielectric at optical wavelengths, but are also supported on thin films with symmetric or asymmetric claddings [1]. On a thin asymmetric-cladded metal film, the non-radiative (bound) SPPs are localised on the high-index side and are strongly confined [1] -

such SPPs are of interest for compact device applications as in the modulators discussed in this paper.

The MOSFET which is vital to integrated electronic circuitry has scaled according to Moore's law. Inspired by this miniaturisation trend, optoelectronic devices are also scaling but not at the same rate, and comparably compact devices have yet to be achieved. Optoelectronic modulators on silicon, for instance, have advanced over the last decade but are still large compared to integrated electronics [2]. In order to bridge this gap and keep pace with current miniaturization trends, alternative approaches are required. Approaches based on SPPs are highly promising as very strong optical confinement is possible allowing dimensions to shrink, and the waves are highly surface sensitive allowing the exploitation of materials effects occurring near surfaces. These attributes can be exploited to achieve compact optoelectronic devices, such as modulators [3-10], which are usually constructed from an SPP waveguide configuration [3, 6-10], and photodetectors which are based on SPP waveguides or a variety of SPP scattering structures such as holes, particles, nano-antennas or gratings [11].

This paper reports on the fabrication of a novel grating-based plasmonic reflection modulator on silicon [12]. The structure is based on a metal-oxide-semiconductor (MOS) structure, and exploits the carrier refraction effect in Si. The device configuration allows intensity modulation of a perpendicularly-incident optical beam. The fabrication of plasmonic modulators is presented and described, including

details on all main fabrication steps. Measurements demonstrating the operation of the device are also presented.

II. Materials and Methods

A. Device structure and fabrication process flow

The modulator of interest is depicted in Fig. 1 and consists of seven fundamental parts. These parts are, in order of their fabrication: i) thin oxide, ii) backside Ohmic contact, iii) circular metal plasmonic surface, iv) metal grating, v) dielectric interlayer, vi) metallized vias, and vii) contact metal layer. The structure is to be fabricated on a double-side-polished p-doped (boron) Si wafer in the 100 orientation, of resistivity ρ = 0.08-0.095 Ω·cm (280 μm thick and 50.8 mm diameter). The thin SiO_2 layer should be 2 to 4 nm thick. The plasmonic surface should be about 20 nm thick, formed of Au, and deposited on a very thin Cr adhesion layer (< 1 nm). The grating pitch should be in the range of Λ = 420 to 480 nm, its duty cycle about 50%, and its thickness about H = 80 nm. The interlayer dielectric will be formed of PMMA (Poly(methyl methacrylate)) and should be about 700 nm thick. The vias of the same depth will be filled with contact layer metal, selected as Au, and of thickness 250 nm. The backside Ohmic contact is to be formed of 1000 nm thick Al. These material and dimensional specifications were determined following modelling and design work reported elsewhere [12] to produce a reflection modulator operating at λ_0 ~ 1550 nm. Alternatively, Cu could be used for the plasmonic surface and the grating, and other good dielectrics such as Si_3N_4 or HfO_2 could be used instead of SiO_2.

The Au plasmonic surface and grating, along with the thin oxide, silicon wafer, and backside aluminum act as a MOS capacitor. The application of a negative gate voltage drives the capacitor into accumulation and increases the density of mobile charge carriers at the semiconductor-oxide interface. The grating is designed to couple perpendicularly-incident *p*-polarised light to SPPs propagating along the Au-oxide-Si region. The accumulated charge carriers modify the local refractive index following the carrier refraction effect which then modifies the effective index of the SPP wave. This in turn alters the coupling efficiency of the grating to SPPs which modulates the reflected light**.**

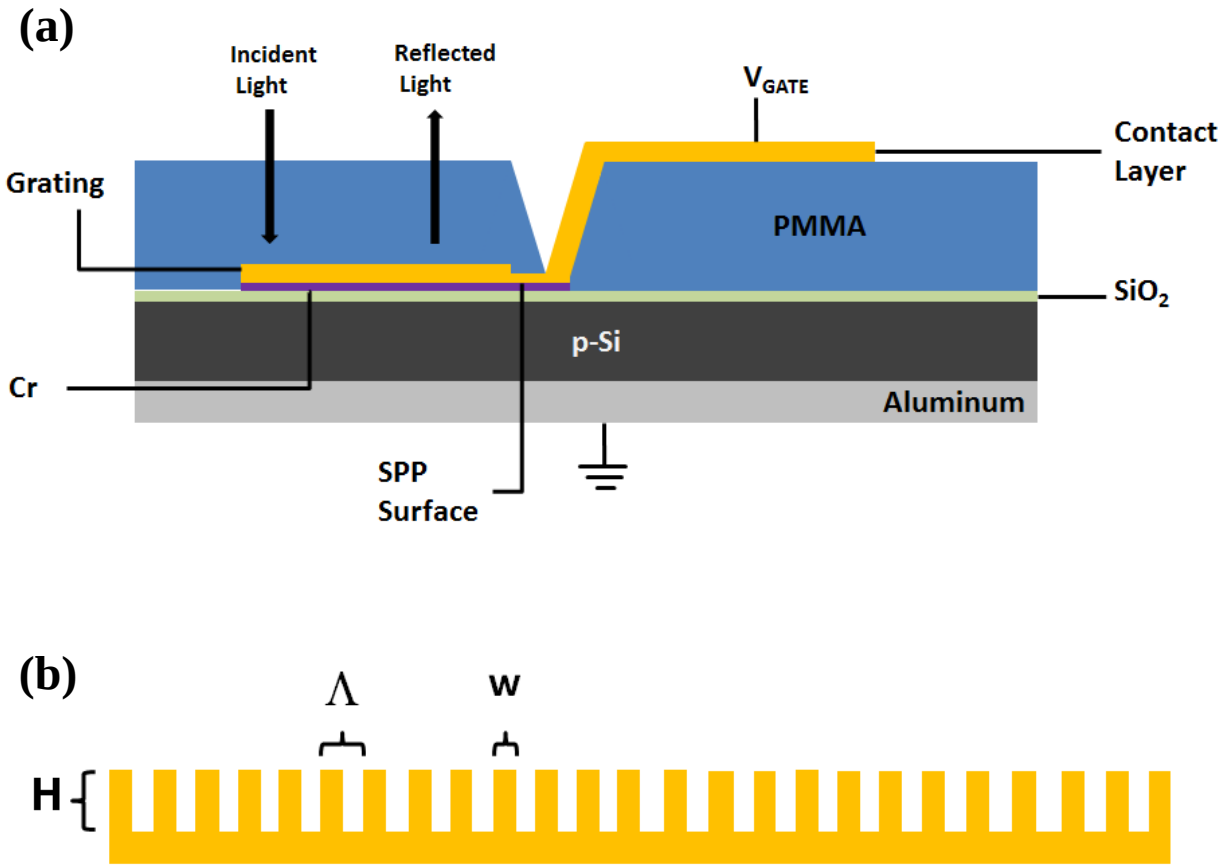

Figure 1. (a) Cross-section of the device. In this view, the grating ridges run along the width of the page. (b) Expanded rotated cross-section of the SPP surface with the grating ridges running into the page. H is the thickness of the grating, Λ is the period and w is the width of each grating ridge.

Figure 2 describes the flow of the main process steps developed and applied to fabricate the structures. Two optical lithography steps are required (plasmonic surface, contact metal) and two e-beam lithography steps are required (gratings, vias). Metal evaporation and lift-off is used. Details on these process steps are provided in what follows.

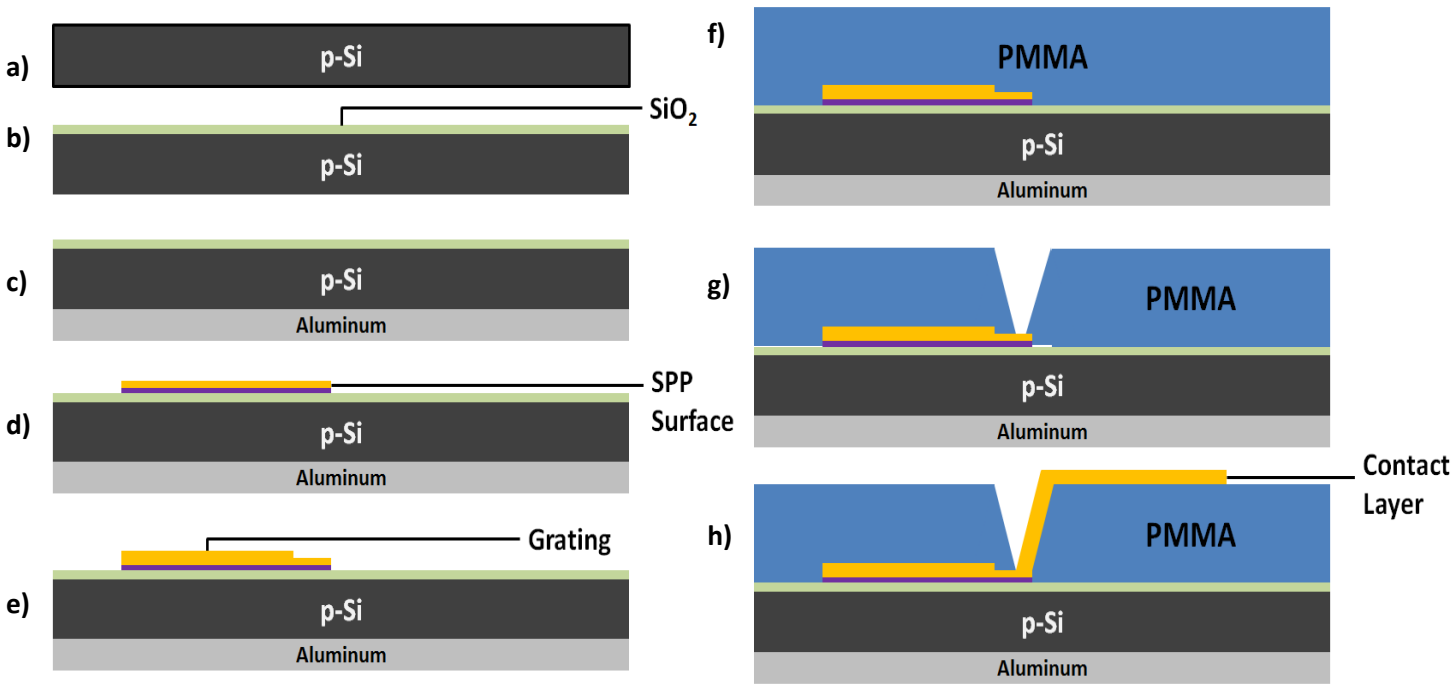

Figure 2. Fabrication process flow. (a) Preparation of silicon wafer, (b) growth of thin-oxide, (c) deposition of back-side metal, (d) deposition of plasmonic surface layer, (e) deposition of grating, (f) deposition of PMMA interlayer, (g) opening of vias, (h) deposition of contact layer metal.

B. Oxide, backside contact and plasmonic surface

Before the thin oxide is grown, the wafers are subjected to an RCA clean. The clean involves placing the wafer in three solutions, followed each time by a deionized water (DI) flush. The first solution consists of $NH_4OH/H_2O_2/H_2O$ in a ratio of 1:4:20. The second solution consists of $HCL/H_2O_2/H_2O$ in a ratio of 1:1:6. The final solution is 10% HF. These solutions clear the wafer of organic molecules, heavy metal ions and silica, respectively.

As mentioned in the previous subsection, the objective is to grow a 2 to 4 nm thick, dense, uniform, thermal SiO_2 layer. The Deal-Grove model which is often used to model the growth of oxides is inapplicable for a thickness less than 10 nm [13]. In the absence of a model, the procedure for growing a very thin SiO_2 layer on Si was arrived at through repeated experimental trials. The oxide is grown in a horizontal oxidation tube (Bruce 8-stack furnace BDF8); the final protocol is detailed in Table I. Note that any native oxide must be cleared immediately before loading into the furnace; the native oxide is etched by dipping the wafer in a 10% HF solution for 1 minute until the wafer's surfaces are hydrophobic. After the thin oxide is grown, oxidation continues once the silica surface is exposed to ambient air, therefore until the waveguide metal is deposited, all steps must be performed in rapid succession.

Table I. Procedure for the growth of a thin layer of SiO_2 on Si.

Step	Description	Details
1	Preheat of furnace	Set Furnace to 850 °C in N_2 3 L/min
2	Preheat at mouth	5 minute push of wafers to the mouth of the furnace
3	Push to centre/oxidation	3 minute push of wafers to the centre of the furnace Simultaneously, N_2 is switched off and 3 L/min O_2 is switched on
4	Anneal	20 minutes. Turn off O_2 and turn on 3 L/min N_2 flow
5	Pull to mouth	4 minute pull of wafers back to the mouth of the furnace
6	Cool at mouth	5 minute cool of wafers at mouth
7	Pull out	5 minute pull of wafers to exit of the Furnace

The deposition of the Ohmic contact is accomplished in an evaporation chamber (Balzers BA-510 evaporation chamber) using a rotating planetary system which

holds the wafers at an angle of approximately 45° to the source normal. The wafer is then rotated at a rate of 2 rpm during the evaporation, to ensure even film thickness across the wafer. Note that in the absence of lithography angular material deposition is not prohibited.

Prior to deposition, the oxide film on the backside of the wafer is etched by swabbing with a 10% HF solution. To ensure complete removal of the oxide, swabbing is repeated until the silicon becomes hydrophobic. Afterwards, the wafer is thoroughly flushed with DI water to remove any residual HF on the backside surface. Removal of the oxide is necessary to permit intimate contact between the metal and the semiconductor.

A 1000 nm layer of Aluminum is deposited at a rate of 1.5 nm/s as measured by a quartz crystal microbalance. To inhibit further front-side oxide growth, immediately after deposition, the wafers are placed in a high-temperature annealing chamber to sinter in H_2 the newly deposited Aluminum. The annealing procedure is listed in Table II.

Table II Procedure for the hydrogen sinter of the backside metal

Step	Description	Details
1	Preheat of Furnace	Set Furnace to 850 °C in N_2 3 L/min
2	Ignition	Turn off N_2 flow and replace with H_2 for 18 minutes. Ignite the gas.
3	Anneal	4 minutes, wafers held at the centre of the furnace
4	Post-purge	Shut off H_2 and reintroduce 3 L/min N_2 for 15 minutes
5	Pull Out	40s pull of wafers to exit of the furnace

6	Cool	15 minute cool of wafers in N_2

A thick (~ 400 nm) Au cap is sputtered on the backside once the sinter is complete, and the backside Ohmic contact has been properly annealed. This Au cap promotes good electrical contact and acts to chemically passivate the Al. Many of the processing steps to come, *e.g.* developments and lift-off, etch Aluminum and it is worthwhile to protect the backside.

The plasmonic surface consists of a circular Au patch designed to be one of 7 different diameters: 56, 28, 22, 17, 11, 5 and 3 μm. These diameters alter the device capacitance, which in turn affects their electrical bandwidth. Larger areas are easier to align to a focused incident optical beam than smaller areas. Smaller devices will have fewer grating ridges which ultimately results in a lower coupling efficiency but they also have lower capacitances and should operate over a larger electrical bandwidth. Optical proximity (contact) lithography was exploited to produce this layer. The lithography and lift-off procedures are described in Table III.

To avoid damage to the sensitive thin-oxide layer, thermal evaporation is used to deposit the Au plasmonic surface in order to avoid gamma ray and x-ray radiation that would be produced by e-beam deposition [14]. Additionally, Au adhesion to SiO_2 is poor, so an optically not-too-invasive adhesion layer is needed. To that end, a flash layer of Cr was deposited. The Cr coats a tungsten rod which is resistively heated allowing for a high degree of deposition control. Indeed, a deposition rate of 0.01 nm/s was achieved which was instrumental to the deposition of a uniform 0.3

nm layer of Cr. The flash Cr layer must be as thin as possible to remain optically non-invasive, while still acting as an effective adhesion layer. Once this deposition is completed, a shutter is swung into place blocking any further deposition, and allowing for a brief 10 min cooling period before the Au layer is evaporated. A Au ingot is placed in a tungsten carrier which is resistively heated allowing for a deposition rate of 0.02 nm/s. A Lower deposition rate reduces metal surface roughness and allows better thickness control.

Table III. Plasmonic surface photo-lithography procedure.

Step	Description	Details
1	Deposition of HMDS	Place in HMDS (Hexamethyldisilizane) oven at 97 °C
2	Deposition of LOR	Spin coat of Michrochem PMGi SFG 2S
3	Deposition of PR	Spin coat of Microposit S1805
4	Exposure	7 s exposure with Karl Suss MA 6 contact mask aligner
7	Development	Develop for 4 min 45s in Microposit MF-321 with aggressive agitation
8	Rinse	Flush rinse with de-ionized (DI) water
9	Metallization	Thermal deposition of 0.3 nm Cr followed by 20 nm Au
10	Lift-off	5 minute static dip in Microposit 1165 followed by 10 s ultrasonic. Repeat once. Static IPA and DI water baths for 10 min each. Finally, dry in N_2
11	Dehydration	Leave on hotplate at 95 °C for 15 min

Once metallization is complete, further oxide growth between the metal plasmonic surface and the semiconductor is minimized; it is no longer necessary to execute each step in succession without delay.

C. Grating lithography and metal deposition

Grating dimensions have already been detailed in Section A. The grating requires lithographic resolution finer than that possible by contact optical lithography therefore electron-beam nanolithography was used instead.

A poly(methyl methacrylate) (PMMA) bilayer is used as the e-beam resist, with metal evaporation and lift-off to produce the grating. The parameters of the bilayer stack, the e-beam exposure parameters (Raith Pioneer), and the post-exposure develop protocol were determined via experimental trials in order to produce a re-entrant resist profile of the desired dimensions. The complete protocol for the deposition of the PMMA bilayer, e-beam writes, metallization and lift-off are listed in Table IV. The overlay capabilities of the Raith Pioneer e-beam writer were exploited to align the gratings to the underlying Au plasmonic surfaces.

Table IV. Process flow for the gratings lithography, metallization and lift-off.

Step	Description	Details
1	Dehydration bake	Leave on hotplate at 195 °C for 1 hour
2	Deposition of HMDS film	Saturate for 20s then spin at 4000 rpm For 30 s
3	Deposition of first PMMA layer	Saturate wafer for 5 minutes with 6% PMMA 495k, spin at 4000 rpm for 45 s
4	Curing bake	Leave on hotplate at 195 °C for 1 hour
5	Deposition of second PMMA layer	Saturate wafer for 60 seconds with 2% PMMA 950k, spin at 2000 rpm for 45 s
6	Curing bake	Leave on hotplate for 180 °C for 1 hour
7	Pre-Exposure bake	Leave on hotplate at 195 °C for 1 hour
8	Exposure	E-beam power: 30 kV, Dosage: 300 $\mu C/cm^2$ with a 3-point alignment overlay process executed every 3 minutes, with auto axis correction

		and auto write-field alignment executed every 60 minutes
9	Post-Exposure Bake	Leave on hotplate at 95°C for 1 hour
10	Develop	Static bath 3:1 MIBK/IPA for 2 minutes at 20 °C followed by IPA bath, rinse in DI and N_2 dry
11	Descum[a]	14 s in reactive-ion etcher (RIE) at 100 W with O_2 flow of 100 sccm
12	Metallization	Thermal deposition of 80 nm Au
13	Lift-off	Static dip in 40 °C, stirred (500 rpm) acetone for 1 hour followed by 30 s ultrasonic at 86 kHz. Rinse with Acetone, then IPA

[a] – Note that descum time is dependent upon the sample size. The time listed is effective for a quarter of a 2 inch wafer.

D. Vias and contact layer

The thick PMMA interlayer necessary to separate the plasmonic surface from the contact layer along with a charge dissipation polymer (ESPACER™) [18]) are deposited as detailed in Table V.

Table V. Procedure for the deposition of the thick PMMA interlayer and opening of vias

Step	Description	Details
1	Dehydration Bake	Leave on hotplate at 180 °C for 2 hour
2	Deposition of HMDS Film	Saturate for 5 min then accelerate at 400 rpm/min to 4000 rpm, hold for 20 s and then decelerate at 400 rpm/min. Relax film for 30 s
3	Deposition of First PMMA Layer	Saturate wafer for 5 min with 2% PMMA 950k then accelerate at 200 rpm/min for 15 seconds to 1000 rpm. Accelerate again at 200 rpm/min for 35 s to 1600 rpm and

4		finally decelerate at 200 rpm for 10 s until stationary. Relax film for 10 min then bake at 180 °C for 1 hour.
	Deposition of Second PMMA Layer	Saturate wafer for 30 s with 7% PMMA 950k then accelerate at 200 rpm/s for 15 seconds to 1000 rpm. Accelerate again at 200 rpm/s for 35 s to 2000 rpm and finally decelerate at 200 rpm/s for 10 s
5		until stationary. Relax film for 10 min then bake at 180 °C for 1 hour
	Deposition of ESPACER	Saturate wafer for 60 s with ESPACER then accelerate at 300 rpm/s for 7 seconds to 1600 rpm then hold for 20 s. Finally, decelerate at 300 rpm/s for 7 s until stationary. Relax film for 30 s
6	Exposure	E-beam power: 10 kV, Aperture: 30 µm, Working distance: 7 mm, Write field: 100 µm, Step size: 0.0496 µm, Dosage: 68.5 $\mu C/cm^2$, Dosage factor: 1.25
7	Development	1:3 MIBK/IPA bath for 120 s followed by static IPA bath at 20 °C for 20 seconds. Finally, N_2 dry

Vias are then created by writing with e-beam through the PMMA layer, followed by a developing step. ESPACER was spun on the PMMA layer in order to limit charging during the e-beam writes. Vertical or sloped sidewalls are required for the vias in order to minimize the metal thickness needed for infilling while ensuring that the contact layer is electrically connected to the plasmonic surface. The e-beam parameters listed in Table V have been deduced to produce high-quality vertical sidewalls.

To preserve the PMMA stack through which the vias have been opened, a lithographic lift-off technique that negligibly etches PMMA was required. The lithography detailed in Table III uses N-methyl-pyrrolidone as the lift-off agent which

etches PMMA rapidly. This necessitated an alternative approach. Bodas *et al.* showed that tetra-methyl-ammonium-hydroxide (TMAH) etches PMMA at a rate less than 0.1 nm/min at room temperature [15]. Recall that the developer used in Table III is a 3% TMAH solution which enables us to use development as a slower lift-off process. To limit the lift-off process to a reasonable time (< 2 hrs) Megaposit MF-24A, a 12% TMAH solution, was used instead.

The lithography procedure for the contact layer is detailed in Table VI. After resist deposition, the wafer is exposed using a contact mask aligner, metallized using sputtering (Varian M2000 cluster tool), then e-beam evaporation, then undergoes lift-off. The metal sputtering step is required in order to conformally coat the inner surface of the via holes thus ensuring good contact between the metal contact layer and the plasmonic surface.

Table VI. Procedure for contact layer lithography, metallization and lift-off.

Step	Description	Details
1	PMMA Relaxation	Bake at 90 °C for 1 hour
2	Descum	4 s at 100 W in RIE with 100 sccm O_2
3	Deposition of HMDS Film	Place in HMDS oven at 97 °C
4	Deposition of LOR	Two stage spin coat of Michrochem LOR-10B, 10s at 1000 rpm followed by 30s at 3000 rpm
5	Soft Bake	Leave on hotplate at 190 °C for 6 minutes
6	Deposition of PR	Two stage spin coat of Shipley S1811, 10s at 1000 rpm followed by 30s at 4000 rpm
7	Soft Bake	Leave on hotplate at 105 °C for 3 minutes
8	Exposure	49 s exposure with Karl Suss MA 6 contact mask aligner
9	Development	Develop for 1 min in Microposit MF-321 with light agitation
10	Rinse	Flush rinse with de-ionized (DI) water

11	Metallization	Sputter 100 nm of Au followed by e-beam deposition of 250 nm of Au
12	Lift-off	1.5 hour static dip in MF-24A followed by gentle swabbing of the wafer's edge to initiate delamination. Static DI water bath for 10 minutes Finally, dry in N_2
13	Dehydration	Leave on hotplate at 95 °C for 1 hour

III. Results and discussion

A. Oxide characterisation

Upon exiting the oxidation furnace and immediately before deposition of the metal for the plasmonic surface (Subsection II B), the thickness of the grown oxide was determined by ellipsometry (Plasmos ellipsometer SD2000). Five-point measurements (centre, north, east, west and south) reveal the production of an oxide of average thickness 3.8 nm over several wafers. The oxide thickness has an average standard deviation of 2.1 nm.

The oxide must also be an effective electrical insulator, and this is tested by probing the thin plasmonic metal surface directly and measuring the dependence of capacitance on voltage (C-V) of the MOS structure. Capacitance measurements are taken from structures from each quadrant of a wafer. Representative capacitance curves are displayed in Figure 3.

The curve of Fig. 3(a) was obtained on a wafer identified internally as 2a3-a where the backside metal was not sintered and therefore likely formed a rectifying contact rather than an Ohmic one - the capacitance therefore includes that of the reverse-biased backside contact. The curve of Fig. 3(b) was obtained on a wafer identified internally as 2a2-b where the backside metallisation was sintered and therefore formed a good Ohmic contact - the capacitance is therefore that of the metal-oxide-semiconductor structure only. (Fig. 3(a) is included for the sake of completion because this wafer underwent further processing as discussed below.)

The oxide thickness can be calculated from the results of Fig. 3(b) via the following:

$$t = A\frac{\varepsilon}{C} \tag{1}$$

where *t* is the oxide thickness, *A* is the area of the metal surface contacted, ε is the permittivity of the oxide, and *C* is the measured capacitance in the strong accumulation region. Assuming that the relative permittivity of the grown oxide is 3.9, then an oxide thickness of 2.8 nm results; this is similar to ellipsometry measurements taken from this wafer (2a2-b) immediately after the oxide was grown, which yielded an average oxide thickness over the wafer of 2.5 nm.

The electric field in the oxide can be computed via:

$$E = \frac{V}{t} \tag{2}$$

where *E* is the electric field and *V* is the applied voltage. From the results of Fig. 3(b), we note that the oxide breaks down at -5.0 V, which, based on equation (2) implies a breakdown electric field of 1.75×10^{9} V/m. This breakdown field is slightly higher than the value for thermally grown bulk oxide of 1.40×10^{9} V/m [16], as expected for the case of a very thin oxide film [17]. Further, the leakage of the thin oxides is low and the conductance through the oxide, measured on features 56 μm in diameter, is of the order of 10^{-7} S.

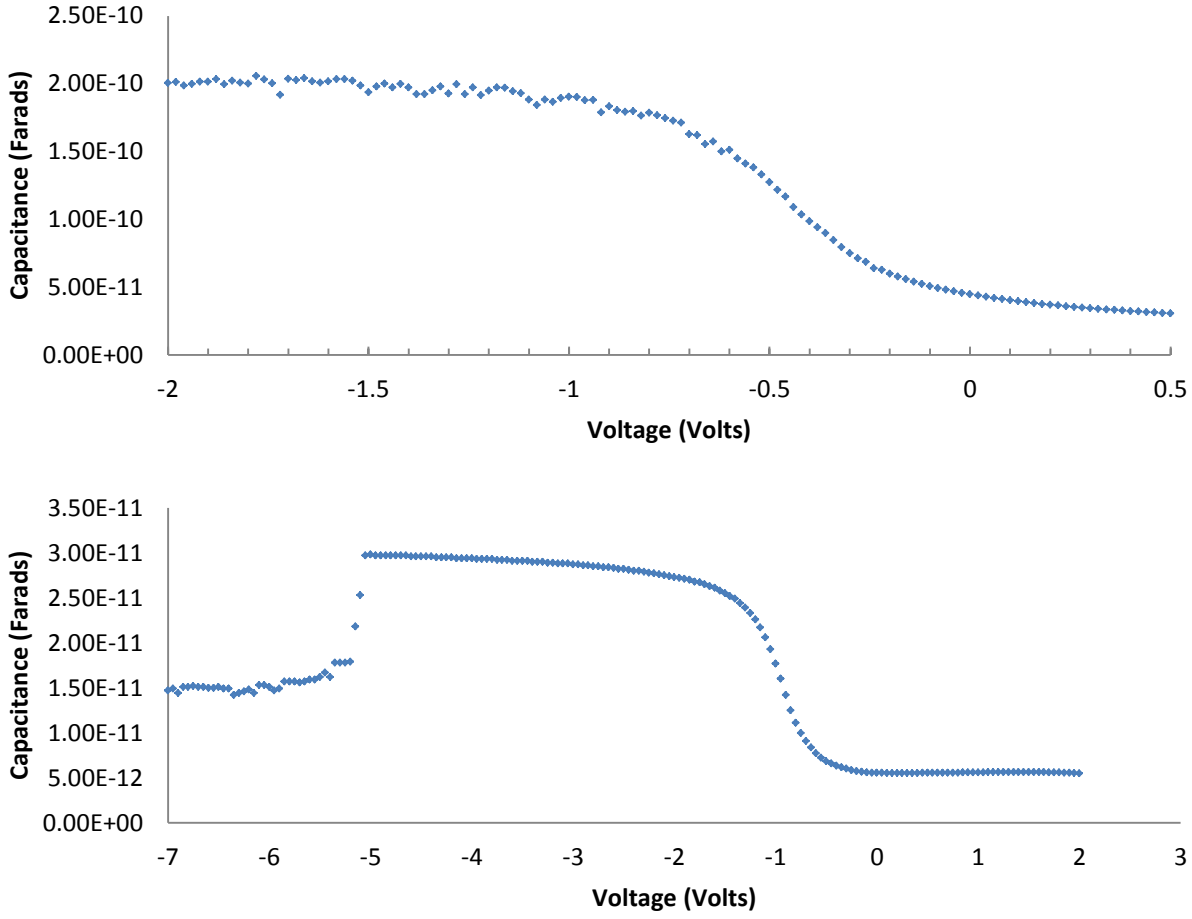

Figure 3. Capacitance versus voltage curves. a) The feature probed is 2,460 μm^2 in area (wafer 2a3-a). b) The feature probed is 2,460 μm^2 in area (wafer 2a2-b). Note the oxide breakdown at -5.0 V.

B. Plasmonic surfaces and overlaid gratings

The successful fabrication of the thin plasmonic metal surface following Sub-section II B, (Table III), is displayed as the microscope images of Figure 4. The layout consists of linear arrays of circular patches of varying diameter (56, 28, 22, 17, 11, 5 and 3 μm) each bounded by three “cross-hairs” to facilitate optical alignment of a perpendicularly incident beam during testing.

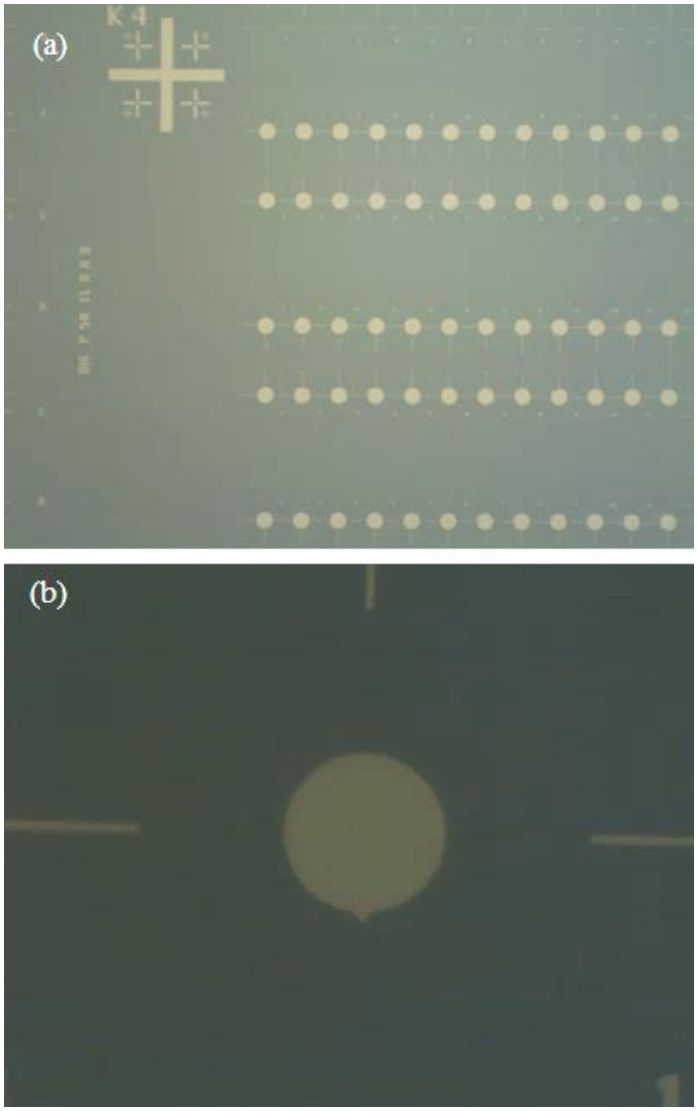

Figure 4. Microscope images of fabricated plasmonic surfaces on a wafer internally referenced as 2a3-a. (a) Large area showing an array of plasmonic surfaces; (b) a single plasmonic surface 28 μm in diameter.

Figure 5 shows a cross-sectional SEM image of a written and developed bilayer PMMA stack after grating metal deposition but prior to lift-off, fabricated following the process described in Sub-section II C (Table IV). The lower layer of PMMA, spun from lower molecular weight material, is damaged to a greater extent than the higher molecular weight PMMA which is spun on top, during e-beam writing. The differential damage creates a re-entrant profile after developing, which then allows the grating metal to be deposited with little or no side-wall deposition; a re-entrant profile is essential if clean lift-off is to be produced. The higher molecular weight PMMA top layer ensures dimensional accuracy of the metal features which then deposit into the trenches.

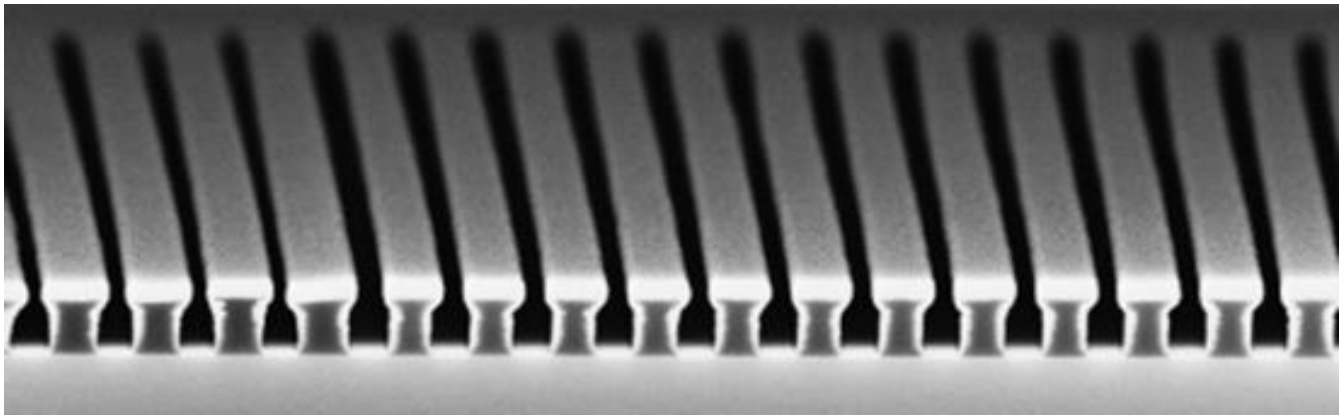

Figure 5. Cross-sectional SEM image of developed PMMA bilayer resist following grating metal deposition but before lift-off.

Figure 6 shows SEM images of gratings overlaid onto plasmonic surfaces, fabricated following Sub-section II C. Fig. 6(a) shows a perspective view of a grating overlaid onto a plasmonic surface which includes a contact arm and pad that can be used for electrical probing and testing of structures fabricated up to this stage. Fig.

6(b) shows a SEM image in top view of a grating overlaid onto a plasmonic surface consisting of a circular patch 28 μm in diameter. Fig. 6(c) shows the same grating in expanded view, revealing a pitch of Λ = 442 nm with a grating ridge width of 300 nm for a duty cycle of 68%. These dimensions are very close to those defined on the layout.

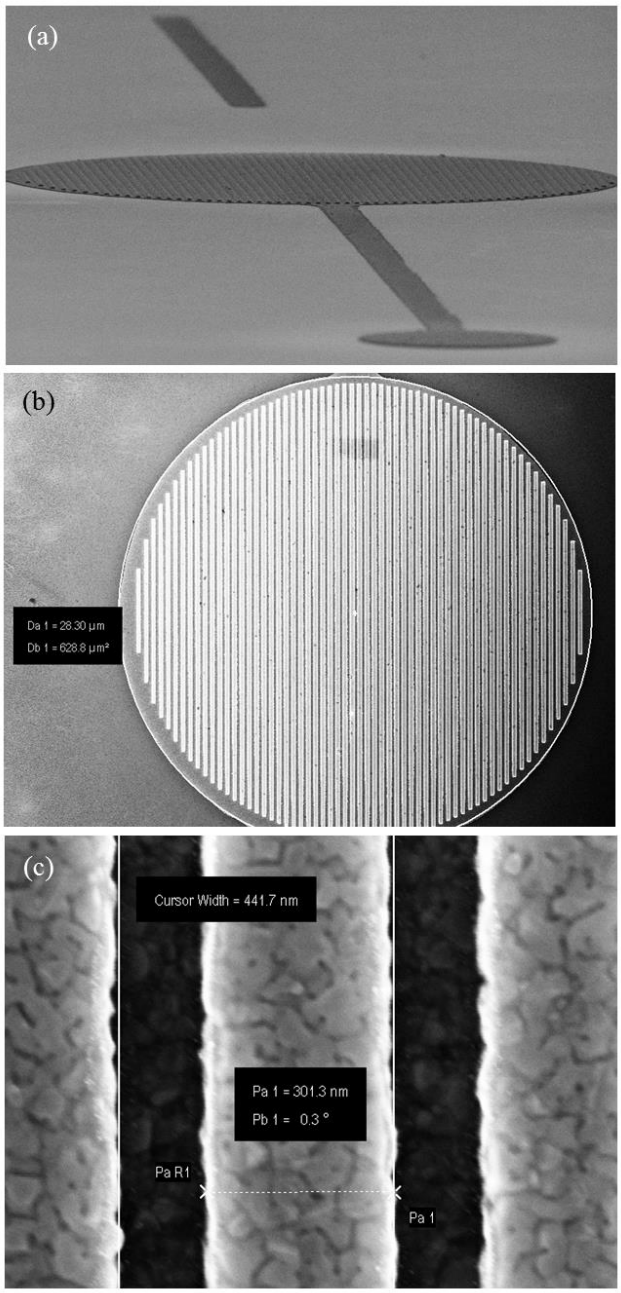

Figure 6. (a) Perspective view of a grating overlaid onto a plasmonic surface including a contact arm and pad for probing and preliminary testing (wafer 2a1-c). (b) SEM image in top view of a grating overlaid onto a plasmonic surface consisting of a circular patch 28 μm in diameter (wafer 2a3-a, device 11). (c) Magnified view of grating revealing a pitch of Λ = 442 nm and grating ridge width of 300 nm (wafer 2a3-a, device 11).

Figure 7 shows atomic force microscopy (AFM) scans from a device originating from wafer 2a3-a (similar to that shown in Fig. 6(b)) from which metal thickness and roughness have been deduced. Scans of the grating ridges, such as that shown as Fig. 7(a), indicate that they have a thickness of 88 to 89 nm with a root mean square (RMS) roughness of 1.5 to 2.3 nm along their top surface. The width and spacing of the ridges are 278 nm and 185 nm for a pitch of 463 nm and a duty cycle of 60%. From a scan of the edge of the plasmonic surface, such as that shown as Fig. 7(b), the thickness of the latter is found to be 26 nm with an RMS roughness of 1.3 nm. The RMS roughness of the neighboring oxide surface is 0.5 nm. Recalling the desired specifications for the structure (Sub-section II A), all dimensions are well in keeping with the target ones, except for the thickness of the plasmonic surface (26 nm *versus* the target thickness of 20 nm); this can easily be corrected by calibrating the quartz crystal microbalance in the evaporator. The low surface roughness on all metal surfaces (ridges and plasmonic surface), attest to the good quality of the thermally evaporated Au.

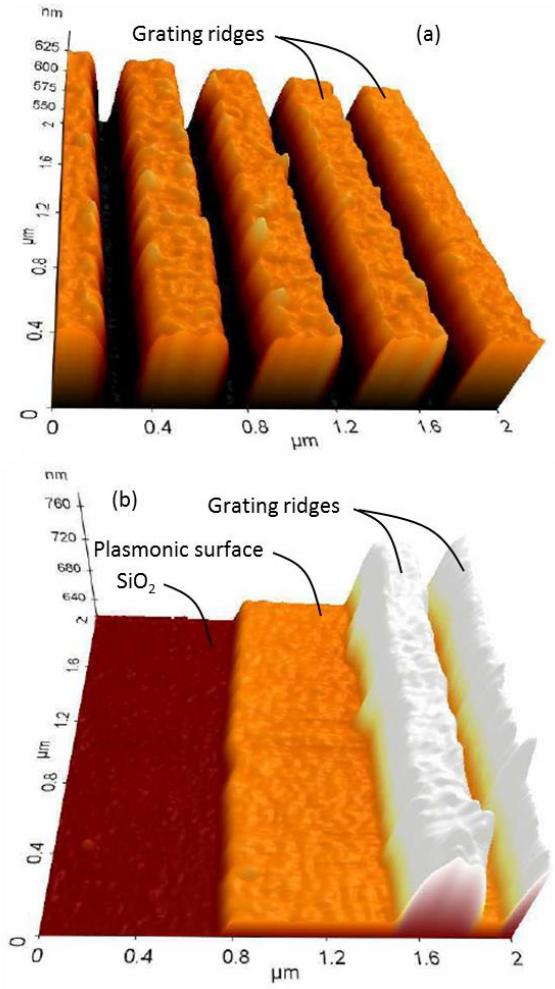

Figure 7. AFM images of a grating on a plasmonic surface (wafer 2a3-a, device 15). (a) Central region; (b) edge of the plasmonic surface with first two grating ridges.

It is possible at this stage of fabrication to test devices for their modulation ability as a means of verifying the process steps developed and carried out thus far. This is achieved by probing a plasmonic surface directly via a contact arm and pad introduced onto the layout for this purpose (*e.g.*, Fig. 6(a)). The device characterised is that shown in Figs. 6(b) and 6(c) (wafer 2a3-a, device 11). Fig. 8 shows the waveform measured at the output of a photoreceiver, while illuminating the

modulator with λ_0 = 1564 nm continuous-wave light, and driving it with a 45 MHz, 7.26 mV peak-to-peak modulating voltage at a bias of -2 V DC. This waveform drives the MOS structure in and out of accumulation (recall that fabrication was carried out on a p-type Si wafer). A clear modulation signal is observed at the operating wavelength (λ_0 = 1564 nm), and remained observable over ~ 20 nm of optical bandwidth.

The device tested did not have a sintered backside contact so only a fraction of the applied voltage appeared across the MOS modulator (the remainder appeared on the backside contact which was likely rectifying and reverse-biased - see Fig. 3(a)). A leakage current of about 5 mA DC was measured indicating that the thin SiO_2 film forming the MOS structure was not defect-free. The structure could be improved by sintering the backside contact to ensure that it is Ohmic, by ensuring that the plasmonic surface is closer to its design thickness, and by using a technique such as atomic layer deposition to form a thin oxide layer of better quality. Nonetheless, despite the fabrication imperfections, the modulation results demonstrate the device concept and validate many of the process steps developed.

The test set-up used to characterise the modulator employed a tunable laser diode with a series of collimating/focussing lenses to achieve a gaussian spot size that is less than the device area (~ 18 μm diameter), along with a beam splitting cube to separate the incident from the reflected beams, and a high-speed photoreceiver based on an avalanche photodiode.

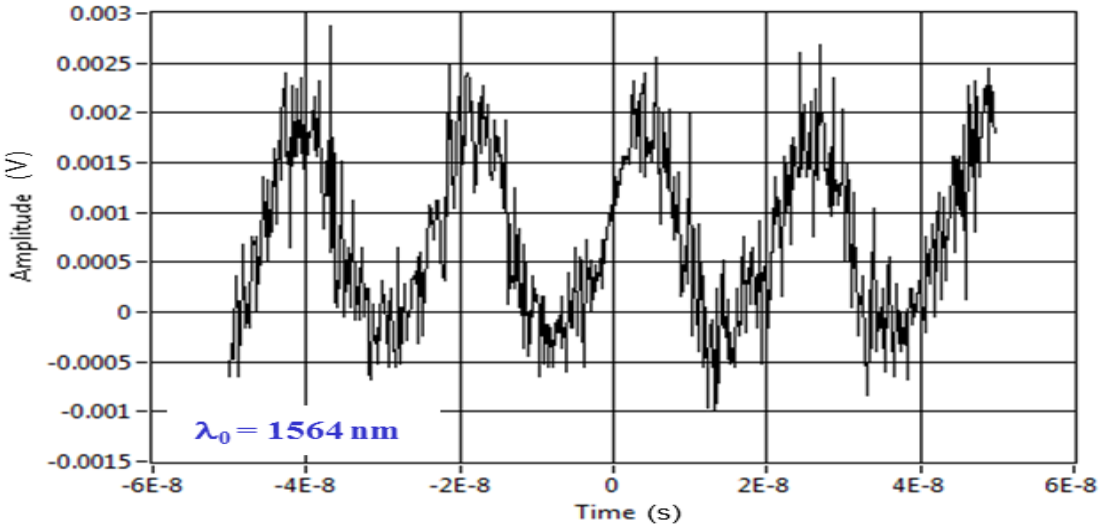

Figure 8. Modulation voltage at photoreceiver produced by a reflection intensity modulator, measured at λ_0 = 1564 nm (wafer 2a3-a, device 11).

C. Vias and contact layer

Figure 9 shows images summarising the results of the processes developed to create metallised vias fabricated following Sub-section II D Table V, and the contact layer metal fabricated following Sub-section II D, Table VI. Fig. 9(a) shows a SEM image in top view of a via hole metallised with 50 nm of sputtered Au, revealing a clean and smooth circular edge. Fig. 9(b) shows a SEM image in cross-sectional view through a cleaved metallised via, revealing a vertical sidewall and conformal coating of Au (50 nm sputtered). The thickness of the PMMA interlayer dielectric was measured as ~740 nm, close to target. Fig. 9(c) shows a microscope image of a full structure. The plasmonic metal surface (optical litho), the metal grating (e-beam litho), the metallised via (e-beam litho), and the contact layer metal (optical litho) were all successfully aligned and overlaid.

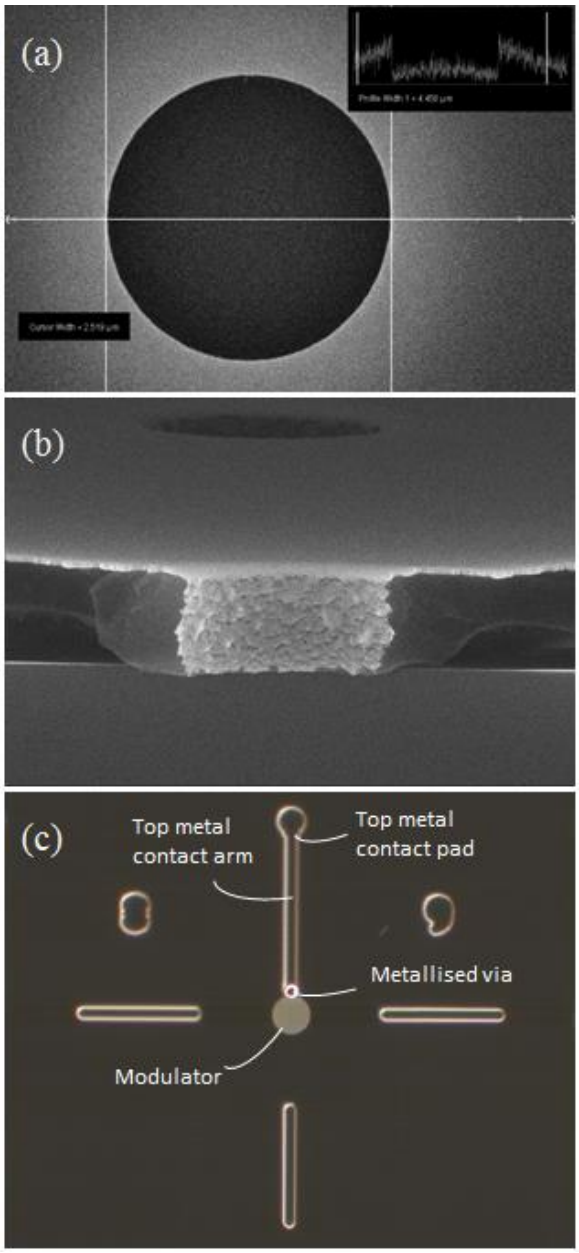

Figure 9. (a) SEM image in top view of a via hole metallised with 50 nm of sputtered Au; the diameter of the hole is ~2.5 μm. (b) SEM image in cross-sectional view through a via hole metallised with 50 nm of sputtered Au. (c) Dark field microscope image of a completed structure including a metalized via and the contact layer metal.

IV. Conclusions

Novel plasmonic modulators based on a metal grating coupler were fabricated. Complete fabrication details were provided and results given for intermediate structures. The device incorporated a MOS capacitor, with a thin-oxide, a grating, a passivation layer, a via and an electrical contact. A SiO_2 film ~3 nm thick was grown in a horizontal oxidation tube and its thickness verified by ellipsometry measurements. C-V measurements confirm the insulating quality of the film. Similarly, gratings of appropriate thickness and pitch were fabricated and their operation in a modulation experiment was demonstrated.

V. Acknowledgements

Financial support from the Natural Sciences and Engineering Research Council of Canada and from Test Photonics Canada is gratefully acknowledged.

References

[1] P. Berini, “Long-range surface plasmon polaritons*”, Advances in Optics and Photonics*, vol. 1, pp. 486, 2009

[2] J. A. Dionne, K. Diest, L. A. Sweatlock, H. A. Atwater, “A metal-oxide-Si field effect plasmonic modulator”, *Nano Letters*, vol. 9, no. 2, pp. 897, 2009

[3] A. Liu, R. Jones, L. Liao, D. Samara-Rubio, D. Rubin, O. Cohen, R. Nicolaescu, M. Paniccia, “A high speed silicon optical modulator based on a metal-oxide semiconductor capacitor”, *Nature*, vol. 427, pp. 615–618, 2004

[4] G. T. Reed, G. Mashanovich, F.Y. Gardes, D. J. Thomson, “Silicon optical modulators”, *Nature Photonics*, vol. 4, pp. 518-526, 2010

[5] J. N. Caspers, N. Rotenberg, H. M. Van Driel, “Ultrafast silicon-based active plasmonics at telecom wavelengths”, *Optics Express*, vol. 18, no. 19, pp. 19761-19769, 2010

[6] X. Sun, L. Zhou, X. Li, Z. Hong, J. Chen, “Design and analysis of a phase modulator based on a metal–polymer–silicon hybrid plasmonic waveguide”, *Applied Optics*, vol. 50, no. 20, pp. 3428-3434, 2011

[7] V. J. Sorger, N. D. Lanzillotti-Kimura, R-M. Ma, X. Zhang, “Ultra-compact silicon nanophotonic modulator with broadband response”, *Nanophotonics*, vol. 1, no.1, pp. 17-22, 2012

[8] A. V. Krasavin, A. V. Zayats, “Photonic signal processing on electronic scales: Electro-optical field-effect nanoplasmonic modulator”, *Physical Review Letters*, vol. 109, no. 5, pp. 1-5, 2012

[9] S. Zhu, G. Q. Lo, D. L. Kwong, “Phase modulation in horizontal metal-insulator-silicon-insulator-metal plasmonic waveguides”, *Optics Express*, vol. 21, no. 7, pp. 8320-8330, 2013

[10] A. Melikyan, L. Alloatti, A. Muslija, D. Hillerkuss, P.C. Schindler, J. Li, R. Palmer, D. Korn, S. Muehlbrandt, D. Van Thourhout, B. Chen, R. Dinu, M. Sommer, C. Koos, M. Kohl, W. Freude, J. Leuthold, “High-speed plasmonic phase modulators”, *Nature Photonics*, vol. 8, pp. 229-233, 2014

[11] P. Berini, “Surface plasmon photodetectors and their applications,” *Laser and Photonics Reviews*, Vol. 8, pp.197-220, 2014

[12] P. Berini and C. Chen, “Metal-insulator-semiconductor modulator and detector based on surface plasmon polaritons,” US provisional patent, filed 2013

[13] E. P. Gusev, H. C. Lu, T. Gustaffson, E. Garfunkel, “Growth mechanism of thin silicon oxide films on Si(100) studied by medium-energy ion scattering”, *Physical Review B*, vol. 52, no. 3, pp. 1759, 1995

[14] K. S. Sree Harsha, “Principles of vapor deposition of thin films”, Elsevier, pp. 403-404, 2006

[15] D. S. Bodas, S. A. Gangal, “Poly(methyl methacrylate) as masking material for microelectromechanical system (MEMS) fabrication”, *Journal of Applied Polymer Science*, vol. 102, pp. 2096, 2006

[16] J. F. Verweij, J. H. Klootwijk, “Dielectric breakdown I: A review of oxide breakdown”, *Microelectronics Journal*, vol. 27, pp. 613, 1996

[17] S. M. Sze, “Physics of Semiconductor Devices,” 2nd Ed., Wiley, 1981

[18] ESPACER™, Showa Denko Singapore, www.sds.com.sg

Chapter 4

Atomically Flat Symmetric Elliptical Nanohole Arrays in a Gold Film for Ultrasensitive Refractive Index Sensing

4.1 Paper published in the journal Lab on a Chip

My Contribution: The paper included in this chapter was published in the journal Lab on a Chip and presents the modelling, fabrication and characterisation of elliptical nanohole arrays. The design parameters optimized by FDTD calculations are elliptical nanoholes in a 100 nm thick Au film, 175 nm and 80 nm for the major and minor axes of the ellipses, respectively, and a nanohole period of 495 nm. The ultra-smooth (atomically flat) Au film is produced by template stripping and is supported by a stack of Optical Epoxy (MG Chemicals 8321C) or Cytop. Nanoholes are opened in the Au film by focused ion beam (FIB). Device modeling and simulation was carried out by Gabriela Andrea Cervantes Tellez under the guidance of Dr. Gordon. The FIB opening of the nanoholes, template stripping and all optical measurements were performed by Gabriela Andrea Cervantes Tellez. All other fabrication steps, including Cytop cladding formation and Au deposition on an oxidised Si wafer were completed by me under the guidance of Dr. Tait and Berini.

Preamble: Fabrication of a completed array of elliptical nanoholes in an Au film is presented. The use of Cytop allows for refractive index symmetry with fluidics, and template stripping produces atomically smooth Au films. Resolution comparable to commercially available Kretschmann SPR sensors is observed

Atomically Flat Symmetric Elliptical Nanohole Arrays in a Gold Film for Ultrasensitive Refractive Index Sensing

Gabriela Andrea Cervantes Tellez, Sa'ad Hassan, R. Niall Tait, Pierre Berini, and Reuven Gordon

Past works on refractive index sensing using nanohole arrays in metal films typically achieved a resolution of around 10^{-4} to 10^{-5} refractive index units (RIU), up to 10^{-6} with complicated detection setups. This is an order of magnitude worse than commercial Kretschmann-based surface-plasmon resonance (SPR) sensors. Here, we demonstrate intensity-based bulk refractive index sensing in an aqueous environment with a resolution of 9.38×10^{-8} refractive index units (RIU), showing for the first time comparative performance for nanohole SPR with Krestschmann-based SPR. This is achieved by the combination of three advances in the materials properties: a) template stripping to achieve ultra-flat Au surfaces of ~0.2 nm roughess, b) elliptical nanoholes to enhance transmission, and c) a Cytop substrate to symmetrize the refractive index with the aqueous environment above the metal film. The simple optical microscope geometry and microfluidic integration used in this work is promising for multiplexed lab-on-chip analysis.

Introduction

Surface plasmon resonance (SPR) has been used as a technology for monitoring refractive index changes due to mass loading at the surface of a metal film. SPR sensing has been used in applications including food safety, medical diagnosis, and drug development [1-4]. Biosensors based on SP effects are dominated by the use of the Krestschmann geometry [5]. Commercial SPR sensors based on the Kretschmann geometry achieve a resolution of 10^{-7} refractive index units (RIU) [6].

In 1998, Ebbesen discovered extraordinary optical transmission through periodic nanohole arrays in a metal film [7]. Since that time, it has been shown that the nanohole array transmission spectrum can be sensitively influenced by the refractive index of the adjacent medium, the shape of the apertures, aperture diameter, periodicity, and film thickness [8-13]. Compared to the Kretschmann geometry, using nanohole arrays is extremely promising for future sensor technologies because it allows a small footprint for dense integration, a high degree of multiplexing, collinear optical detection, and the ability to integrate microfluidics [14-33]. The main performance characteristics of SPR sensors include sensitivity, resolution, accuracy, and linearity. So far, the resolution of nanohole arrays has been demonstrated to be between 10^{-4}-10^{-6} RIU. A sensitivity of 10^{-5} RIU was achieved by using crossed polarizers that were able to select between the coherent and incoherent contributions of extraordinary optical transmission [34]. That work also predicted 10^{-6} RIU resolution with further improvements to the setup. The resolution was improved to 1.69×10^{-6} RIU by using a signal of two orthogonal

polarizations impinging on a nanohole array with rectangular periodicities [35]. Dual-wavelength LEDs have also been used to increase spectral diversity with 6×10^{-4} RIU resolution [36].

In this work, we demonstrate intensity-based bulk refractive index sensing in an aqueous environment with a resolution of 0.98×10^{-7} RIU and an intensity sensitivity of 1.67×10^{5} % per RIU. Bulk sensing performance is not necessarily indicative of binding sensor performance, which will depend on the local electromagnetic field distribution [37].

Here we demonstrate for the first time comparative bulk sensing performance for nanohole SPR with Krestschmann-based SPR. This is achieved by optimization of the material properties: template stripping to achieve ultra-flat surfaces of ~0.2 nm in roughness, elliptical nanoholes to enhance the transmission and a Cytop substrate to symmetrize the refractive index with the aqueous environment. These results are encouraging for future detection of chemical and biological species.

Results and discussion

Design and optimization of the elliptical nanohole arrays

We performed comprehensive calculations of the transmission spectra of the elliptical nanohole arrays using the finite difference time domain method (FDTD) to have an idea of the optimal parameters: periodicity of the holes, film thickness and dimensions of minor and major axes of the elliptical holes. Elliptical nanoholes are known to have higher transmission that is strongly polarized and can produce

sharper peaks [10], therefore, they are expected to give improved sensor performance (considering Eq. 1 below). FDTD optimization targeted the sensor performance; considering the impact of the spectral change on the resolution. With suitable design, shot noise can be made to be the dominant noise contributor and it scales as the square root of the intensity. The resolution, then, when changing the refractive index from $n_1 = 1.3375$ to $n_2 = 1.3377$ will be proportional to

$$R = \left| \frac{I_{n1} - I_{n2}}{\sqrt{\frac{I_{n1} + I_{n2}}{2}}} \right| \quad (1)$$

where I_{n1} and I_{n2} represent the transmission intensities for different refractive index values. We performed FDTD calculations for periodicities from 470 to 500 nm, and dimensions for the minor axis from 50 to 100 nm and for the major axis from 140 to 200 nm. To model the dispersive Au film a fit to experimental values was used [38]. The substrate was taken to have a refractive index of 1.52 (for glass), and Cytop (an amorphous perfluoro polymer) was taken to have a refractive index of 1.34 [39].The simulation domain used perfectly matched layer boundary conditions above and below the structure to prevent reflections and Bloch boundary conditions laterally to define the periodicity of the structure. A plane wave source was normally incident on the elliptical nanohole array. A frequency domain profile monitor collected the transmission through the elliptical nanoholes in the visible and near infrared wavelength range. A mesh over-ride of 2 nm was used throughout the Au film, a dimension small enough to capture the SP dispersion as confirmed via finite

difference mode calculations. The sensitivity was determined by noting the change in the transmission characteristics for varying refractive index of the solution bounding the elliptical holes.

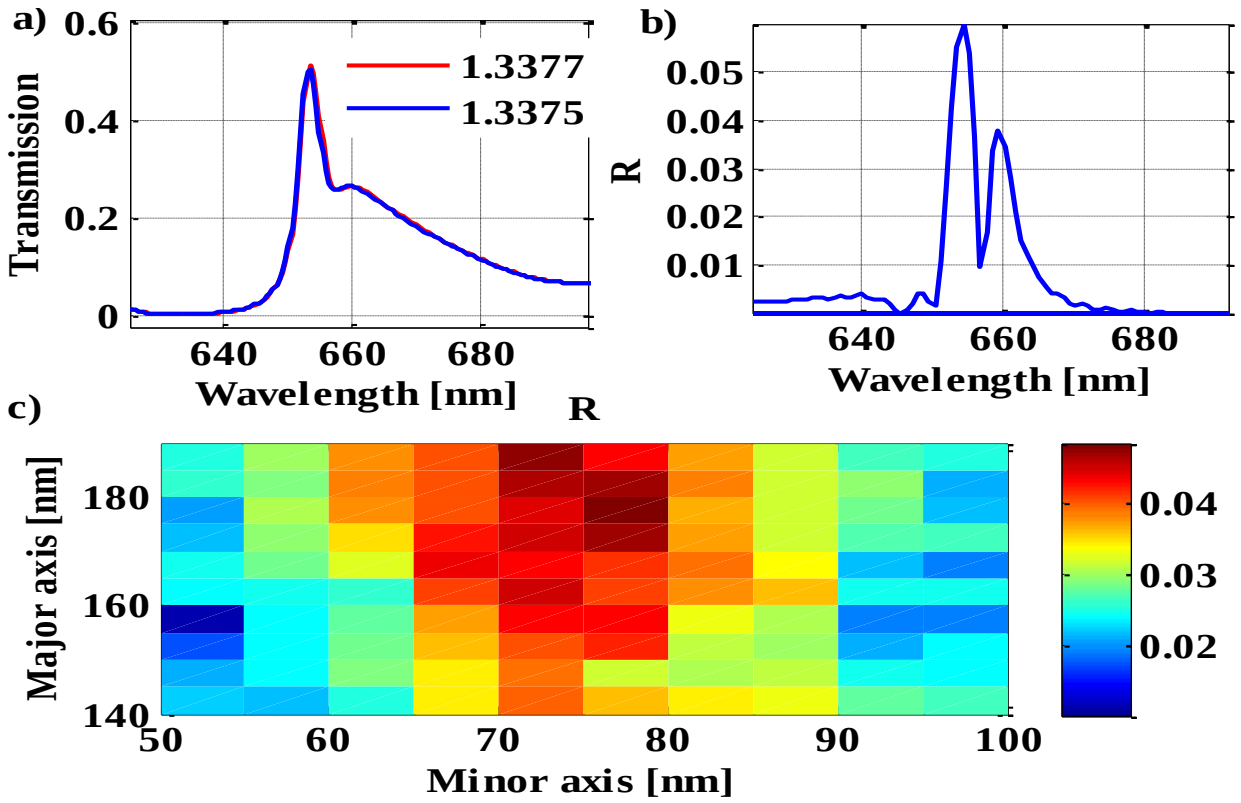

Figure 1. Results of FDTD simulations. (a) Transmittance spectrum of the optimized elliptical nanohole array with a major axis of 175 nm, a minor axis of 80 nm and a periodicity of 495 nm. (b) Optimal wavelength of operation for the optimized elliptical nanohole array (655 nm). (c) Optimization of the parameter *R* for elliptical nanohole arrays with a periodicity of 495 nm, and minor axis ranging from 50 to 100 nm and major axis from 140 to 200 nm (Eq.(1)).

Fig. 1 (a) shows the best result among all calculations, consisting of the transmittance for an optimized elliptical nanohole array with dimensions of 175 nm for the major axis, 80 nm for the minor axis, a 495 nm periodicity, and using a 100 nm thick Au film with Cytop as the substrate. This design gives $R = 0.055$ (Eq. (1)).

By comparison a circular hole array on glass produced $R =$ 0.016 for a periodicity of 425 nm and a hole diameter of 150 nm.

Fig. 1 (b) shows that the optimal wavelength for operation for this elliptical nanohole array is at 655 nm. Fig. 1 (c) shows the FDTD optimization for the elliptical nanohole array parameters. Here the dimensions of the minor axis were varied from 50 to 100 nm and the dimensions of the major axis were varied from 140 to 200 nm for a periodicity of 495 nm.

Characterization of the elliptical nanohole arrays

Fig. 2 (a) shows the experimental setup to measure the transmission spectra where the light from a halogen lamp was focused by a 0.5 NA microscope objective. A fiber optic was used to collect the light connected to an Ocean Optics USB-2000 miniature spectrometer. Visible and near infrared spectra were recorded with an acquisition time of 200 ms. Fig. 2 (b) shows the transmission spectra of an elliptical nanohole array with a major axis of 175 nm, a minor axis of 80 nm and a periodicity of 495 nm on the template-stripped Au film with Cytop. Good agreement is seen between Fig. 2 (b) and the FDTD calculations of Fig. 1 (a).

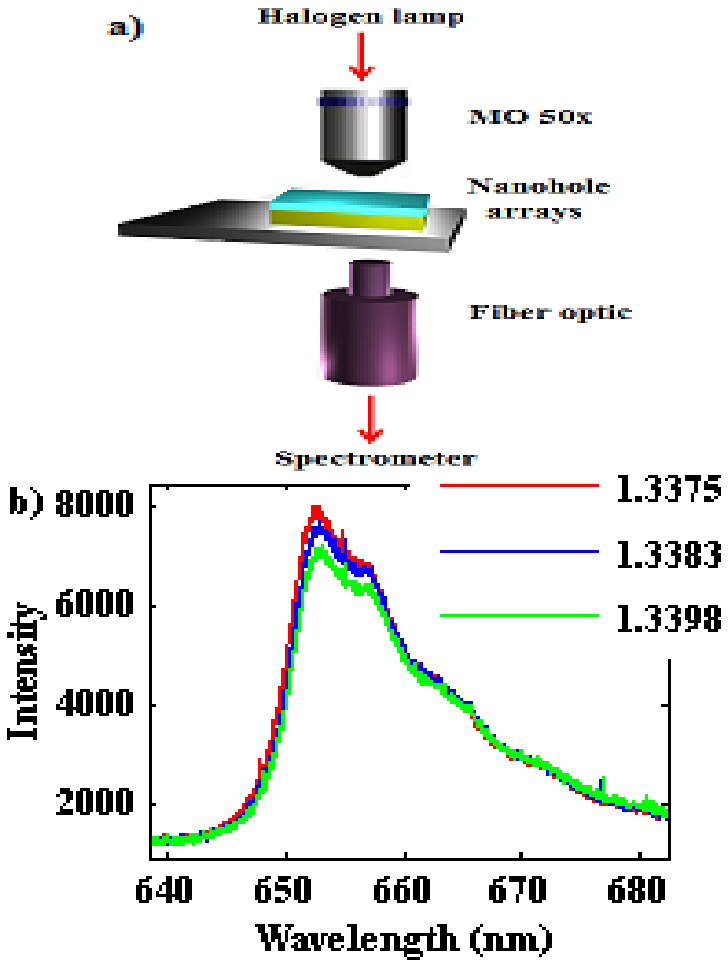

Figure 2. Measurements of the optimized elliptical nanohole array. (a) Experimental setup to record the transmission spectrum of the fabricated elliptical nanohole arrays. (b) Transmission spectra of normally incident white light through an elliptical nanohole array with a major axis of 175 nm, a minor axis of 80 nm and periodicity of 495 nm on the template-stripped Au film with Cytop. The three curves correspond to three solutions of different refractive index adjacent to the Au surface and filling the holes of the array.

Experimental set-up

Fig. 3 shows the experimental setup for measuring the samples subjected to refractive index steps of the solution. It is based on the microscope transmission geometry. A laser diode at 655 nm wavelength in constant power mode was used, to

reduce noise. The laser beam was focused using a microscope objective of 0.1 numerical aperture (NA) that ensured a low angular deviation of the incident photons and thereby sharpening the transmission resonance [40]. For the elliptical holes the laser beam was polarized perpendicular to the major axis of the ellipse. Then, the emerging light was collected with a microscope objective of 0.5 NA that acquired a larger number of photons to increase the signal to noise ratio, which is shot noise dominated. The sizes of the fabricated elliptical nanohole arrays as well as the illumination spot of the laser beam are factors that help to reduce also the shot noise in the system [41]. A CCD camera (Prosilica GC) was used to image the output of the nanohole arrays while flowing solutions of slightly different refractive index over the sample. This camera was chosen because it has a high frame rate and sensitivity, thereby maximizing the photons collected. The high frame rate is important to avoid saturation prior to read-out when using higher laser intensities. Any change in the refractive index of the solution appears as a change in the intensity of transmission through the aperture arrays. A polydimethylsiloxane (PDMS) based microfluidic flow-channel was created over the chip by replica molding from a photolithographic mask in SU-8. The fabricated samples were sandwiched between two acrylic layers to seal the flow channel. A syringe pump (Harvard apparatus 11 series) was used to produce a stable liquid flow rate of 7µL/min.

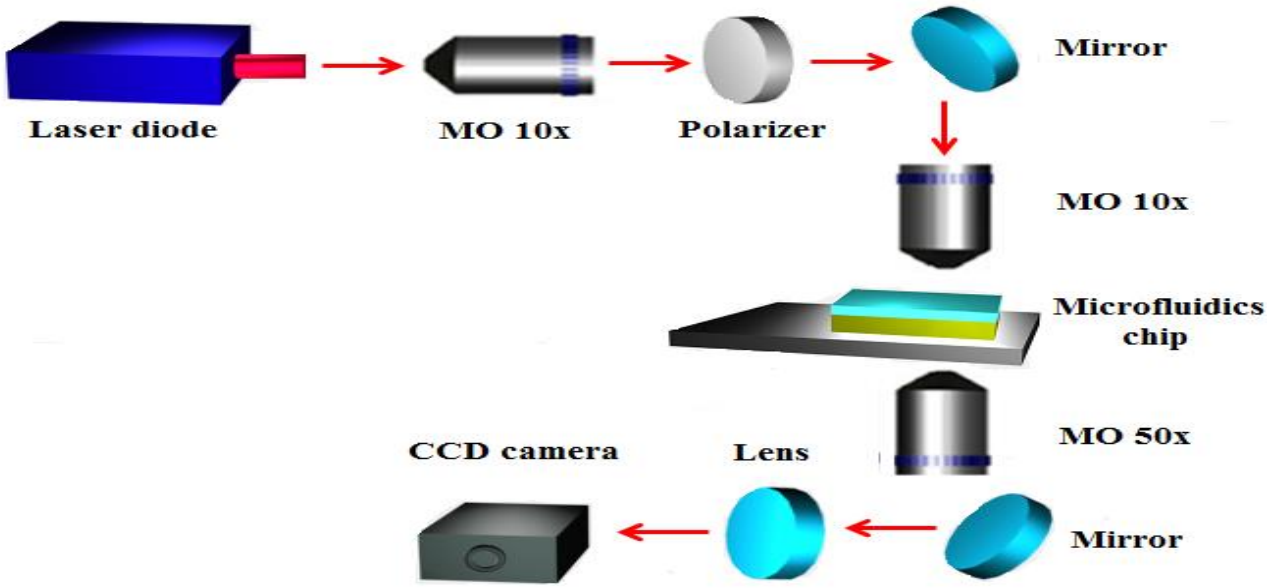

Figure 3. Schematic of optical setup for measuring the change in intensity of the fabricated samples.

Bulk sensitivity measurements for atomically flat Au films

Measurements carried out with a high intensity laser diode source and the data was filtered numerically to remove noise outside of the operating bandwidth. The numerical filtering reduced the time resolution to 0.5 frames per second. Fig. 4 shows the intensity change of the optimized elliptical nanohole array subject to different refractive solutions. Resolution was defined as the difference between refractive indexes divided by the signal to noise ratio (SNR). The SNR was determined by taking the difference between the mean value of the signal for the bottom and top part of each step, divided by the standard deviation of the signal at those levels.

The best experimental result obtained among all the arrays was an optimized elliptical nanohole array (major axis of 175 nm, minor axis of 80 nm and periodicity of 495 nm) on the template-stripped Au film with Cytop substrate, yielding a resolution of 9.38×10^{-8} RIU. This is a promising value, comparable with existing commercial SPR devices, while allowing for multiplexing, integration and optofluidic provided by using nanohole arrays as the sensors. The Au template-stripped approach for the same nanohole array parameters but without the Cytop layer had a resolution of 3.6×10^{-7} RIU. For the Au on Cytop without template stripping, the resolution was 2.8×10^{-7} RIU. The best resolution obtained for elliptical nanoholes milled in a commercial gold-on-glass slide was 6.8×10^{-7} RIU.

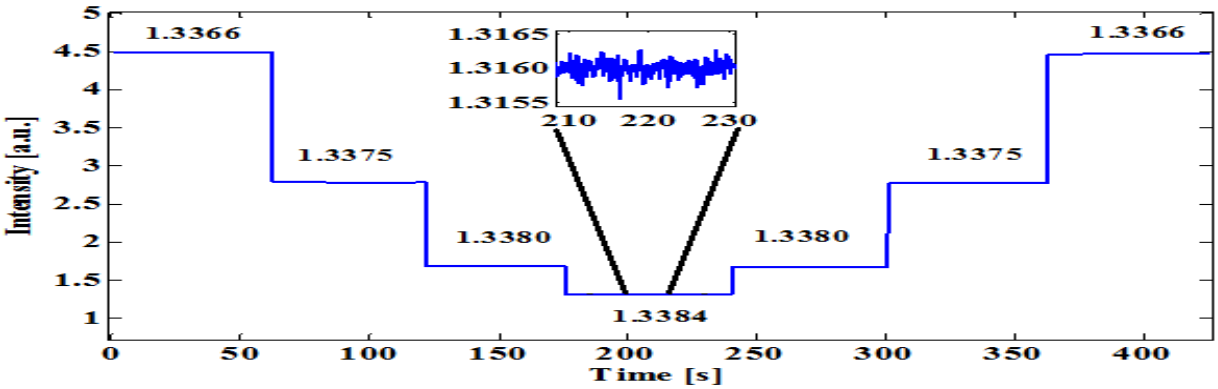

Figure 4. Experimental results for measuring the change in intensity at a wavelength of 655 nm of an elliptical nanohole array with a periodicity of 495 nm, a minor axis of 80 nm and a major axis of 175 nm on the template-stripped Au film with Cytop.

We performed bulk measurements for many other elliptical nanohole arrays with dimensions close to the optimal value found from calculations; however, these all yielded lower resolution results. For example, for the array with a periodicity of

490 nm, a minor axis of 65 nm and a major axis of 160 nm, the resolution was found to be 5.69×10^{-7} RIU.

As mentioned in the introduction, bulk sensing performance is not necessarily indicative of binding sensor performance [37]. There is, however, a relation between bulk and surface sensitivity that can be readily defined if the electromagnetic field distribution is known [42]. The surface sensitivity is expected to be directly proportional to the bulk sensitivity for sensing modalities that use the same surface plasmon mode (i.e., the same field distribution). In this case, the SPP of a single interface is expected to play an important role in EOT phenomenon [8]. The surface sensitivity should be comparable to that of the Kretschmann geometry in conventional SPR that also uses the single interface SPP and achieves 10^{-7} RIU bulk resolution.

Materials and methods

Template stripping

Even nanometric roughness can dampen the propagation of SPs [43]. The template stripping procedure was introduced as an alternative to produce smooth Au surfaces with decreased SP propagation loss [44-47]. Here, the template stripping procedure begins with the e-beam evaporation of 100 nm of Au on a Si wafer. The deposition rate used was 0.1 nm/s. The Au film is subsequently coated with optical epoxy (MG Chemicals 8321C) and covered with a glass slide. The optical epoxy acts as an adhesion layer to attach the Au film to the glass slide. After baking at 80°C for 150

min, the optical epoxy adhered to the glass slide and the Au. We then peeled off the Au on epoxy on the glass slide from the Si wafer revealing the Au surface.

Figures 5 (a) and (b) show atomic force microscopy (AFM) measurements for two Au surfaces, revealing that the film formed by template stripping retains the smoothness of the crystalline Si (Fig. 5 (b)) and is much smoother than a reference Au film obtained from a commercial supplier (Fig. 5 (a)). The area scanned for the AFM measurements was 3×3 μm^2. The root-mean squared (RMS) surface roughness was 1.3 nm for the commercial sample, and 0.05 nm for the template stripped sample on Si.

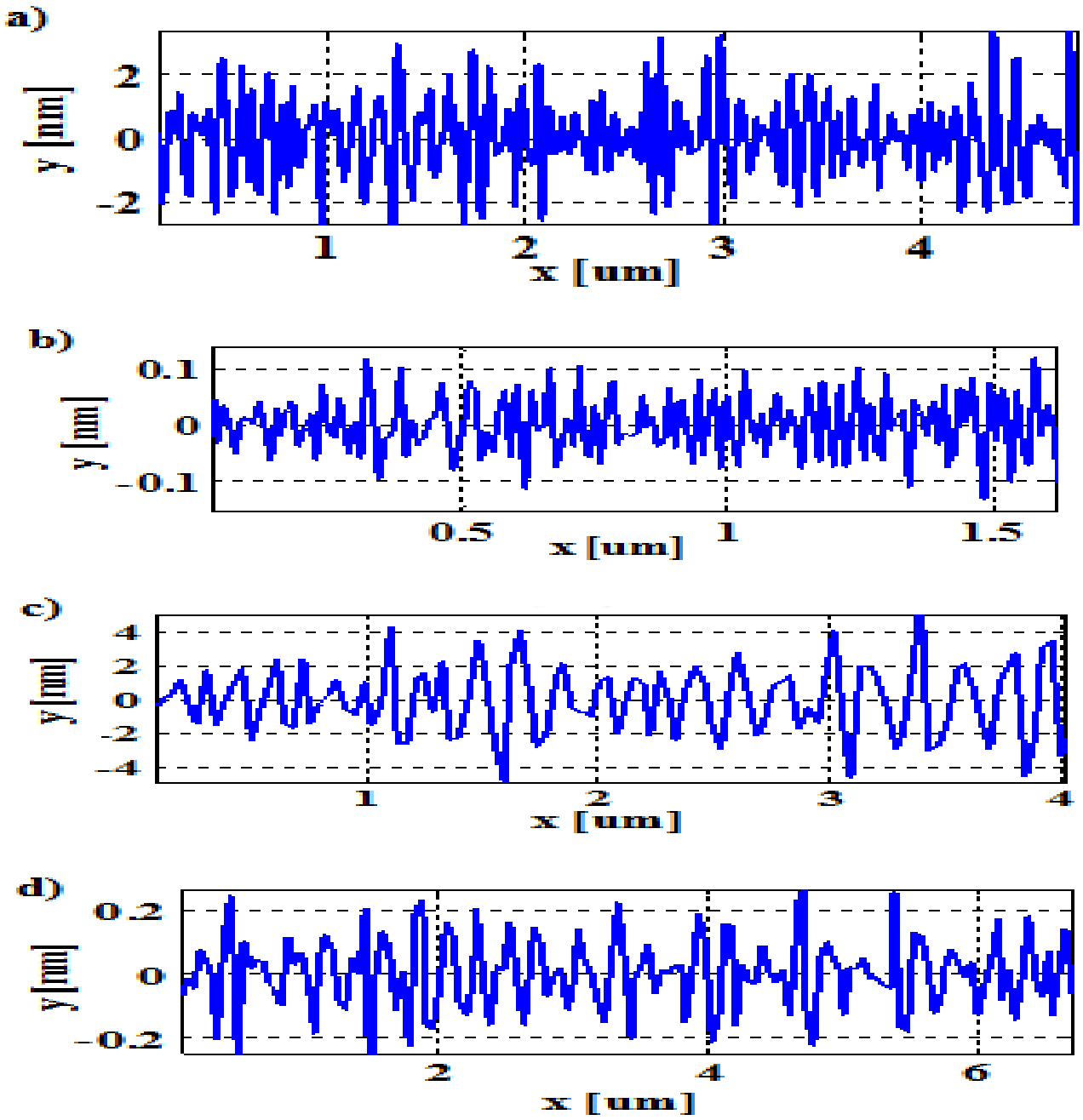

Figure 5. Results of AFM studies. (a) Surface roughness of a commercial Au sample. (b) Surface roughness of an Au film formed by template stripping. (c) Surface roughness of a Au film on Cytop. (d) Surface roughness of an Au film covered by Cytop and formed by template stripping. The order of magnitude difference in scales on the y-axis should be noted.

Au film and Cytop

Cytop was chosen as the lower cladding material because it has an index of refraction close to that of water which increases the transmission resonance quality [6]. Furthermore, it has excellent transparency [39]. The fabrication process essentially follows Ref. 48. It consists of starting with a microscope slide (VWR VistaVision) that is subjected to oxygen plasma for 5 minutes. Then, Cytop (grade CTL-809M, 5% by mass) is spin-coated at 500 rpm for 10 seconds followed by 1000 rpm for 20 seconds producing a layer 0.4 µm thick. This grade of Cytop is used because it has good adhesion to Si and metals. Next, Cytop is spin-coated (grade CTX-809SP2, 9% by mass) twice; each spin at 1000 rpm for 10 seconds followed 1500 rpm for 20 seconds producing a layer 2.6 µm thick. This produced the 5.2 µm optical grade stack of Cytop. Then, Cytop (grade CTX-809SP2, 5% by mass) is spin-coated at 1000 rpm for 20 seconds producing a layer 0.8 µm thick. This step is necessary for smoothing the surface of the Cytop. After every layer of Cytop is spun on, the glass-slide is soft-baked on a hotplate at 50 °C for 30 minutes, once the entire stack of Cytop is soft-baked a final hard-bake is performed. The slide is heated from 50 °C to 200 °C at a ramp rate of 50 °C/hour, and then held at 200 °C for 1.5 hours. Finally, a 100 nm thick film of Au is evaporated directly onto the surface. Fig. 5 (c) shows the surface roughness of the Au film on Cytop. The RMS roughness was 2.6 nm in this case.

Template stripping combined with Cytop

We combined the Au template stripping approach with a Cytop cladding, for the first time, in order to produce a smooth surface with decreased SP propagation loss in a symmetric refractive index structure when in water. The fabrication procedure consists of the e-beam evaporation of 100 nm of Au on a thermally-grown film of SiO_2 on Si, then spin-coating with Cytop onto the Au film. This process is similar to that described in the previous section, with three differences. First, the thick stack of Cytop (grade CTX-809SP2, 9% by mass) is only spun on once, contributing 2.6 µm to the total Cytop stack. Second, the final smoothing layer of Cytop (grade CTX-809SP2, 5% by mass) is spun on three times to produce a 2.4 µm contribution to the total Cytop thickness. This allowed the production of a slightly thinner total stack of Cytop, 5.4 µm, at slower spin speeds to avoid perturbing the weak Au to the SiO_2 adhesion. Finally, the hard-bake process has been modified. The Cytop after being spun-on and soft-baked is hard-baked from 50 °C to 100 °C at a rate of 25 °C/hour and held at 100 °C for 2 hours. This new hard-bake procedure was introduced to avoid delamination or deformation of the Au due to poor Au to SiO_2 adhesion. The Cytop layer was then coated with epoxy and bonded to a glass slide which was subsequently separated following the approach described above, revealing the Au surface (Au adheres very weakly to SiO_2). Fig. 5 (d) shows the surface roughness of the Au surface formed in this manner. The RMS roughness was 0.11 nm in this case. With this approach, it was possible to achieve an ultra-flat template-stripped gold film with a Cytop substrate.

Nanofabrication of the elliptical nanohole arrays

The elliptical nanohole arrays were machined by using a FB-2100 (Hitachi) focused ion beam (FIB) with a gallium ion source in the Au films fabricated as described previously. The ion beam was set to 40 keV for milling and a beam current of 0.01 nA. Fig. 6 (a) shows a scanning electron microscope image of an optimized elliptical nanohole array with a periodicity of 495 nm, a minor axis of 80 nm and a major axis of 175 nm on the template stripped Au film with Cytop. The size of the elliptical nanohole array was 32×32 μm^2. Fig. 3 (b) shows an AFM image of the same elliptical nanohole array.

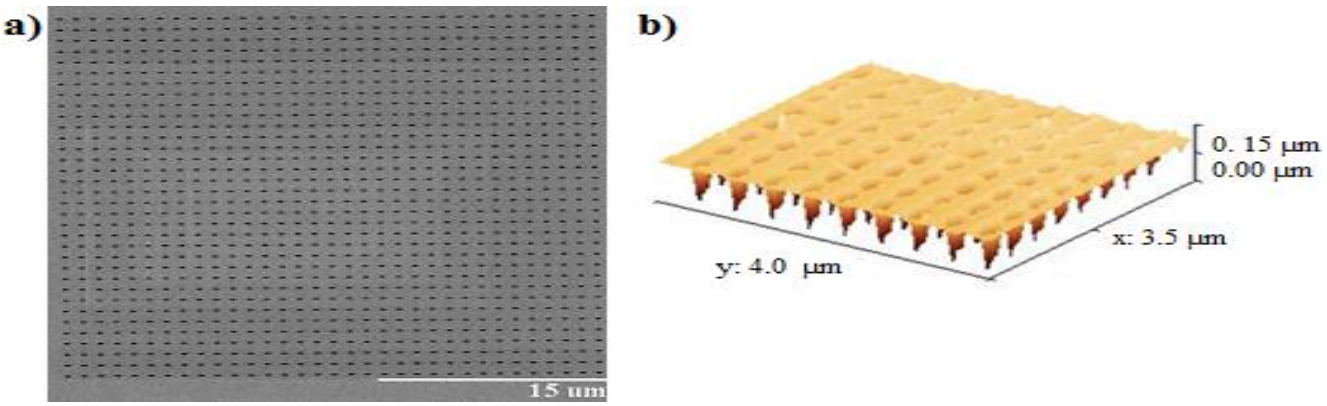

Figure 6. Elliptical nanohole arrays. (a) Scanning electron microscope image of an elliptical nanohole array with a major axis of 175 nm, a minor axis of 80 nm and a periodicity of 495 nm (b) AFM image of the same elliptical nanohole array.

Conclusions

In this work, we demonstrate that it is possible to achieve a bulk sensing resolution using nanohole arrays comparable to the best commercial SPR instruments based on the Kretschmann geometry. This result is achieved by advanced approaches to

the nanohole fabrication, including the use of shaped nanoholes, the use of symmetrized substrates (with respect to refractive index) and the fabrication of ultra-flat surfaces created by template stripping. Such high resolution sensing is promising for multiplexed lab-on-chip biosensors using the simple collinear microscope geometry afforded by the nanohole arrays.

Acknowledgements

This work is supported by the NSERC Strategic Network for Bioplasmonic Systems (Biopsys).

References

1 S.R. Nugen, A.J. Baeumner, *Anal. Bioanal. Chem*. 2008, **391**, 451-454.
2 B. Cherif, A. Roget, C.L. Villiers, R. Calemczuk, V. Leroy, P.N. Marche, T. Livache, M.B. Villiers, *Clin. Chem.* 2006, **52**, 255-262.
3 J.A. Lofgren, S. Dhandapani, J.J. Pennucci, C.M. Abbott, D.T. Mytych, A. Kaliyaperumal, S.J. Swanson, M.C. Mullenix, *J. Immunol.* 2007, **178**, 7467-72.
4 M.A. Cooper, *Nat. Rev. Drug. Discov.* 2002, **1**, 515-28.
5 R.L. Rich, D.G. Myszka, *J. Mol. Recognit.* 2008, **21**, 355-400.
6 Biacore. http://www.biacore.com
7 T.W. Ebbesen, H.J. Lezec, H.F. Ghaemi, T. Thio, P.A. Wolff, *Nature* 1998, **391**, 667-669.
8 A. Krishnan, T. Thio, T.J. Kim, H.J. Lezec, T.W. Ebbesen, P.A. Wolff, J. Pendry, L. Martin-Moreno, F.J. Garcia Vidal, *Opt. Commun.* 2001, **200**, 1-7.
9 A. Degiron, H.J. Lezec, W.L. Barnes, T.W. Ebbesen, *Appl. Phys. Lett.* 2002, **81**, 4327.
10 R. Gordon, A.G. Brolo, A. McKinnon, A. Rajora, B. Leathem, K.L. Kavanagh, *Phys. Rev. Lett.* 2004, **92**, 037401.
11 K.J. Klein Koerkamp, S. Enoch, F.B. Segerink, N.F. van Hulst, L. Kuipers, *Phys. Rev. Lett.* 2004, **92**, 183901.
12 K.L. van der Molen, K.J. Koerkamp, S. Enoch, F.B. Segerink, N.F. van Hulst, L. Kuipers, *Phys. Rev. B* 2005, **72**, 045421.
13 F.J. Garcia-Vidal, L. Martin-Moreno, T.W. Ebbesen, L. Kuipers, *Rev. Mod. Phys.* 2010, **82**, 729-787.
14 P.R.H. Stark, A.E. Halleck, D.N. Larson, *Methods* 2005, **37**, 37-47.
15 H. Gao, J. Henzie, T.W. Odom, *Nano Lett.* 2006, **6**, 2104-2108.

16 A. Lesuffleur, H. Im, N.C. Lindquist, S.H. Oh, *Appl. Phys. Lett*. 2007, **90**, 243110.
17 A. De Leebeeck, L. K. Kumar, V. de Lange, D. Sinton, R. Gordon, A.G. Brolo, *Anal. Chem.* 2007, **79**, 4094-4100.
18 L. Pang, G. Hwang, B. Slutsky, Y. Fainman, *Appl. Phys. Lett.* 2007, **91**, 123112.
19 C.J. Alleyne, A.G. Kirk, R.C. McPhedran, N-A. P. Nicorovici, D. Maystre, *Opt. Express* 2007, **15**, 8163-8169.
20 A. Lesuffleur, H. Im, N.C. Lindquist, K.S. Lim, S.H. Oh, *Opt. Express* 2008, **16**, 219-224.
21 R. Gordon, D. Sinton, K.L. Kavanagh, A.G. Brolo, *Accounts of Chem. Res.* 2008, **41**, 1049-1057.
22 J.C. Sharpe, J.S. Mitchell, L. Lin, N. Sedoglavich, R.J. Blaikie, *Anal. Chem.* 2008, **80**, 2244-2249.
23 J. Homola, *Chem. Rev.* 2008, **108**, 462-493.
24 A. Dhawan, M.D. Gerhold, J.F. Muth, *IEEE Sens. J.* 2008, **8**, 942-950.
25 A.B. Dahlin, M.P. Jonsson, F. Höök, *Adv. Mater.* 2008, **20**, 1436-1442.
26 F. Eftekhari, C. Escobedo, J. Ferreira, X. Duan, E.M. Girotto, A.G. Brolo, R. Gordon, D. Sinton, *Anal. Chem.* 2009, **81**, 4308-4311.
27 N.C. Lindquist, A. Lesuffleur, H. Im, S.H. Oh, *Lab Chip* 2009, **9**, 382-387.
28 K.L. Lee, S.H. Wu, P.K. Wei, *Opt. Express* 2009, **17**, 23104.
29 R. Gordon, A.G. Brolo, D. Sinton, K.L. Kavanagh, *Laser and Photonics Rev.* 2010, **4**, 311-335.
30 C. Escobedo, A.G. Brolo, R. Gordon, D. Sinton, *Anal. Chem.* 2010, **82**, 10015-10020.
31 J. Yao, A.-P. Le, S.K. Gray, J.S. Moore, J.A. Rogers, R.G. Nuzzo, *Adv. Mater.* 2010, **22**, 1102–1110.
32 C. Escobedo, A.G. Brolo, R. Gordon, D. Sinton, *Nano Lett.* 2012, **12**, 1592-1596.
33 K.L. Lee, M.J. Chih, X. Shi, K. Ueno, H. Misawa, P.K. Wei, *Adv. Mater.* 2012, **24**, OP253-OP259.
34 K.A. Tetz, L. Pang, Y. Fainman, *Opt. Lett*. 2006, **31**, 1528-1530.
35 A.P. Blanchard-Dionne, L. Guyot, S. Patskovsky, R. Gordon, M. Meunier, *Opt. Express* 2011, **19**,15041-15046.
36 C. Escobedo, S. Vincent, A.I. K. Choudhury, J. Campbell, A.G. Brolo, D. Sinton, R. Gordon, *J. Micromech. Michroeng.* 2011, **21**, 115001.
37 M. Svedendahl, S. Chen, A. Dmitriev, M. Käll, *Nano Lett.* 2009, **9**, 4428-4433.
38 P.B. Johnson, R.W. Christy, *Phys. Rev. B* 1972, **6**, 4370.
39 Asahi Glass Company, "Technical Information Cytop", distributed by Bellex International Corporation. www.bellexinternational.com
40 J. Heer, J. Coe, *Plasmonics* 2012, **7**, 71-75.
41 H. Im, J.N. Sutherland, J.A. Maynard, S.H. Oh, *Anal. Chem.* 2012, **84**, 1941-1947.
42 P. Berini, *Adv. Opt. Photon.* 2009, **1**, 484-588.
43 K.L. Lee, P.W. Chen, S.H. Wu, J.B. Huang, S.Y.Yang, P.K.Wei, *Nano Lett*. 2012, **6**, 2931-2939.
44 D. Stamou, D. Gourdon, M. Liley, N.A. Burnham, A. Kulik, H. Vogel, C. Duschl, *Langmuir* 1997, **13**, 2425.
45 P. Nagpal, N.C. Lindquist, S.H. Oh, D.J. Norris, *Science* 2009, **325**, 594-597.
46 N.C. Lindquist, T.W. Johnson, D.J. Norris, S.H. Oh, *Nano Lett.* 2011, **11**, 3526-3530.

47 H. Im, S.H. Lee, N.J. Wittenberg, T.W. Johnson, N.C. Lindquist, P. Nagpal, D.J. Norris, S.H. Oh, *ACS Nano* 2011, **5**, 6244-6253.
48 C. Chiu, E. Lisicka-Skrzek, R. N. Tait, P. Berini, *J. Vac. Sci. Technol.* 2010, **B 28**, 729-735.

Chapter 5

5. Conclusions

5.1 Summary and Conclusions

Three separate plasmonic devices were completely fabricated; a plasmon-polariton Bragg grating (PPBG) biosensor, a reflection intensity modulator incorporating a diffraction grating, and elliptical nanohole arrays machined into an ultra-smooth Au surface. The fabrication of all three devices was executed using fabrication techniques detailed in the introduction.

The PPBG biosensor was fabricated with 8 micron wide, 35 nm thick Au waveguides that were stepped in width to produce reflection Bragg gratings. The waveguides are embedded in symmetric, Cytop, bottom and top claddings. Into the top cladding, fluidic channels are etched down to the waveguides enabling the incorporation of fluidics, allowing for the functionalization of the waveguides, i.e. critically enabling the device to function as a biosensor. Complete fabrication details were included, along with fabrication improvements that reduce the incidence of cracks in the Cytop claddings and increase hardness in the top cladding. Optical measurements verifying the function of the device were performed and included.

The modulator produces an oscillation in the intensity of a reflected light beam following the oscillation of a drive voltage. It is based on a MOS capacitor with thin (~ 3 nm) silicon oxide, p-doped silicon wafer and 20 nm thick Au surface. Due to the carrier-refraction effect, surface plasmons that propagate at the oxide-metal surface can experience a change in coupling efficiency by changing the density of charge carriers at the oxide-semiconductor interface. This is accomplished by

applying a negative bias to the metal relative to the body of the semiconductor and driving the capacitor into and out of accumulation with a superimposed AC voltage. The Au SPP surface is 20 nm thick and supports 80 nm thick diffraction gratings that excite the SPPs. Electrical contact pads 250 nm thick are separated from the MOS capacitor by a thick (700 nm) dielectric and electrically connected to the device by 2.5 μm diameter metallized vias. Competed fabrication details were provided in chapter 3 along with preliminary modulation measurements which verified the device concept.

Elliptical nanohole arrays were opened in atomically smooth Au films by FIB machining. Root mean square roughness in the Au film, as low as 0.05 nm, was achieved by template stripping (atomic roughness levels). A high degree of metal film smoothness, along with refractive index symmetrisation of Cytop to fluidics and FDTD optimization of nanohole dimensions enabled a high degree of sensitivity to be achieved. 0.98×10^{-7} refractive index sensing units (RIU). This degree of sensitivity is on the same order of magnitude as commercially available Kretschmann based SPR biosensors and a record for nanohole sensors.

5.2 Future Work

Considerable improvements were made to previous Cytop cladded SPP biosensors with microfluidics. These improvements include better resolution of waveguide dimensions and introducing PPBGs by lithographically stepping in width the waveguide metal. The addition of Bragg gratings has created stringent resolution requirements which were not all met. Gratings with widths of 5 μm and grating

widths of 0.5 μm have yet to be fabricated. Further, biosensing trials involving the PPBG biosensors are pending. To date, the waveguides have been shown to act as Bragg reflectors (See chapter 2, subsection IV). Further trials involving the functionalization of the PPBG waveguides to detect bio-elements such as proteins, viruses or live cells are desired.

It is of interest to fabricate plasmonic modulators with oxides of higher permittivity than that of SiO_2. At present, experiments depositing Hafnium Dioxide are being undertaken. Atomic layer deposition of Hafnia, using tetrakis(dimethylamido)hanfium as a precursor has yielded uniform, insulating films of hafnia 7 nm thick. Further trials producing thinner (~ 3nm), dense hafnia films are of being pursued. Initial modulation results with hafnia modulators have been submitted for publication (Appendix A).

Modulation measurements taken on existing, fabricated modulators are handicapped by Fabry-Perot resonance in the Silicon wafer. More highly doped wafers would dampen the extent of resonance between the backside-ohmic contact and the front-side metal allowing for a reduction of noise in modulation measurements. Fabrication has been started on wafers that are highly p-doped (resistivity = 0.001 – 0.005 ohm•cm).

Appendix A

Plasmonic metal-oxide-semiconductor reflection modulators

Abstract
We propose a plasmonic surface that produces an electrically-controlled reflectance as a high-speed intensity modulator. The device is conceived as a metal-oxide-semiconductor capacitor on silicon with its metal structured as a thin patch bearing a contiguous nanoscale grating. The metal structure serves multiple functions, as a driving electrode, and as a grating coupler for perpendicularly-incident *p*-polarised light to surface plasmons supported by the patch. Modulation is produced by charging and discharging the capacitor and exploiting the carrier refraction effect in silicon along with the high sensitivity of strongly confined surface plasmons to index perturbations. The area of the modulator is set by the area of the incident beam, leading to a very compact device for a strongly-focussed beam. Packaging can be simplified because butt-coupling and propagation through end-facets are not required, and simpler packages suitable for surface devices can be used. The modulator can operate over a broad electrical bandwidth (GHz) with a modulation depth of 3 to 6%, a loss of 3 to 4 dB, and an optical bandwidth of about 50 nm. About 2000 modulators can be integrated over a 100 mm^2 area producing an aggregate data rate in excess of 1 Tb/s. We demonstrate modulators operating at telecommunications wavelengths, fabricated as Au/HfO_2/p-Si capacitors. Applications such as short-reach data communications, massively-parallel data output for optical interconnects to chips, and functional wafer probing for compliance testing post-manufacturing are envisaged. The modulators break conceptually from waveguide-based devices and belong to the same class of devices as surface photodetectors and vertical cavity surface-emitting lasers.

An optical modulator is a key component in telecommunication systems as a device responsible for impressing electronic data signals (digital or analog) onto an optical carrier at the transmitter. Typically, such devices exploit the linear electro-optic effect in a suitable crystal (*e.g.*, $LiNbO_3$, GaAs), the quantum-confined Stark effect in multiple-quantum-well heterostructures (*e.g.*, InP), or the carrier refraction effect in a semiconductor (*e.g.*, Si).[1] High-speed devices are often implemented as a velocity-matched travelling-wave structure where a microwave waveguide overlaps with an optical one over a long interaction length. In a push to cost-reduce modulators and integrate them with electronics, implementation on Si is sought.[2] Conventionally, modulators are large discrete waveguide-based components, requiring input and output coupling to optical fibres via polished or otherwise processed end-facets and costly packaging.[3] Yet, the ever-increasing demand for bandwidth and the need for compact inexpensive modulators motivate further research on these components. The desire to also integrate monolithically with signal-processing and drive electronics strongly motivates the use of Si, the dominant semiconductor in electronics.

Metallic structures hold the promise of compact modulators because they can guide highly-confined surface plasmon-polaritons (SPPs) with field enhancement,[4] which in turn enhances material effects in the modulating medium. They also provide an opportunity to simultaneously use the metal(s) to drive the modulating medium, a capability that was demonstrated initially in thermo-optic modulators by using the metal stripe supporting long-range SPPs to also heat a polymer cladding through Ohmic loss induced by the injection of current.[5,6] This idea was also exploited for thermo-optic modulation in dielectric-loaded SPP waveguides.[7] Metal stripes buried in $LiNbO_3$ were also used to demonstrate a long-range SPP electro-optic modulator.[8] Metal-clad SPP waveguides have also been proposed as modulator structures,[9] exploiting electro-optic effects in polymer,[10] or carrier refraction effects in conductive oxides such as indium tin oxide[11-14] or gallium-doped zinc oxide.[15] Metal-clad modulators based on metal-oxide-semiconductor (MOS) structures in Si and exploiting the carrier refraction effect therein have also been reported,[16-20] including an all-optical concept.[21] Waveguide-based plasmonic modulators can be far more compact than their dielectric counterparts but they still require end-fire excitation, often implemented by butt-coupling to a larger and lower loss dielectric waveguide, so as standalone components some of the benefits of compactness are lost - such modulators seem best suited to applications involving further optical integration in the plane.

In this paper we describe and demonstrate a plasmonic modulator that breaks conceptually from convention: We propose a surface device having an electrically-controlled reflectance as an optically and electrically broadband reflection modulator. The modulator is implemented as a MOS capacitor and is excited by a broadside-incident *p*-polarised continuous-wave (CW) optical beam which it then reflects with an intensity modulation following the electrical drive signal. Thousands of modulators can be densely integrated into arrays over the surface of the substrate. Packaging is simplified because butt-coupling and propagation through end-facets are not required, and simpler packages suitable for surface devices can be used.[3] As the area of the modulator is set by the area of the incident beam, relaxed alignment tolerances can be provided by adopting a modulator area that is slightly larger than that of the latter. Although the concept can work in principle with several modulator materials, we choose to work with Si exploiting carrier refraction therein, anticipating eventual monolithic integration with electronics. We target telecommunications wavelengths and envisage applications such as short-reach data communications, massively-parallel data output for optical interconnects to chips,[22] and functional wafer probing for

compliance testing post-manufacturing.[23] The modulator proposed belongs conceptually to the same class of devices that includes surface photodetectors and vertical cavity surface-emitting lasers.

Modulator structure:

Fig. 1 gives a cross-sectional sketch of our modulator concept. Generally, the device includes a surface for guiding SPPs, consisting of a thin metal patch of thickness t and complex refractive index $n_3 - jk_3$, on a thin insulating oxide layer of thickness d and refractive index n_2, on a doped semiconductor of refractive index n_1. The structure may be passivated by a cover insulating layer of refractive index n_4. The thin metal patch is defined as a circular feature.

Metal ridges of width W and thickness H are arranged in period Λ forming a grating on the thin metal patch (the grating is invariant out of the page). The dimensions of the grating (W, H, Λ), and the thickness of the metal patch (t) and oxide layer (d), are selected such that a broadside-incident *p*-polarised light beam couples to SPPs propagating in the lateral directions along the thin metal patch with fields localised along its *bottom* surface and that penetrate into the doped semiconductor, as depicted in Fig. 1. The SPPs are very sensitive to changes in refractive index occurring within their field decay length.

The thin metal patch and grating, the oxide layer, and the semiconductor, together form a MOS capacitor. Applying a voltage $V_b+v_d(t)$ to the metal patch, where V_b is a DC bias voltage and $v_d(t)$ is a time-dependent voltage, will cause carriers to accumulate in the semiconductor near the thin oxide layer, as depicted in Fig. 1. Carriers accumulate whether the MOS structure is driven into accumulation or inversion, depending on the polarity of the applied voltages relative to ground. An increase in carrier density decreases the refractive index of the semiconductor via the carrier refraction effect. This in turn reduces the effective index (n_{eff}) of the SPP propagating along the patch, which changes the coupling efficiency of the grating and thus the reflected power. Reflection modulation is therefore achieved by modulating the coupling efficiency of the incident beam to the SPPs via the carrier refraction effect in a MOS capacitor.

Several materials could be used to implement the modulator. We consider Au and Cu for the metal (the former as a common SPP metal and the latter as a Si-compatible metal), SiO_2 and HfO_2 for the thin insulating oxide layer, p- and n-doped Si for the semiconductor, and Air and SiO_2 as the cover. The operating wavelengths of interest are in the telecommunications range, $\lambda_0 \sim$ 1310 and 1550 nm.

Results

Theoretical

The carrier concentration distribution in candidate MOS structures was computed as a function of applied voltage by solving Poisson's equation using a commercial device simulator.[24] Specifically, Cu/SiO_2/n-Si MOS structures with d = 2 and 4 nm and a donor concentration of $N_D = 5\times10^{17}$ to 5×10^{19} cm^{-3} were driven into accumulation by applying voltages in the range of V_b = 1 to 5 V. Electron concentrations of 10^{20} to 10^{21} cm^{-3} were

observed over a distance of ~1 nm from the oxide into the Si. Similar hole concentrations are achievable using accumulation voltages of opposite polarity on p-Si. The Drude equation was then used to model the change in refractive index due to an increase in carrier density,[1] revealing that the index of low-doped Si decreases by about 0.5 for a hole or electron concentration of about 4×10^{20} cm^{-3} at our wavelengths of interest.

Very large carrier concentrations can thus be produced using reasonable accumulation voltages and a modest Si doping level in a MOS structure, resulting in very large refractive index perturbations. However, both occur over a very small thickness of about 1 nm. It is therefore desirable for the SPPs propagating along the thin metal patch to be maximally sensitive to index changes that occur in the Si along its interface with the oxide. This situation is very similar to what is desired in SPP biosensors, where high sensitivity to the formation of thin biological adlayers on the surface of a metal film is needed.[25,26]

The transfer matrix method[27] was used to model the structure without the grating. The free-space operating wavelength was set to λ_0 = 1550 nm, SiO_2 ($\varepsilon_{r,4} = 1.444^2$) was selected as the material for the cover layer, Cu ($\varepsilon_{r,3} = (0.606 - j8.26)^2$) as the thin metal film, HfO_2 ($\varepsilon_{r,2} = 1.88^2$) as the thin insulating oxide layer and silicon ($\varepsilon_{r,1} = 3.4767^2$) as the semiconductor. A 1 nm thick perturbed region, of permittivity $\varepsilon'_{r,1} = (3.4767+\Delta n)^2$ with $\Delta n = -0.5$, was used to model the change caused by carrier accumulation in the Si along the oxide due to an applied voltage (all optical parameters originate from Ref. 28, except for HfO_2 which originates from Ref. 29). The inset to Fig. 2 gives a sketch of the structure modelled.

The thickness t was varied from 10 to 30 nm and d was taken as 2, 4 and 6 nm, in order to investigate the impact of these dimensions on the purely bound SPP. The computations reveal that n_{eff} and the mode power attenuation (MPA) of the SPP increase as t and d decrease, following increased field confinement along the bottom surface of the thin metal film. The differential effective refractive index Δn_{eff} of the SPP was also computed over the same range of dimensions (t, d) with and without the 1 nm thick perturbation revealing that $|\Delta n_{eff}|$ also increases with decreasing t and d due to increasing SPP field overlap with the perturbation. Thus, insofar as sensitivity to charge accumulation is concerned, t and d should be selected as thin as possible in order to maximise $|\Delta n_{eff}|$, in the limit of what can be fabricated reliably. A smaller d also favours lower drive voltages but increases the capacitance.

Fig. 2 gives the computed distribution of $Re\{E_y\}$, the main transverse electric field component of the SPP, over the cross-section of the structure, without and with the 1 nm thick perturbation, for t = 20 nm and d = 2 nm. The SPP field is localised along the bottom surface of the thin metal patch and has a large peak in the lower-index oxide layer. The perturbation applied to the Si evidently has a significant impact on the local field distribution. The computed n_{eff} and MPA in this structure are 4.1909 and 4.1757, and 6.89 dB/μm and 6.78 dB/μm, without and with the perturbed region, respectively. A differential effective index of $|\Delta n_{eff}| \sim 0.015$ is observed, which is about two orders of magnitude larger than in biosensing applications at comparable wavelengths.[26] The MPA is large which implies that a patch diameter of a few microns will suffice to fully absorb the SPPs, mitigating optical interference between closely packed modulators.

The grating period Λ is selected to satisfy the momentum conservation condition:

$$\Lambda = m\lambda_0/(n_{eff,a} - n_4 \sin\theta) \quad (1)$$

where m is the (integer) order of the grating, $n_{eff,a}$ is the average effective refractive index of the SPP propagating along the structure including the grating, n_4 is the refractive index of the

cover medium, and θ is the angle of incidence of the beam, which we set to θ = 0° for broadside excitation along the surface normal. Choosing m = 1 and setting $n_{eff,a} = n_{eff}$ simplifies Eq. (1) to the following approximate form:

$$\Lambda \approx \lambda_0 / n_{eff} \quad (2)$$

which is used to obtain an initial value for Λ. The above also illustrates that changes in n_{eff} compromise the momentum conservation condition leading to lower grating coupling efficiency.

The 2-D FDTD method[30] was used to model the optical performance of a cross-section of several candidate designs to determine good dimensions for the gratings. A *p*-polarised 2-D Gaussian beam, several microns in width, was set to originate a few microns above the device and be perpendicularly incident onto the grating. Field observation planes were defined in order to compute the reflectance, transmittance and deduce the absorptance and grating coupling efficiency into the SPPs. A sufficient number of periods was assumed such that the grating was wider than the incident beam. Material dispersion was taken into account for all materials[28] except HfO_2 (due to a lack of measured data).

Fig. 3 shows the computed reflectance (R), absorptance (A) and coupling coefficient to SPPs (C) for a SiO_2 coated Cu/SiO_2/n-Si MOS modulator having Λ = 410 nm, W = 200 nm, H = 80 nm, t = 20 nm and d = 2 nm. R1 and C1 were computed with the refractive index perturbation in Si (1 nm thick region of Δn = - 0.5 along the interface with the oxide), whereas R0, A0 and C0 were computed without the perturbation. The absorptance and coupling coefficient (A0, C0) are observed to be largest at λ_0 ~ 1530 nm which corresponds to the wavelength where Eq. (1) is satisfied for this design. Most of the absorptance (A0 = 0.58) is due to coupling to SPPs (C0 ~ 0.53). The reflectance (R0) goes through a minimum close to this wavelength. The difference in the coupling coefficients between the perturbed and unperturbed cases (C1, C0) causes the reflectance to change (R1, R0) producing the desired intensity modulation on the reflected beam. The largest reflectance modulation occurs slightly off-resonance, in this case at λ_0 = 1507 nm (indicated by the vertical dashed line), where a modulation of R1 - R0 = -0.03 is observed. The nominal reflectance at this wavelength is about 0.43 implying a modulator loss of about 3.7 dB. The FWHM of the modulation response (R1-R0) is observed to span ~50 nm about this wavelength, and is taken as the optical bandwidth of the modulator.

Investigating several designs over our wavelengths of interest reveals many facts about the modulator concept. The operating wavelength (maximum |R1-R0|) is usually blue-shifted from the wavelength of maximum coupling to SPPs. Grating ridge heights that provide strong coupling are H ~ 80 to 120 nm. The maximum coupling and modulation wavelengths increase with Λ. The optical FWHM modulation bandwidth remains about 50 nm. Good patch thicknesses are t = 15 to 25 nm and good oxide thicknesses are d = 2 to 6 nm. The largest modulation depth observed from our computations was |R1-R0| ~ 0.06 for a Au/HfO_2/Si MOS modulator operating at 1310 nm. As another example, a Cu/SiO_2/Si MOS modulator operating at 1550 nm would produce |R1-R0| ~ 0.02. Generally, the modulation depth decreases with increasing operating wavelength, for Cu relative to Au, and for SiO_2 relative to HfO_2.

Electrically, the MOS modulators can be modelled as a lumped-element RC circuit, as sketched in inset to Fig. 3. The modulator series resistance R_s is due to contact and substrate resistances, and ideally is small. R_p is the shunt resistance of the oxide and ideally is infinite.

C_m is the capacitance of the modulator, which is largest under strong accumulation (worst case) and given by the capacitance of the oxide only:

$$C_m = \varepsilon_0 \varepsilon_{rs,2} A_m / d \quad (3)$$

where A_m is the area of the structure and $\varepsilon_{rs,2}$ is the static relative permittivity of the oxide. The modulator is assumed connected to a load R_L and driven by a generator of internal impedance R_g. The electrical bandwidth of this circuit (assuming $R_p = \infty$) is then:[1]

$$\mathrm{BW} = 1/[2\pi\ (R_s + R_g||R_L)C_m] \quad (4)$$

Normally $R_L = R_g$ (matched impedances) and both are set to a standard value such as 50 Ω. We assume this to be the case, along with $R_s = 0$ ideally (or small compared with $R_g||R_L$), and $\varepsilon_{rs,2} = 3.9$ and 11 as the static relative permittivity of SiO_2 and HfO_2 respectively.[31,32] The electrical bandwidth was then computed over several modulator designs, yielding a broad range of values, such as BW ~ 100 MHz for a 50 μm diameter modulator having HfO_2 as its oxide with d = 4 nm (C_m ~ 60 pF), and BW ~ 100 GHz for a 2.5 μm diameter modulator having SiO_2 as the oxide with d = 4 nm (C_m ~ 0.05 pF). SiO_2 produces higher BW modulators compared to HfO_2 for the same A_m and d, but requires larger drive voltages to achieve the same carrier concentration and modulation depth. A smaller A_m produces a larger BW, the smallest diameter being limited by the ability to focus and align the incident beam, and by the minimum number of grating ridges that can be accommodated on the patch. The lower limit of 2.5 μm corresponds to the focussed diameter that can be achieved with, *e.g.*, a tapered optical fibre while allowing about 6 grating periods to be accommodated.
Bit-error-rate (BER) estimates were also computed using MOS modulators operating with on/off keying in an optical fibre link, assuming commercial ancillary optoelectronic and passive components. We find that error-free communications (BER = 10^{-12}) can be achieved with -9 to -2 dBm of laser power for a modulation depth of |R1-R0| ~ 0.04 to 0.01, over an electrical bandwidth of 1.5 GHz, in a link with negligible fibre impairment. The performance expected is therefore sufficient for a broad range of short-reach applications, including those envisaged.

Experimental

Modulators were fabricated and characterised as described under "Methods" on p- Si wafers, with HfO_2 as the thin oxide, Au for the metal patch and grating ridges, an Al Ohmic contact on the backside, and no cover layer (air) to allow for direct electrical probing. The modulators were shaped as circular to avoid field discontinuities and premature breakdown at corners, and include a contact arm with a probing pad to facilitate direct probing. Various modulator diameters in the range from 3 to 56 μm were fabricated, along with gratings having a 50 to 60% duty cycle and a period near 350 or 450 nm targeting telecommunications wavelengths near 1310 or 1550 nm respectively.
Fig. 4(a) gives a SEM image of a fabricated modulator on a wafer identified internally as 2f1-d (all experimental results originate from this wafer). Fig. 4(b) shows a microscope image of ~ 1700 modulators distributed over a ~100 mm^2 area on a single die. The image was taken at a shallow angle in order to produce visible higher-order diffraction from each modulator. Each colour spot corresponds to one modulator, and the diffracted colour changes with the period of the design. Each modulator consumes, effectively, an area of about 250×250 μm^2 but they could be packed to a higher density, *e.g.*, following a 50 μm pitch.

Fig. 5 plots the *p*-polarised optical reflectance response measured at normal incidence of four uncoated modulators ($n_4 = 1$) of different grating period (Λ). The rapid variation in reflectance with wavelength is due to Fabry-Perot resonances as light transmitted through the modulator propagates through the transparent (low-doped) Si substrate and reflects from the backside Ohmic contact. These resonances could easily be eliminated if desired by using a heavily-doped substrate. The slowly varying reflectance response, highlighted as the moving average plotted in bold, is due to grating coupling of the incident beam to SPPs on the bottom of the thin metal patch. These slow responses are similar to the reflectance curve labelled R0 on Fig. 3, and their minimum is observed to red-shift with the grating period, following the coupling expected from the grating equation (Eq. (1)). Modulation was observed from three of these devices: near 1540 nm for Λ = 430 nm, near 1600 nm for Λ = 450 nm, and near 1620 nm for Λ = 460 nm.

Fig. 6 plots optical modulation traces measured at the photoreceiver with an oscilloscope for two modulators identified internally as D14 and D17. D14 consisted of a 22.5 μm diameter modulator, of total area $A_m = 598\ \mu m^2$ (including the contact arm and contact pad), having a grating of period Λ = 450 nm and 50% duty cycle; and D17 consisted of a 28.2 μm diameter modulator, of total area $A_m = 883\ \mu m^2$ (including the contact arm and contact pad), having a grating of period Λ = 460 nm and 50% duty cycle. The electrical drive applied to the modulators consisted of a negative DC bias voltage ($V_b < 0$) and a sinusoidal RF voltage of amplitude comparable to the DC bias voltage in order to drive the MOS structure in and out of accumulation to effect modulation (recall that holes accumulate for MOS capacitors on p-Si).

Fig. 6(a) compares modulation traces obtained for D14 at 45 MHz, under the same electrical drive conditions, as the optical wavelength was varied. The clearest trace is observed for the case λ_0 = 1590 nm, with modulation being discernable at λ_0 = 1580 and 1560 nm but not at λ_0 = 1600 nm. Thus the operating wavelength is near λ_0 = 1590 nm, which is consistent with the location of the reflectance dip measured on a similar device bearing the same grating design (Fig. 5, Λ = 450 nm), and the optical bandwidth is ~30 nm which is close to theoretical expectations. The trace for D14 plotted in Fig. 6(b) was obtained under the same electrical drive conditions as in Part (a) except at a frequency of 250 MHz. Modulation traces were observed up to 500 MHz, limited by the electrical bandwidth of our oscilloscope.

The trace for D17 plotted in Fig. 6(b) was obtained at 45 MHz with the electrical drive power and bias voltage selected to maximise the peak-to-peak voltage observed on our oscilloscope. In this case, the DC bias was set to V_b = -0.6 V and the incident RF power to 8.7 dBm, which would correspond to a drive voltage of v_d = 0.86 V into a 50 Ω load. The laser power was set to 3 mW and the operating wavelength to λ_0 = 1610 nm, which is consistent with the location of the reflectance dip measured on a similar device bearing the same grating design (Fig. 5, Λ = 460 nm). The measured modulation depth of this device is $|R1-R0| \sim 0.016$, which is lower than desired mostly because the HfO_2 and thin metal patch are slightly thicker than desired. Their thicknesses were measured as d = 7 nm and t = 24 nm (see "Methods), whereas a modulation depth of 0.03 to 0.04 is expected for d = 4 nm and t = 20 nm.

Fig. 7 plots the measured impedance response (symbols) of a modulator, 22.5 μm in diameter of total area $A_m = 598\ \mu m^2$ including contact arm and pad, as a function of DC bias (V_b) into the accumulation region. The impedance response of the modulator was computed from the equivalent circuit sketched in inset to Fig. 3 and is also plotted (solid and dashed

curves). The parameters of the circuit, given in the legend of Fig. 7 (R_s, C_m), were deduced by manually fitting the computed responses to the measurements. No DC leakage current was observed (R_p > 1 MΩ).

The impedance of the MOS structure changes with bias as the device state progresses from depletion to accumulation.[31] Smaller device capacitances C_m are observed and expected at weak or no bias because the oxide capacitance appears in series with the depletion capacitance. As the device is biased into accumulation, the depletion capacitance gradually disappears, leaving only the oxide capacitance. The extracted capacitance C_m trends with increasing bias voltage magnitude $|V_b|$ to the value expected under strong accumulation, which is 8 pF (computed using Eq. (3) with A_m = 598 μm^2, d = 7 nm and $\varepsilon_{rs,2}$ = 11). The fitted values for R_s of 70 to 40 Ω originate partly from the substrate resistance and are reasonable given its modest doping level and thickness.

The electrical bandwidth of this device at V_b = -0.4 V in a 50 Ω system, determined using Eq. (4) with $R_L = R_g$ = 50 Ω, and C_m = 4.3 pF with R_s = 50 Ω (Fig. 7), is about 500 MHz. The bandwidth could be significantly increased by using a smaller area modulator and fabricating the contact arm and probing pad on a higher level (*e.g.*, above a thick inter-metal dielectric) to eliminate their parasitic capacitance which accounts for about 1/3 of the total capacitance in this device. Using a substrate of higher doping (about 20×), or fabricating top surface ground contacts in doped wells, would substantially reduce R_s. With such changes, electrical bandwidths in the 10's of GHz, as projected theoretically, could be achieved. In an integration scenario with electronics, a driver amplifier would be co-designed with the modulator further reducing parasitics and eliminating the matching constraint to specifically 50 Ω. Nonetheless, a 500 MHz electrical bandwidth is sufficient for 1 Gb/s on-off keying, implying that an aggregate bit rate of about 1.7 Tb/s could be achieved by operating all 1700 modulators shown in Fig. 4(b).

Methods

Fabrication

Modulators were fabricated on prime grade double-side-polished, p-doped (boron) Si wafers, 280 μm thick and 50.8 mm (2 in) in diameter, in the 100 orientation, of resistivity ρ = 0.08 to 0.095 Ω·cm ($N_A = 3.1\times10^{17}$ to 2.5×10^{17} cm^{-3}). Wafers were RCA-cleaned then sacrificial SiO_2 was grown thermally and stripped using HF. An Ohmic contact was formed on the wafer backside by evaporating and sintering a 1 μm thick Al film. Formation of the HfO_2 film was carried out by atomic layer deposition (ALD),[32,33] after treating the wafer surface in buffered HF then in H_2O_2 heated to 75 °C for 4 min. ALD was carried out in 50 cycles at 275 °C using tetrakis(dimethylamido)hafnium and H_2O as gas precursors, aiming for a film thickness of about d ~ 5 nm. The metal patches defining the area of the modulators were then fabricated via optical lithography and lift-off of thermally-evaporated Au (t ~ 20 to 25 nm) on < 1 nm of Cr used as an adhesion layer to HfO_2. The modulator designs consisted of variable diameter circular areas with a contact arm and pad to facilitate electrical probing. The gratings were fabricated by e-beam lithography overlaid on the metal patches and lift-off of thermally-evaporated Au (H ~ 80 nm). The designs consisted of variable period (Λ) and

duty cycle (50 to 60%) gratings. There was no cover layer in order to facilitate direct electrical probing. Fabrication details for these process steps have been reported elsewhere,[34] except for the formation of HfO_2 via ALD.[32,33]
The thickness of the HfO_2 film was measured using ellipsometry immediately after formation, yielding a mean value of d = 7.2 nm and a standard deviation of 0.088 nm, based on measurements taken at 5 locations on the wafer. Capacitance versus voltage measurements were then obtained in the accumulation region, on several structures immediately after formation of the metal patches. From the C-V curves, a breakdown field of 6.4 MV/cm and a static relative permittivity of $\varepsilon_{rs,2} = 11$ were deduced for the HfO_2 film. Both of these values are consistent with ALD-deposited HfO_2[32,33] but the static permittivity is lower than the bulk value, possibly due to the lower density of the film or the formation of a thin SiO_x layer on the Si surface prior to ALD deposition. The measured conductance of the HfO_2 film remained very low (1 to 5 μS for a 56 μm diameter pad). The thickness of the HfO_2 film was also verified independently via an AFM measurement over a square area where HfO_2 was etched to produce steps. AFM measurements on the metal patches revealed a thickness of t = 24 nm. The HfO_2 and metal film roughness are about 3 nm. The gratings were characterised via SEM after lift-off, revealing ridges that are about H = 90 nm thick with a period and duty cycle that are very close to the target values.

Measurements

The modulator measurements were obtained using an electro-optic test set-up assembled specifically for this purpose. The optical path comprised a tunable laser (Photonetics Tunics Plus) connected to a polarisation-maintaining single-mode fibre terminated with collimating optics to launch the incident beam. The incident beam was focussed through a beam splitter cube onto the modulator under test. The beam reflected from the modulator was reflected by the beam splitter and send through focussing optics onto a high-speed avalanche photoreceiver (Menlo Systems APD 310). The photoreceiver was connected to an oscilloscope used to measure the detected waveform (Tektronics TDS540A). A continuous-wave power sensor (Thorlabs S132C) was inserted on occasion into the reflected beam path to measure the passive reflectance of modulator as the laser was tuned. An infrared camera (Electrophysics Micron Viewer 7290A) was also switched on occasion into the reflected beam path in lieu of the photoreceiver to assist with beam-to-modulator alignment by viewing the modulator through the output focussing optics. The optical path was calibrated using a reference mirror fabricated on the same chip as the modulator, and the modulation depth was determined by directly modulating the laser source and comparing the voltages read on the oscilloscope.
The electrical path originated with an HP 8510B vector network analyser (VNA) with one port connected to a variable gain amplifier (Mini-Circuits TVA-11-422) followed by a bias-T (Mini-Circuits ZX85-12G-S+) connected to a probing system (Picoprobe Model 10) terminated with custom open-circuited signal-ground electrical probe tips to contact the modulator under test (a terminating load resistor was not used, $R_L = \infty$). The modulator was mounted onto a custom-machined microwave test jig and aligned in the set-up using a 6-axis piezo translation stage (Thorlabs Nanomax Max603). The DC bias voltage was applied through the bias-T using a source meter which was also used to simultaneously measure the

DC bias current (Keithley 2400). The DC bias current remained near the noise floor of the source meter for all of the modulation measurements reported. The An HP 436A power meter with an HP 8481A sensor head were used to determine the microwave power used to drive the modulator. The VNA without the amplifier was also used to measure S11 of the modulator from which its impedance was determined. On-jig custom calibration standards (open, short, load) were used to calibrate the VNA for this purpose, from its test port up to the end of the electrical probe tips.

Acknowledgements
Financial support from the Natural Sciences and Engineering Research Council of Canada and from Test Photonics Canada is gratefully acknowledged. The authors are also grateful to Vincent Tabard-Cossa and Benjamin Watts for assistance with the atomic layer deposition of HfO_2.

Author contributions
P.B. generated the modulator concept. C.C. carried out modelling and design work. S.H. fabricated the devices with the assistance of A.O and E.L.-S. A.O. built the experimental characterisation set-up and obtained the measurements. R.N.T. and P.B. directed the work.

References:

1. Chen, A. & Murphy, E. J., *Broadband optical modulators: Science Technology and Applications*. CRC Press, Boca Raton USA, (2012).

2. Reed, G. T., Mashanovich, G., Gardes, F. Y. & Thomson, D. J. Silicon optical modulators. *Nature Photonics* **4**, 518-526 (2010).

3. Tekin, T., Review of Packaging of Optoelectronic, Photonic, and MEMS Components. *IEEE J. Sel. Top. Quant. Electr.* **17**, 704-719 (2011).

4. Schuller, J. A., Barnard, E. S., Cai, W., Jun, Y. C., White, J. S. & Brongersma, M. L. Plasmonics for extreme light concentration and manipulation. *Nature Materials* **9**, 193-204 (2010).

5. Nikolajsen, T., Leosson, K., & Bozhevolnyi, S. I. Surface plasmon polariton based modulators and switches operating at telecom wavelengths. *Appl. Phys. Lett.* **85**, 5833-5835 (2004).

6. Gagnon, G., Lahoud, N., Mattiussi, G. & Berini, P. Thermally activated variable attenuation of long-range surface plasmon-polariton waves. *J. Lightwave Technol*. **24**, 4391-4402 (2006).

7. Gosciniak, J., Bozhevolnyi, S. I., Andersen, T. B., Volkov, V. S., Kjelstrup-Hansen, J., Markey, L., & Dereux, A. Thermo-optic control of dielectric-loaded plasmonic waveguide components. *Opt. Express* **18**, 1207-1216 (2010).

8. Berini, P., Charbonneau, R., Jetté-Charbonneau, S., Lahoud, N. & Mattiussi, G. Long-range surface plasmon-polariton waveguides and devices in lithium niobate. *J. Appl. Phys.* **101**, 113114 (2007).

9. Cai, W., White, J. S., & Brongersma, M. L. Compact high-speed and power-efficient electrooptic plasmonic modulators. *Nano Lett.* **9**, 4403-4441 (2009).

10. Melikyan, A., Alloatti, L., Muslija, A., Hillerkuss, D., Schindler, P. C., Li, J., Palmer, R., Korn, D., Muehlbrandt, S., Van Thourhout, D., Chen, B., Dinu, R., Sommer, M., Koos, C., Kohl, M., Freude, W. & Leuthold, J. High-speed plasmonic phase modulators. *Nature Photonics* **8**, 229-233 (2014).

11. Melikyan, A., Lindenmann, N., Walheim, S., Leufke, P. M., Ulrich, S., Ye, J., Vincze, P., Hahn, H., Schimmel, Th., Koos, C., Freude, W. & Leuthold, J. Surface plasmon polariton absorption modulator. *Opt. Express* **19**, 8855-8869 (2011).

12. Krasavin, A. V. & Zayats, A. V. Photonic signal processing on electronic scales: Electro-optical field-effect nanoplasmonic modulator. *Phys. Rev. Lett.* **109**, 053901 (2012).

13. Sorger, V. J., Lanzillotti-Kimura, N. D., Ma, R.-M., Zhang, X. Ultra-compact silicon nanophotonic modulator with broadband response. *Nanophotonics* **1**, 17-22 (2012).

14. Zhu, S., Lo, G. Q. & Kwong, D. L. Design of an ultra-compact electro-absorption modulator comprised of a deposited TiN/HfO_2/ITO/Cu stack for CMOS backend integration. *Optics Express* **22**, 17930-17947 (2014).

15. Babicheva, V., Kinsey, N., Naik, G. V., Ferrera, M., Lavrinenko, A. V., Shalaev, V. M. & Boltasseva, A. Towards CMOS-compatible nanophotonics: ultra-compact modulators using alternative plasmonic materials. *Opt. Express* **21**, 27326-27337 (2013).

16. Dionne, J. A., Diest, K., Sweatlock, L. A. & Atwater, H. A. PlasMOStor: a metal-oxide-Si field effect plasmonic modulator. *Nano Lett*. **9**, 897-902 (2009).

17. Zhu, S., Lo, G. Q. & Kwong, D. L. Theoretical investigation of silicon MOS-type plasmonic slot waveguide based MZI modulators. *Opt. Express* **18**, 27802-27819 (2010).

18. Zhu, S., Lo, G. Q. & Kwong, D. L. Electro-absorption modulation in horizontal metal-insulator-silicon-insulator-metal nanoplasmonic slot waveguide. *Appl. Phys. Lett.* **99**, 151114 (2011).

19. Zhu, S., Lo, G. Q. & Kwong, D. L. Phase modulation in horizontal metal-insulator-silicon-insulator-metal plasmonic waveguides. *Opt. Express* **21**, 8320-8330 (2013).

20. Thomas, R., Ikonić, Z. & Kelsall, R. W. Plasmonic modulators for near-infrared photonics on a silicon-on-insulator platform. *IEEE. J. Sel. Top. Quant. Electr.* **19**, 4601708 (2013).

21. Nielsen, M. P. & Elezzabi, A. Y. Ultrafast all-optical modulation in a silicon nanoplasmonic resonator. *Opt. Express* **21**, 20274-20279 (2013).

22. Miller, D. A. B. Device requirements for optical interconnects to silicon chips. *Proc. IEEE* **97**, 1166-1185 (2009).

23. Marinissen, E. J., Lee, D. Y., Hayes, J. P., Sellathamby, C., Moore, B., Slupsky, S. & Pujol, L. Contactless Testing: Possibility or Pipe-Dream? Proceedings of the Conference on Design, Automation and Test in Europe - DATE ‘09, 676-681 (2009).

24. ATLAS (S-PISCES), Silvaco International.

25. Cullen, D. C., Brown, R. G. W. & Lowe, C. R. Detection of immuno-complex formation via surface plasmon resonance on gold-coated diffraction gratings. *Biosens*. **3**, 211–225 (1987).

26. Berini, P. Bulk and surface sensitivities of surface plasmon waveguides. *New J. Phys.* **10**, 105010 (2008).

27. Chen, C., Berini, P., Feng, D., Tolstikhin, V.I., Tanev, S. & Tzolov, V.P. Efficient and Accurate Numerical Analysis of Multilayer Planar Lossy and Active Optical Waveguides in Anisotropic Media. *Opt. Express* **7**, 260-272 (2000).

28. Palik, E. D. *Handbook of Optical Constants of Solids*. Elsevier, (1998).

29. Jerman, M., Qiao, Z., & Mergel, D. Refractive index of thin films of SiO_2, ZrO_2, and HfO_2 as a function of the films' mass density. *Appl. Opt.* **44**, 3006-3012 (2005).

30. Lumerical Solutions Inc.

31. Sze S. M. *Physics of Semiconductor Devices*. 2nd Ed., Wiley, New York, 1981

32. Scarel, G., Spiga, S., Wiemer, C., Tallarida, G., Ferrari, S. & Fanciulli, M., Trends of structural and electrical properties in atomic layer deposited HfO_2 films. *Mat. Sci. Eng. B* **109**, 11–16 (2004).

33. Molina, J., Zuniga, C., Calleja, W., Rosales, P., Torres, A. & Herrera-Gomez, A. Physical and electrical characteristics of atomic-layer deposition-HfO_2 films deposited on Si substrates having different silanol Si-OH densities. *J. Vac. Sci. Technol. A* **31**, 01A132 (2013).

34. Hassan, S., Lisicka-Skrzek, E., Olivieri, A., Tait, R. N. & Berini, P. Fabrication of a Plasmonic Modulator Incorporating an Overlaid Grating Coupler. *Nanotechnology*, in press

List of Figures

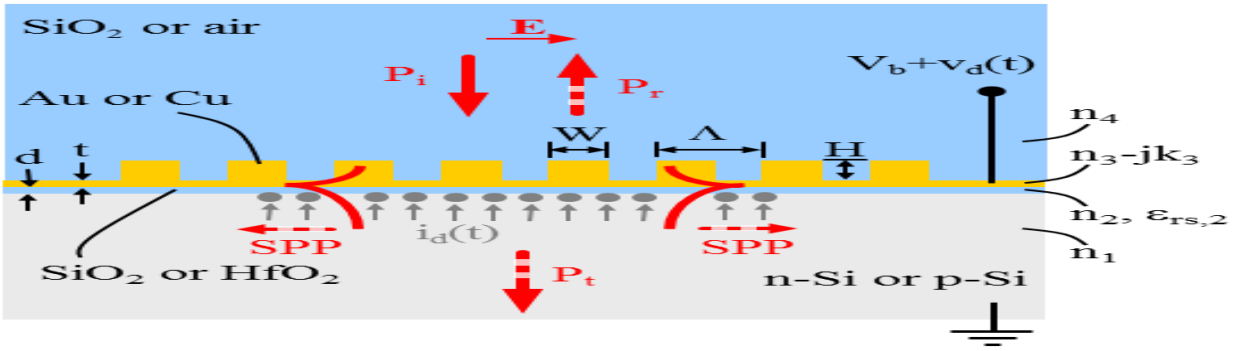

Fig. 1. Cross-sectional sketch of a MOS modulator comprising a metal surface of thickness t, with a metal grating consisting of rectangular ridges of width W and thickness H arranged periodically in pitch Λ, on an oxide layer of thickness d, on a semiconductor. The materials considered are Cu and Au for the metal, SiO_2 and HfO_2 for the oxide, and n-type or p-type Si for the semiconductor. The top of the device may be coated with a dielectric such as SiO_2 or left open.

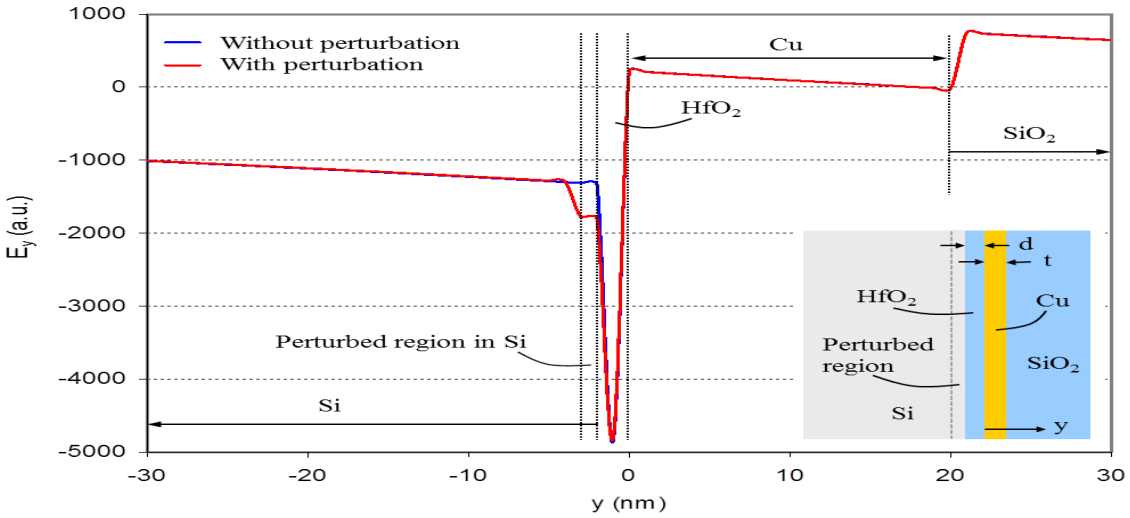

Fig. 2. Computed distribution of Re{E_y} over the cross-section of a SiO_2 coated Cu/HfO_2/Si MOS structure, with and without a 1 nm thick refractive index perturbation of $\Delta n = -0.5$ applied to the Si along the interface with the oxide. The structure modelled is sketched in inset and the case t = 20 nm and d = 2 nm is plotted at λ_0 = 1550 nm.

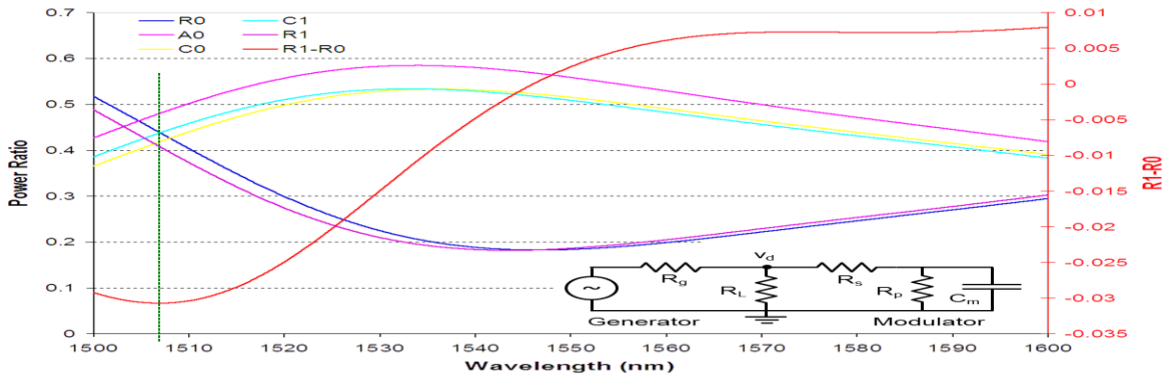

Fig. 3. Computed reflectance (R), absorptance (A) and coupling coefficient to SPPs (C) for a SiO_2 coated Cu/SiO_2/n-Si MOS modulator (Λ = 410 nm, W = 200 nm, H = 80 nm, t = 20 nm, d = 2 nm). R0, A0, C0: unperturbed; R1, C1: perturbed by a 1 nm thick refractive index change of Δn = - 0.5 applied to the n-Si along the interface with the oxide. The operating wavelength of this design is λ_0 = 1507 nm (indicated by the vertical dashed line) which produces a reflectance modulation of R1 - R0 = -0.03. The equivalent electrical circuit of the modulator (R_s, R_p, C_m), connected to a generator of internal resistance R_g and a load of resistance R_L, is sketched in inset.

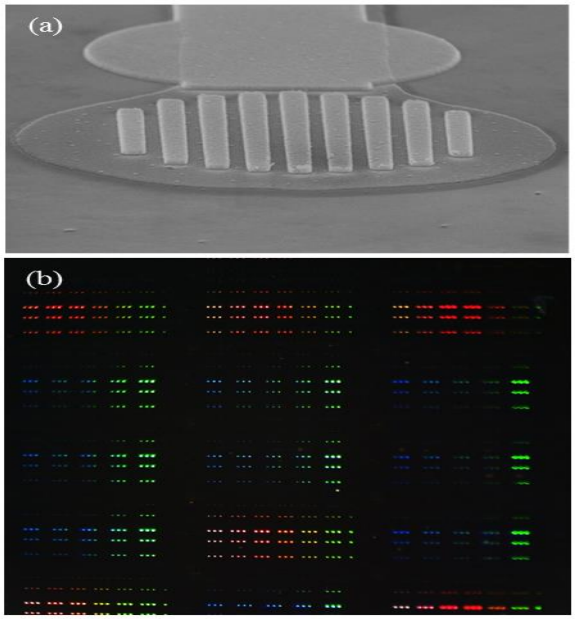

Fig. 4. (a) SEM image of an uncoated Au/HfO_2/p-Si MOS modulator on wafer 2f1-d (the width of a grating ridge is 290 nm). (b) Optical microscope image of modulators (as in Part (a)), of varying grating period. Each colour spot corresponds to one modulator. The area shown is about 100 mm^2 and contains ~1700 modulators.

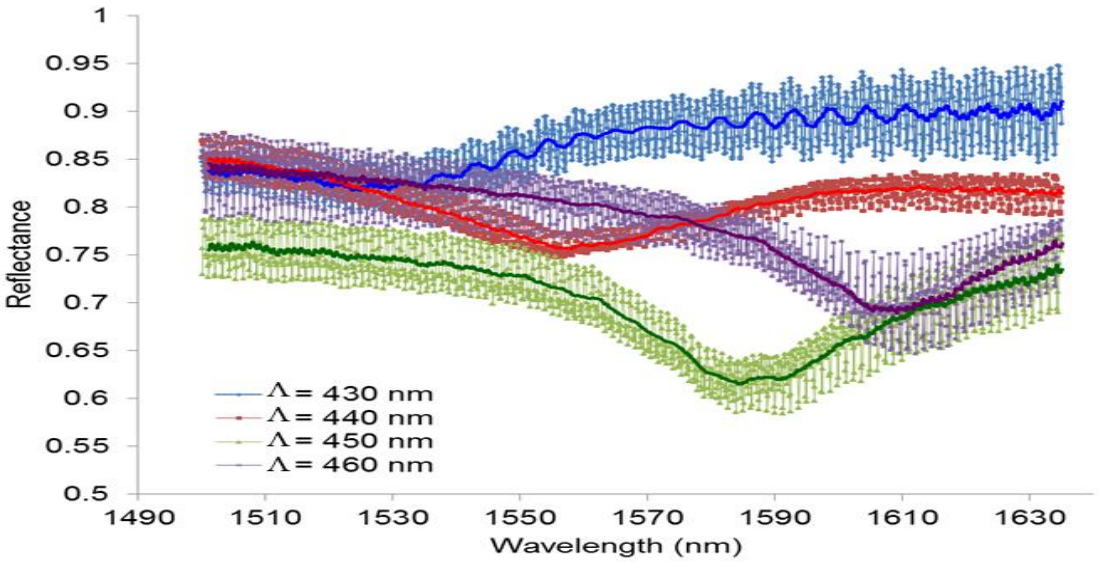

Fig. 5. Measured optical reflectance response of four uncoated Au/HfO_2/p-Si MOS modulators of different grating period (Λ). A 12 period moving average is plotted on each response as the bold curve.

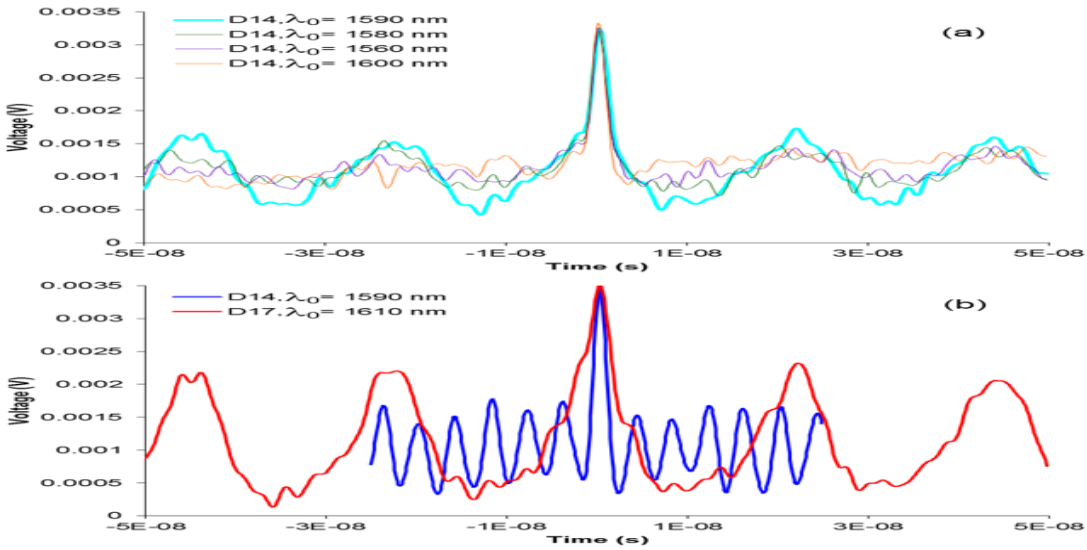

Fig. 6. Optical modulation traces measured at the photoreceiver with an oscilloscope for uncoated Au/HfO_2/p-Si MOS modulators. (The peak at the time origin is an artefact originating from the trigger of our oscilloscope.) (a) All traces were obtained on device 14 (D14) at 45 MHz under the same electrical drive conditions. (b) The trace for D14 was obtained under the same drive conditions as in Part (a) except at a frequency of 250 MHz. The trace for device 17 (D17) was obtained at 45 MHz with the drive power and bias voltage selected to maximise the measured voltage.

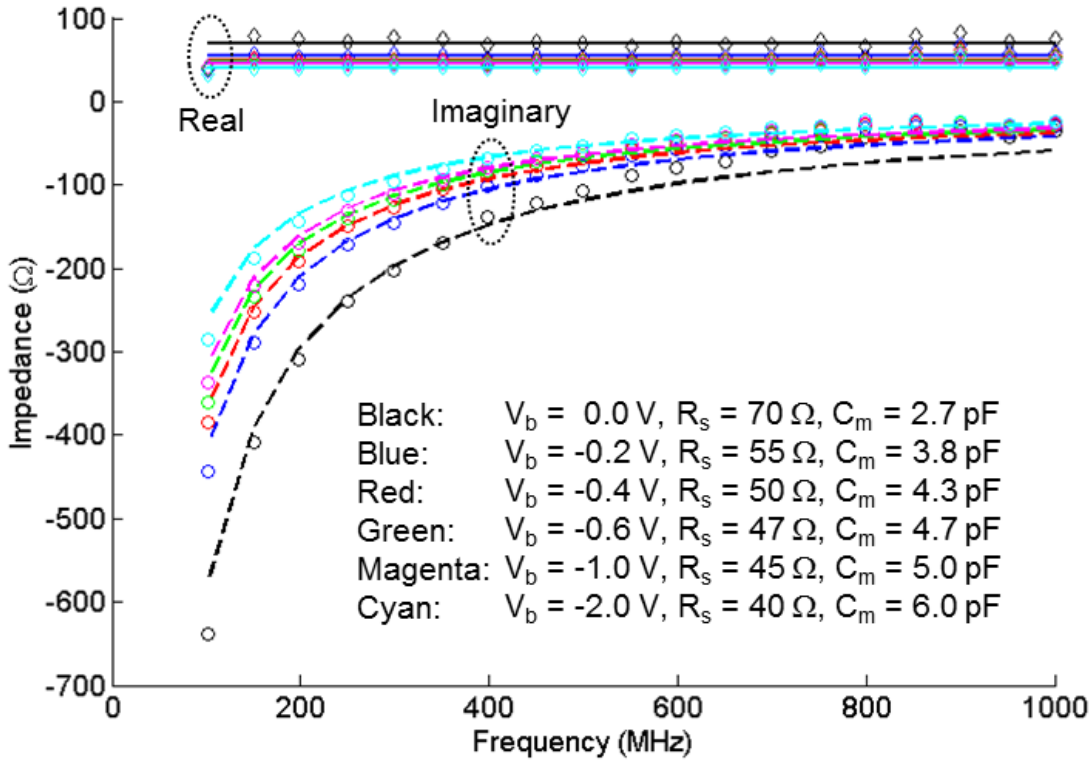

Fig. 7. Impedance response of an uncoated Au/HfO_2/p-Si MOS modulator 22.5 μm in diameter of total area 598 μm^2 (including contact arm and pad), as a function of DC bias (V_b) into the accumulation region. The measurements are denoted as symbols and the computed response of the equivalent electrical circuit (sketched as inset to Fig. 3) as the solid and dashed curves. The parameters of the equivalent circuit were obtained by manual fitting to the measurements and are given in the legend (R_s, C_m with R_p > 1 MΩ).